COMPUTATIONAL STUDIES OF METAL FREE C−H BOND FUNCTIONALIZATION

by

Cristian A. Morales Rivera

Bachelor of Science, University of Puerto Rico Rio Piedras Campus, 2014

Submitted to the Graduate Faculty of

the Dietrich School of Arts and Sciences in partial fulfillment

of the requirements for the degree of

Doctor of Philosophy

University of Pittsburgh

2019

UNIVERSITY OF PITTSBURGH

DIETRICH SCHOOL OF ARTS AND SCIENCES

This dissertation was presented

by

Cristian A. Morales Rivera

It was defended on

August 28, 2019

and approved by

Paul Floreancig, Professor, Dietrich School of Arts and Sciences, University of Pittsburgh

Daniel S. Lambrecht, Assistant Professor, Dietrich School of Arts and Sciences, University of Pittsburgh

Giannis Mpourmpakis, Assistant Professor, Swanson School of Engineering, University of Pittsburgh

Committee Chair: Peng Liu, Assistant Professor, Dietrich School of Arts and Sciences, University of Pittsburgh

Copyright © by Cristian A. Morales Rivera

2019

COMPUTATIONAL STUDIES OF METAL FREE C−H BOND FUNCTIONALIZATION

Cristian A. Morales Rivera, PhD

University of Pittsburgh, 2019

Carbon–hydrogen bond functionalization reactions can greatly facilitate chemical synthesis due to their capability to increase molecular complexity from readily available starting materials with minimal waste generation. These processes are most often achieved through transition metal catalysis, though metal-free approaches for such reactions are becoming increasingly common. DDQ and hypervalent iodine reagents have shown to be greatly useful for promoting C–H cleavage. DFT calculations presented in this dissertation were performed to study the mechanistic pathways of metal free C–H functionalization mediated by DDQ and various hypervalent iodine reagents. These computational investigations not only replicate and explain the experimental observations, but also provide a better understanding of the reaction mechanisms and factors contributing to the reactivity and selectivity. These computational insights were used to develop a predictive reactivity model for the DDQ-mediated C–H functionalization.

TABLE OF CONTENTS

LIST OF TABLES

LIST OF FIGURES

DEDICATION

This dissertation is dedicated to my wife Daniela Esis-Villalobos for her love and encouragement. To my mom Jackeline Rivera-Hernandez for all her dedication, support and for teaching me value of education. To my stepfather Cruz Rodriguez De Jesus for his support and guidance. To my dad Juan Morales-Santiago for his support. To my lovely grandparents Hector Rivera-Rivera and Ramona Hernandez-Carrasquillo for their love and support. To the best brothers someone can have Juan Morales-Rivera and Hector Morales-Rivera. I also want to dedicate this dissertation to the memory of my grandparents Ramona Santiago and Antonio Morales.

ACKNOWLEGEMENTS

I would like to express my sincere gratitude to my advisor, Dr. Peng Liu for the continuous support, patient, motivation, encouragement and invaluable guidance throughout my Ph.D. study at the University of Pittsburgh. I could have not imagined a better advisor and mentor for my Ph.D. study.

I would like to thank fellow members of the Peng Liu group: Dr. Gang Lu, Dr. Xiaotian Qi, Dr. Huiling Shao, Dr. Cheng Fang**,** Gabriel A. Cintrón-Rosado, Tuğçe Erbay, Humair Omer, Ilia Kevlishvili, Luke T. Jesikiewicz and Samantha Hong.

Also, I would like to thank all the collaborators, Prof. Paul Floreancig, Prof. Ming-Yu Ngai and Prof. Gong Chen.

My sincere thanks also go to the professors and friends that inspired me to continue this path: Dr. Ingrid Montes, Dr. Osvaldo Rosario, Dr. Zhongfang Chen, Mrs. Benitez, Sara Delgado, Juan Carlos “Juanky” and Johanna Fajardo.

Last but not least, I thank my wife, Daniela Esis-Villalobos, my parents, grandparents and brothers for their love and support. And above all thing, I would like to thank God because without him I could have not come so far.

Philippians 4:13 “*I can do all things though*
Christ who strengthens me”.

1.0 INTRODUCTION

Functionalization of C–H bonds is one of the most active areas in modern synthetic organic, organometallic, and computational chemistry. In comparison to traditional functional group manipulation methods employed in synthesis, activation of C–H bonds offers more straightforward, step-, and atom-economical synthetic routes. Many approaches have been reported in recent years utilizing this strategy, often requiring a transitional-metal catalyst.[1] Catalysts involving transition metals such as Pd, Ir, and Rh have played an important role in the functionalization of unactivated C–H bonds.[2,3] However, the use of metals and the removal of potentially toxic trace metals may incur high costs. In order to avoid the use of metals and develop more economical and environmentally benign reactions, metal-free C–H bond functionalization protocols have been developed.[4] Nevertheless, differentiating numerous C–H bonds and affecting site-specific and stereoselective chemical modification is an ongoing challenge.[5]

Although there is a plethora of applications in transition metal catalyzed C–H functionalization, metal-free approaches are relatively underdeveloped. Most of these metal-free C–H bond functionalization occurs through radical-based mechanisms.[6, 7] One example of this type of C–H bond functionalization is the $C(sp^3)$–H oxidation involving oxygen-centered radicals. The pioneering work of Murray[8] and Curci[9] demonstrated the use of dimethyldioxirane (DMDO) and methyl(trifluoromethyl)dioxirane (TFDO) for $C(sp^3)$–H oxidation without the use of transition metals.[10] The K. N. Houk research group have been involved in the study of the metal free oxidation of $C(sp^3)$–H bonds by means of computational chemistry using DFT calculations.[11]

Their calculations have shown that the DMDO activates C−H bond through a hydrogen atom abstraction mechanism to form a radical pair intermediate, which rapidly rebounds and forms the final product. However, many newly developed metal-free C−H bond functionalization reactions do not appear to occur via the radical C−H abstraction/rebound mechanism. The mechanisms in many of these processes remain unclear. The overall objective of this dissertation is to perform computational studies on the mechanisms and origins of rate and selectivity in metal-free C−H activation reactions. Calculations have been performed to investigate the reaction pathways to generate the reactive intermediates that are responsible for C−H cleavage and the mechanisms in the C−C and C−X bond forming functionalization step. The effects of reactants and reagents on reactivity and selectivity will also be investigated. In this dissertation the following three specific reactions are investigated.

1. DDQ-mediated oxidative C-H bond functionalization. Quinones are powerful oxidants which perform many useful reactions under relatively mild conditions. Within this class, 2,3-dichloro-5,6-dicyano-1,4-benzoquinone (DDQ) represents one of the more versatile reagents since it combines high reactivity in oxidation with relative stability. DDQ is widely used in the dehydrogenation of hydrocarbons and carbonyl compounds, oxidation of alcohols, phenolic cyclization and coupling reactions. Recently, DDQ has been successfully used by the Floreancig group to functionalize C−H bond through formation of carbocation via carbon-hydrogen bond oxidation and subsequent C-C bond formation (**Figure 1-1**).[12] Chapter 2 discusses the computational study of the C−H bond activation by DDQ to form new C−C bonds under metal-free conditions. A reactivity predictive model was generated from the computational mechanistic insights.

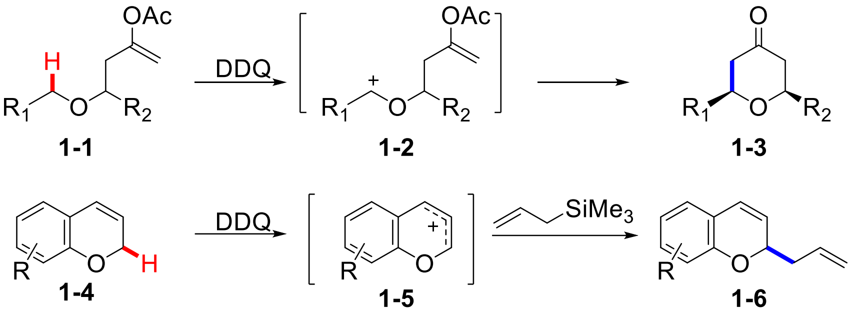

Figure 1-1. C-C bond formation through oxidative C-H activation.[12]

2. C–H bond functionalization mediated by hypervalent iodine reagents. In addition to DDQ, hypervalent iodine compounds have shown promising reactivity to functionalize unactivated C–H bonds. Among these compounds, cyclic derivatives stand apart because of their enhanced stability.[13] They are commonly used as oxidants, but their potential for functional-group transfer has only begun to be investigated recently. The use of benziodoxol(on)es for trifluoromethylation (Togni's reagents) is already widely recognized, but other transformations have also attracted strong interest. In 1996, Zhdankin reported that the reaction of simple hydrocarbons with **1-8** in the presence of benzoyl peroxide led to selective azidation of 3° and activated 2° C–H bonds in moderate to good yield (**Figure 1-2a**).[14,15,16] Hartwig in 2015 reported that Fe/PyBOX catalysts promote aliphatic C–H azidation with **1-8** under milder conditions, allowing the functionalization of complex natural products with high selectivity (**Figure 1-2a**).[17] Recently, the Gong Chen research group reported a metal-free approach for the azidation of tertiary aliphatic C–H bonds under visible light using a photo-redox catalyst and **1-8** reagent. In addition to the azidation of tertiary C–H bonds, they developed two new reactions for the halogenation of tertiary C–H bonds (**Figure 1-2b**).[18] In 2017, Chen reported an efficient and broadly applicable photoredox-catalysis strategy for the selective hydroxylation of tertiary and benzylic C−H bonds using **1-16** as oxidant and H_2O as cosolvent and hydroxylation reagent (**Figure 1-1c**).[94]

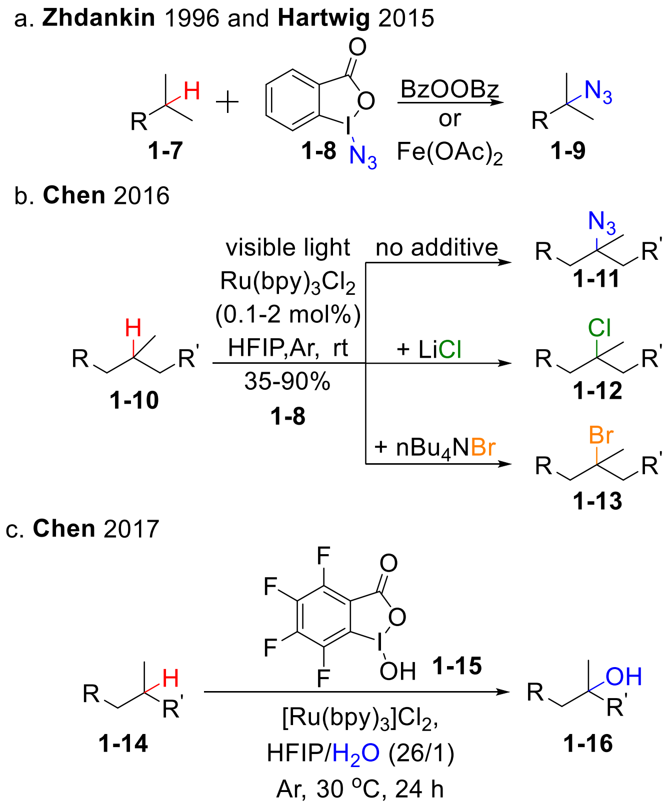

Figure 1-2. Selective functionalization of C-H bond with hypervalent iodine reagents.

In addition, these cyclic hypervalent iodine reagents have been used to promote Minisci-type C−H alkylation reactions and an unusual epimerization reaction of stereogenic tertiary carbon centers (**Figure 1-3**). The Minisci reaction is a known strategy for alkylation of heteroaromatic C−H bonds through a radical substitution.[19] However, the classical Minisci requires harsh reaction conditions. The Chen research group reported the first photoredox-mediated Minisci C−H alkylation reaction of *N*-heteroarenes with a variety of easily accessible primary and secondary alkyl boronic acids using a hypervalent iodine reagent as radical initiator (**Figure 1-3a**).[20] Racemization or epimerization of stereogenic tertiary carbon centers via reversible cleavage of C−H bonds could offer an invaluable tool for editing the stereochemistry of organic compounds. In this aspect, Chen[95] reported, in 2018, an efficient and synthetically useful protocol for epimerizing tertiary carbons via radical cleavage of nonacidic 3° C(sp3)−H bonds with hypervalent iodine reagent benziodoxolone azide (**1-8**) under mild conditions (**Figure 1-3b**). Chapters 3 and 4 will discuss the mechanisms and the role of different hypervalent iodine reagents on the reactivity and selectivity.

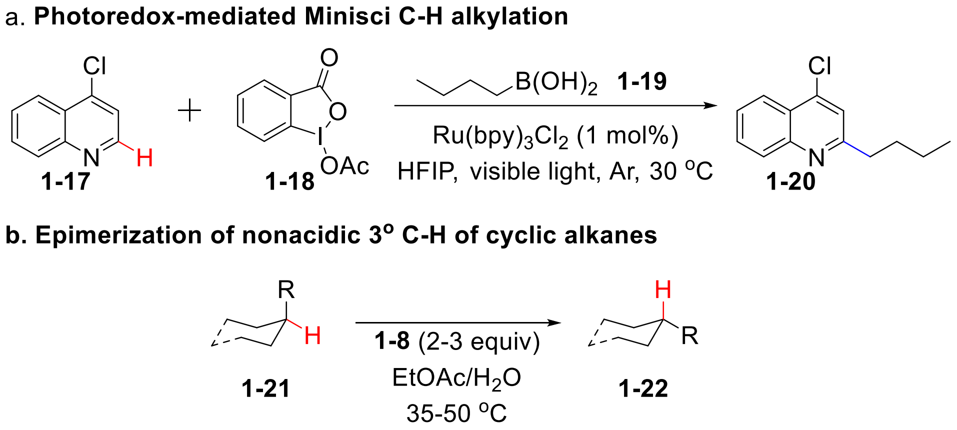
a. **Photoredox-mediated Minisci C-H alkylation**

b. **Epimerization of nonacidic 3° C-H of cyclic alkanes**

Figure 1-3. (a) Photoredox-mediated Minisci C−H alkylation and (b) eoimerization of nonacidic 3° C−H of cyclic alkyanes with hypervlaent iodine molecules.

3. C−H bond tri- and difluoromethoxylation of arenes and heteroarenes. Tri- and difluoromethoxylation of arenes and heteroarenes are of great importance in medicinal chemistry. Although a number of prescribed pharmaceutical agents bear OCF_3 or OCF_2H motifs in an aromatic system, access to such analogues often requires the installation of these groups at the early stage of a multi-step synthetic sequence. In this aspect, the Ngai research group developed a C−H trifluoromethoxylation of (hetero)arenes *via* OCF_3-migration using Togni's reagents. In order to develop better synthetic strategies for the C−H tri- and difluoromethoxylation of arenes and heteroarenes, the Ngai research group synthetized novel OCF_3- and OCF_2H-reagents taking advantage of the relatively weak $N{-}OCF_3$ and $N{-}OCF_2H$ bonds (**Figure 1-4**). Chapter 5 describes a computational study on the mechanisms of the C−H tri- and difluoromethoxylation of arenes and heteroarenes.

a. Trifluoromethoxylation of arenes by OCF3 migration

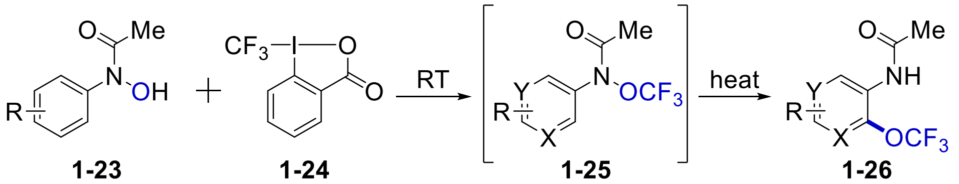

b. Tri and difluoromethoxylation of heteroarenes and arenes using OCF_3- and OCF_2-reagents.

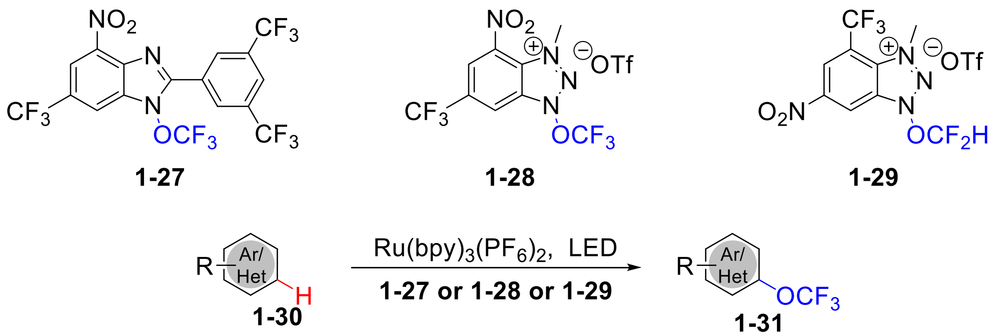

Figure 1-4. Tri- and difluoromethoxylation of arenes and heteroarenes via (a) OCF_3 migration and (b) using OCF_3 and OCF_2-reagents.

Computational Methods. The computational studies of these metal-free C−H functionalization reactions were performed using density functional theory (DFT) in Gaussian 09. DFT offers a reasonable accuracy required for the studies described here and a good balance between accuracy and cost as compared with wave function theory (WFT) methods. The previously commonly density functional, B3LYP, has some serious limitations. For example, it gives worse performance for transition metal complexes than for main-group chemistry [21];

secondly, it systematically underestimates reaction barrier heights[22]; and finally it is inaccurate for interactions dominated by medium range correlation energy, such as van der Waals attractions, aromatic-aromatic stacking, and alkane isomerization energies. In order to address these problems, a number of new functionals, such as the M06[23] family functionals, were developed. While B3LYP belongs to a meta-GGA type of functional, M06-2X is a hybrid-meta-GGA functional. Based on the Jacob's ladder hybrid-meta-GGA functionals belong to a higher rank of functional which performance is expected to be better than hybrid-GGA.[24] Calculations presented in this dissertation were performed by using M06-2X functional since it offers more reliable results for main group chemistry.[25] The SMD solvation model were generally used for single point energy calculations. On average, SMD provides better results than earlier versions of implicit solvation models due to parameterization of atomic radii and short-range non-electrostatic interactions.[26] The specific functional, basis set, and other computational details used in each project are provided in the following chapters.

2.0 COMPUTATIONAL STUDIES OF OXIDATIVE C−H BOND ACTIVATION BY DDQ

Reproduced with permission from Cristian A. Morales-Rivera, Paul E. Floreancig, and Peng Liu, “Predictive Model for Oxidative C−H Bond Functionalization Reactivity with 2,3-Dichloro-5,6-dicyano-1,4-benzoquinone”, *J. Am. Chem. Soc*. **2017**, *139*, 17935-17944. Copyright 2017, American Chemical Society. In this work, I designed and carried out DFT calculations and analysis of computational results.

2.1 INTRODUCTION

Carbon–hydrogen bond functionalization reactions can greatly facilitate chemical synthesis due to their capability to increase molecular complexity from readily available starting materials with minimal waste generation.[27] These processes are most often achieved through transition metal catalysis, though metal-free approaches for such reactions are becoming increasingly common. 2,3-Dichloro-5,6-dicyano-1,4-benzoquinone (DDQ) is a mild yet effective reagent for promoting oxidative C−H bond cleavage.[28,29,30] This reagent is most commonly employed to cleave benzylic and allylic ethers through oxidative oxocarbenium ion formation followed by hydrolysis.[28c] These oxocarbenium ions can also be trapped with an intra- or intermolecular nucleophilic addition to generate carbon−carbon[29,30] (**Figure 2-1**) and carbon−heteroatom bonds.[31] This process is tolerant of numerous functional groups and has been used in late stages of natural product syntheses.[32]

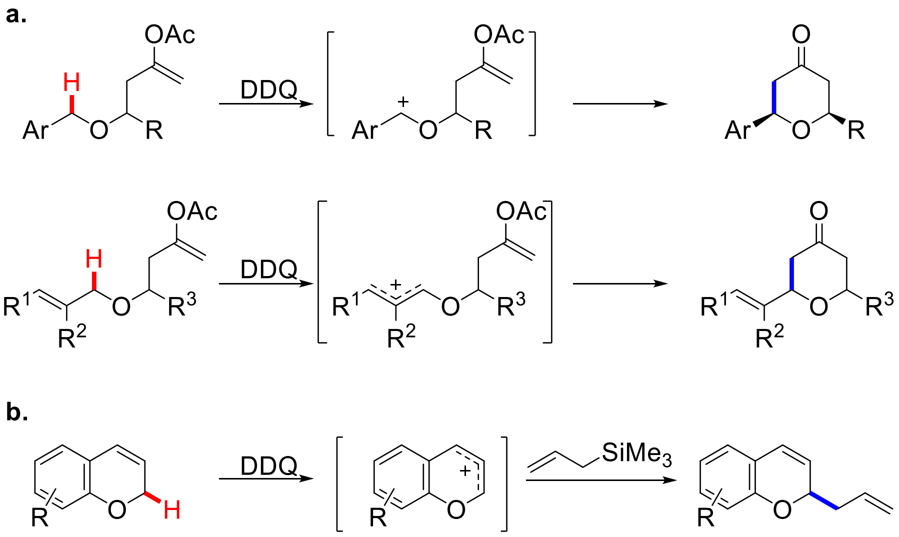

Figure 2-1. Selected examples of DDQ-mediated (a, b) intra- and (c) intermolecular carbon−carbon bond formation reactions through the oxidation of carbon−hydrogen bond.[12]

DDQ-mediated C–H functionalization has been performed on a wide variety of substrates, with specific examples being illustrated in **Figure 2-2**. The rates of these reactions commonly correlate with the stabilities of the carbocation intermediates. For example, benzylic C−H bond cleavages are promoted by electron-donating substituents (**Figure 2-2a**).[29a] Internal allylic substrates are much more reactive than terminal allylic substrates (**Figure 2-2b**).[29a] Additionally, the reactivity is significantly enhanced by the formation of aromatic carbocation intermediates, as seen in the reaction of **2-9** (**Figure 2-2c**).[29g] Attributing the kinetics of C–H bond cleavage solely to carbocation stability, however, is inconsistent with the difference in reactivity between alkenyl and allylic ethers (**Figure 2-2d**).[33] Although alkenyl ether **2-13** and allylic ether **2-15** react with DDQ to provide the same oxocarbenium ion, the cyclization of **2-13** is significantly faster. This is particularly notable in consideration of the greater stability of **2-13** relative to **2-15** and indicates that substrate oxidation potential also influences reaction rate.

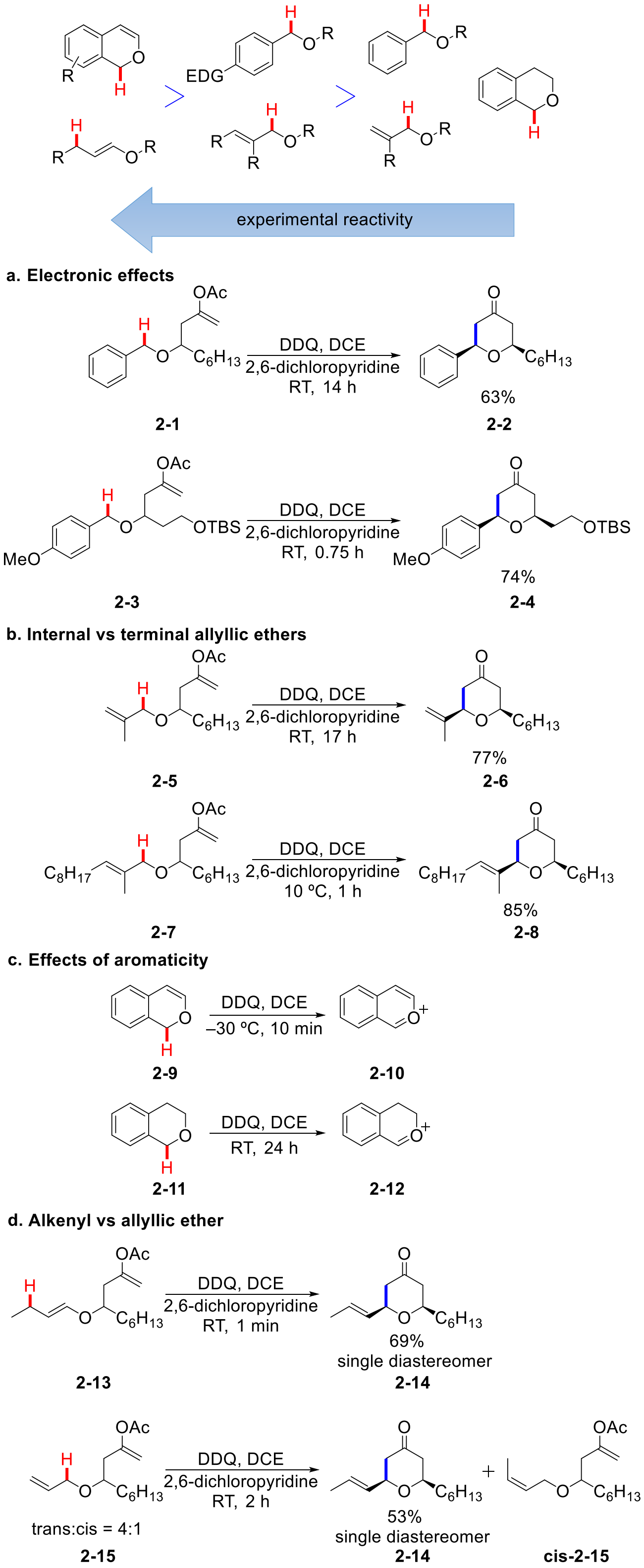

Figure 2-2. Experimental reactivity trend of different C−H Bonds in DDQ-mediated oxidative coupling reactions.[29a,29g,33]

Clearly, a thorough understanding of the mechanisms of the DDQ-mediated C−H cleavage is necessary to elucidate the origin of reactivity. Four different mechanisms have been proposed for DDQ-mediated oxidative C–H bond cleavage reactions (**Figure 2-3**). A single electron transfer (SET) from the substrate to DDQ can form a charge transfer complex of a radical cation with DDQ$^{\bullet-}$ followed by hydrogen atom transfer (HAT) to form a carbocation and DDQH^{-}.[34,35] This mechanism is consistent with the importance of oxidation potential on the reaction rate but is not consistent with the relatively modest reduction potential of DDQ.[36] Alternatively, hydrogen atom transfer (HAT) from the substrate to DDQ can form an alkyl radical followed by single electron transfer to form the same carbocation. This mechanism, proposed by Rüchardt based on the trapping of the intermediary radicals by nitrosobenzene,[37] is unlikely because the known lack of substituent effects on benzylic C–H bond strengths[38] is contrary to the observed influence of cation-stabilizing substituents on reaction rates, and kinetic isotope effects clearly show that C–H bond cleavage is the rate-determining step.[39] A one-step hydride transfer to the oxygen atom on DDQ (O-attack) can directly form a zwitterionic complex of DDQH^{-} with carbocation, as proposed by Linstead and Jackman.[40] Hydride transfer to the carbon atom attached to the cyano group on DDQ (C-attack) followed by aromatization to form DDQH^{-} can generate the same carbocation.[41] The observed correlation between intermediate cation stability and reaction rate supports the direct hydride transfer mechanisms, though this pathway does not explain the observed importance of substrate oxidation potential. DFT calculations from Chan and Radom,[42] Mayr and Zipse,[41] and others[43,44] suggest that the most favorable pathway in the dehydrogenation of 1,4-cyclohexadiene in polar solvent is the concerted hydride transfer via O-attack. However, the mechanism of reactions with other C−H hydride donors, including benzylic and allylic ethers, and the origin of substituent effects on rates have yet to be investigated computationally.

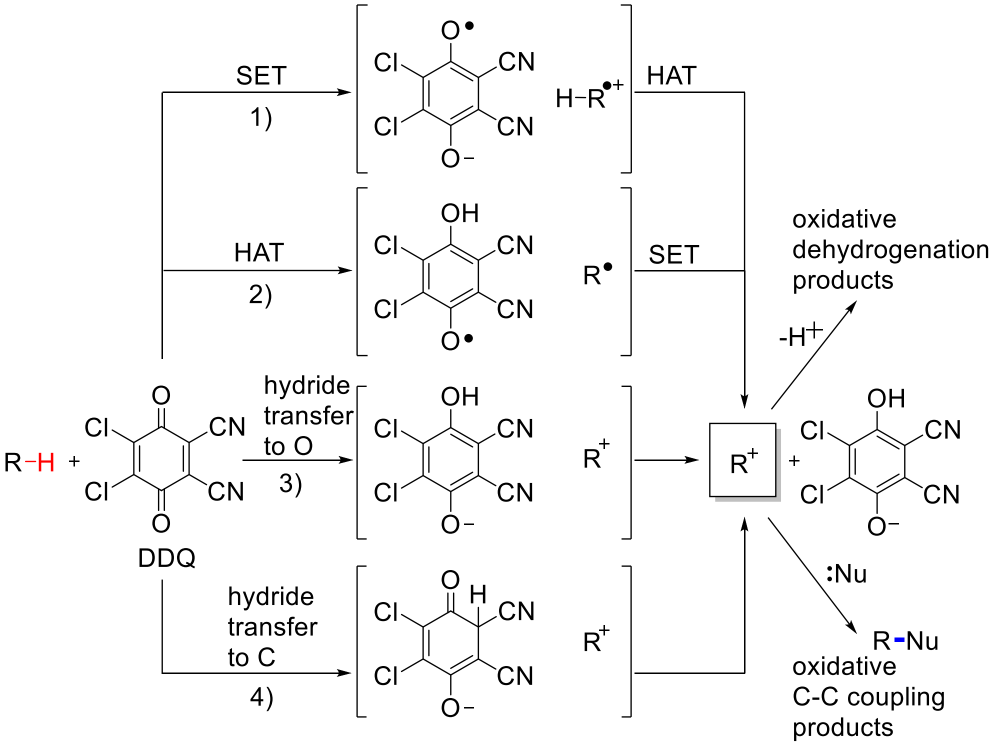

Figure 2-3. Possible mechanisms of DDQ-mediated C−H cleavage.

This chapter describes a computational study on the mechanism and origin of reactivity of a wide variety of C–H bonds in the DDQ-mediated oxidative C–C coupling reactions. The four pathways shown in **Figure 2-3** were analyzed computationally to elucidate the most favorable mechanism for C–H bond cleavage. A thorough theoretical analysis of the transition state interactions was then performed to reveal the main factors that dictate the reactivity. These theoretical insights and the DFT-computed barriers were utilized to establish a two-variable mathematical equation to predict the rate of the C–H cleavage from the hydride dissociation energy (HDE)[45] and the oxidation potential of the substrate.

2.2 COMPUTATIONAL DETAILS

All calculations were performed with Gaussian 09.[46] Images of the 3D structures of molecules were generated using CYLView.[47] The geometries of all intermediates and transition states were optimized with the M06-2X[48] functional and the 6-31G(d) basis set. Single point energy calculations were performed with M06-2X and the 6-311++G(d,p) basis set. Solvent is expected to impact both the optimized geometries and the energies of the hydride transfer transition states and the zwitterionic complexes. Solvation effects were considered by applying the SMD[49] solvation model with dichloroethane (DCE) solvent in both geometry optimization and single point energy calculations. Thermal corrections to the Gibbs free energies and enthalpies were calculated using the harmonic oscillator approximation at 298K. All energies in the reaction energy profiles are with respect to the separated reactants. Each structure reported is the lowest energy conformer as indicated by calculations. The activation free energies of the outer-sphere single electron transfer reactions were calculated from Marcus theory.[50] Oxidation potentials were calculated from the reaction Gibbs free energies of the oxidation half-reactions in DCE solution (see section 2.4).[36c,51]

2.3 RESULTS AND DISCUSSION

2.3.1 Mechanisms of DDQ-Mediated C−H Benzylic Ether Functionalization

The single electron transfer (SET), hydrogen atom transfer (HAT), and the O- and C-attack hydride transfer pathways of the C–H cleavage step in the reaction between DDQ and benzylic ether **2-16** were first studied. The computed activation energies and reaction energies are shown in **Figure 2-4**. The O-attack hydride transfer is the most thermodynamically favorable pathway to form the carbocation intermediate **2-21** and DDQH^{-} (**22**) with a reaction Gibbs free energy of −10.8 kcal/mol. The C-attack pathway to form the same carbocation **2-21** and the less stable nonaromatized DDQH^{-} isomer **2-23** is slightly endergonic by 4.6 kcal/mol. The SET and HAT pathways are all much more endergonic, with reaction Gibbs free energies of 20.7 and 13.9 kcal/mol, respectively. The activation Gibbs free energy of the SET pathway was calculated using Marcus theory. The barrier to the outer-sphere single electron transfer from **2-16** to DDQ ($\Delta G^{\ddagger}$ = 22.6 kcal/mol) is higher than both the O- and C-attack hydride transfer pathways. H-atom abstraction can also be discarded because an open-shell HAT transition state cannot be located in solution. Instead, such calculations lead to the more stable closed-shell hydride transfer transition state.[52] These results indicate that the two hydride transfer pathways (O-attack and C-attack) are the most favorable mechanisms for the DDQ-mediated benzylic C−H cleavage.

The Gibbs free energies of activation of the outersphere single electron transfer (OSET) in reactions with **2-16** and **2-28** were calculated using Marcus theory. The calculation of the OSET from **2-16** is shown below as an example. The same steps were taken to calculate the OSET barrier for substrate **2-28**.

$$\textbf{2-16} + \text{DDQ} \leftrightarrow \textbf{2-16}^{\bullet +} + \text{DDQ}^{\bullet -}$$

Based on Marcus theory, the[53] activation Gibbs free energy of the outersphere single electron transfer can be calculated from:

$$\Delta G^{\ddagger}_{OSET} = \Delta G^{\ddagger}_{0}\left(1 + \frac{\Delta_r G^{\ominus}}{4\Delta G^{\ddagger}_{0}}\right)$$

Here, $\Delta_r G^{\ominus}$ = 20.7 kcal/mol is the reaction energy of the OSET obtained from DFT calculations. $\Delta G^{\ddagger}_{0}$ is calculated from

$$\Delta G^{\ddagger}_{0} = (\lambda_i + \lambda_0)/4$$

The inner reorganization energy λ_i is expected to be small, and thus is neglected in the calculations. The solvent reorganization energy λ_0 is calculated as follows:

$$\lambda_0 = 95\left[(2r_{16})^{-1} + \left(2r_{DDQ}\right)^{-1} - (r_{16} + r_{DDQ})^{-1}\right] = 95\left(\frac{1}{2 \times 4.3} + \frac{1}{2 \times 4.1} - \frac{1}{4.3 + 4.1}\right)$$
$$= 11.4 \text{ kcal/mol}$$

Here, the radii of **2-16** and DDQ (4.3 and 4.1 Å, respectively) were derived from the molecular volume calculated from the "volume" keyword in Gaussian 09. After obtaining the molecular volumes, the radii were derived assuming the shapes of the molecules are perfect spheres.

Thus, $\Delta G^{\ddagger}_{0} = \lambda_0/4$ = 2.9 kcal/mol and $\Delta G^{\ddagger}_{OSET} = 2.9 \times \left(1 + \frac{20.7}{4\times 2.9}\right) = 22.6 \text{ kcal/mol}$

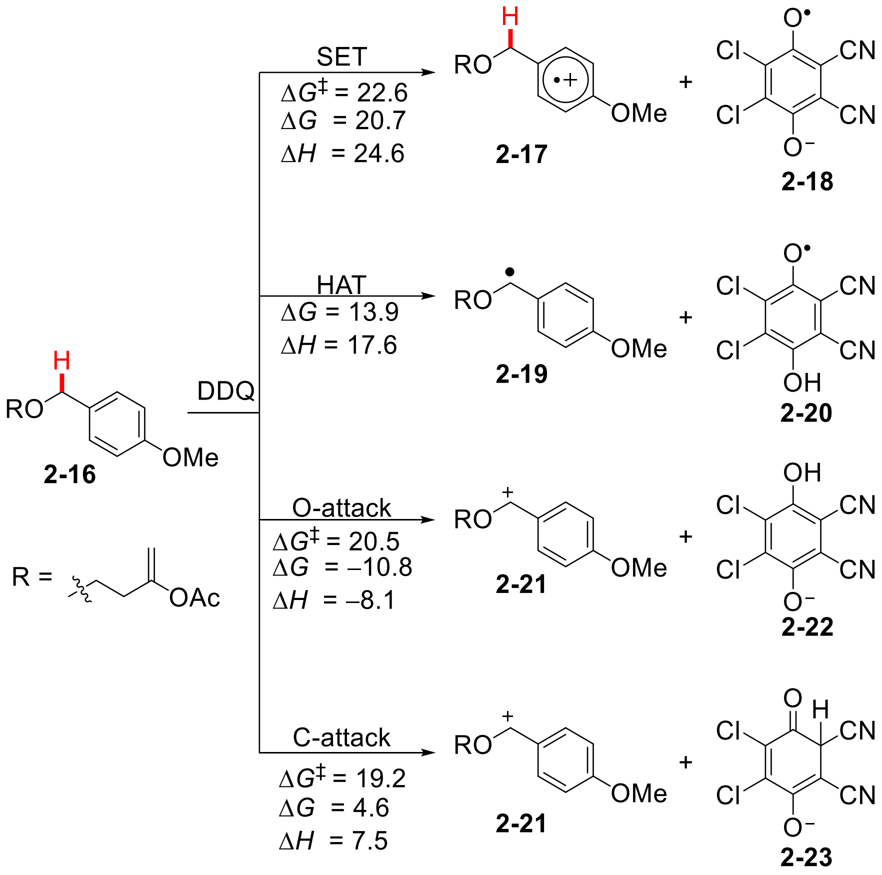

[a] All energies are in kcal/mol with respect to the separate reactants (**16** and DDQ).

Figure 2-4. Activation and reaction energies of competing C−H cleavage pathways in the reaction of DDQ and benzylic ether 2-16[a].

The complete reaction energy profiles of the two hydride transfer pathways in the oxidative cyclization of benzylic ether **2-16** are shown in **Figure 2-5A**. DDQ first coordinates with **2-16** to form a charge-transfer complex **2-24**. Natural population analysis (NPA) calculations show the total atomic charges of the DDQ fragment is −0.110 *e* (**Figure 2-5B**), indicating that complex **2-24** is stabilized by a small amount of charge transfer from the substrate to DDQ. From **2-24**, the hydride from the benzylic C–H bond may be transferred to either the carbonyl oxygen on DDQ (O-attack, **2-TS2**, $\Delta G^{\ddagger}$ = 20.5 kcal/mol) or the cyano-substituted carbon on DDQ (C-attack, **2-**

TS1, $\Delta G^{‡}$ = 19.2 kcal/mol). The C-attack pathway requires a slightly lower barrier than the O-attack pathway. This contrasts with the DDQ-mediated C−H oxidation of 1,4-cyclohexadiene, in which the O-attack is favored by 2.2 kcal/mol.[41] NPA calculations revealed significant amounts of electron transfer from the substrate to DDQ in both C- and O-attack transition states (0.746 and 0.742 *e* in **2-TS1** and **2-TS2**, respectively). This is consistent with the nature of the hydride transfer process. The proximity of the negatively charged DDQ and the positively charged aryl moiety of the substrate suggests that the hydride transfer transition state is stabilized by the electrostatic interactions between DDQ and the benzylic ether substrate (see below for detailed discussions of factors that determine reactivity).

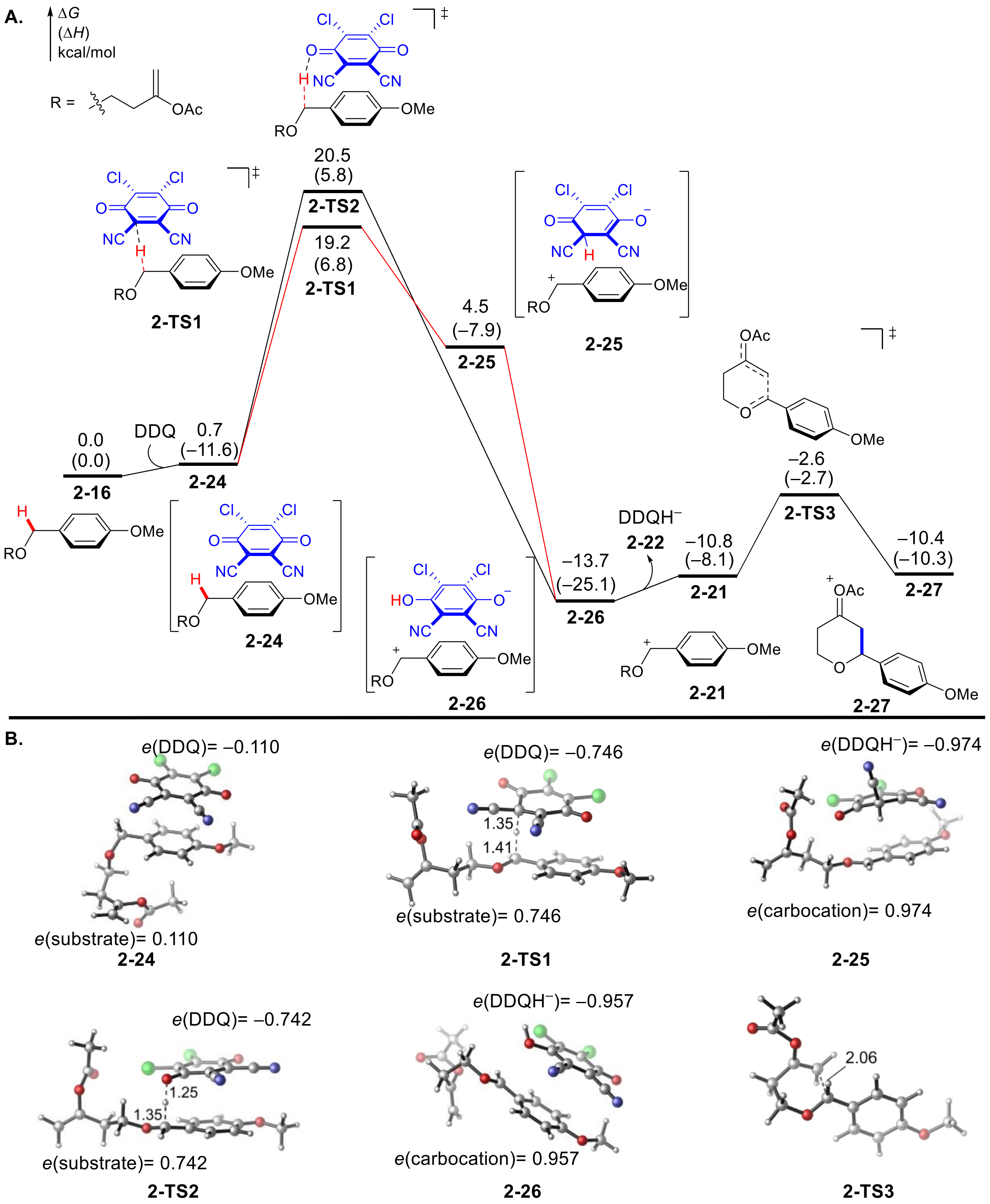

Figure 2-5. A. Energy profile of the DDQ-mediated intramolecular oxidative C−C coupling of benzylic ether 2-16. B. 3D structures of key intermediates and transition states.

The C- and O-attack hydride transfer transition states lead to zwitterionic complexes of the benzylic cation with two isomers of DDQH$^-$ (**2-25** and **2-26**, respectively). Tautomerization of the nonaromatized isomer of DDQH$^-$ in **2-25** forms the much more stable isomeric complex **2-26**. Dissociation of the carbocation **2-21** from the zwitterionic complex **2-26** followed by intramolecular nucleophilic addition forms a new C–C bond (**2-27**) via a cyclization transition state (**2-TS3**). This nucleophilic C–C bond formation has a lower barrier than the C–H cleavage via **2-TS1** or **2-TS2**. Thus, the hydride transfer is the rate-determining step of the overall transformation, in agreement with the primary KIE observed in experiment.[39] Finally, acylium ion loss from **2-27** will lead to the cyclic ketone product. This final step in the oxidative C–C coupling reaction is expected to be facile and exothermic, and thus was not investigated computationally.

2.3.2 Mechanisms of DDQ-Mediated C−H Functionalization of an Allylic Ether

The four mechanistic pathways using allylic ether **2-28** as the substrate were studied next. The computed reaction energies of the single electron transfer (SET), hydrogen atom transfer (HAT), and two different hydride transfer pathways (O-attack and C-attack) are shown in **Figure 2-6**. Similar to the reaction with benzylic ether **2-16**, the most thermodynamically favorable pathway is through a one-step hydride transfer to form the carbocation intermediate **2-31** and DDQH$^-$ (**2-22**). The activation free energy of the SET pathway derived from the Marcus theory is also higher than the hydride transfer pathways.

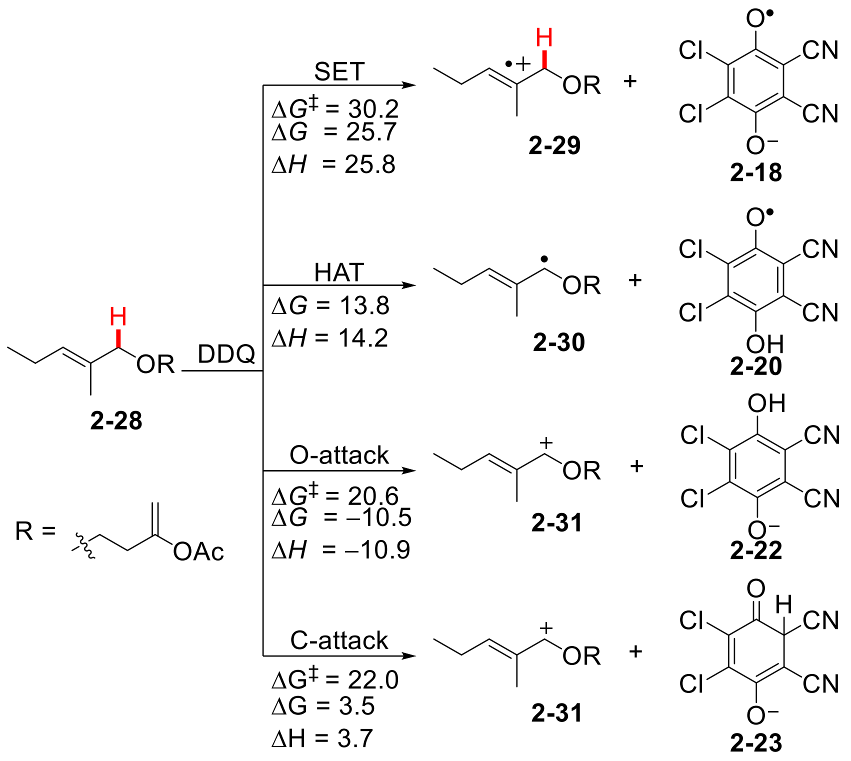

[a] All energies are in kcal/mol with respect to the separate reactants (**2-28** and DDQ).

Figure 2-6. Activation and reaction energies of competing C−H cleavage pathways in the reaction of DDQ and allylic ether 2-28[a].

The computed energy profile of the two hydride transfer pathways in the oxidative cyclization of **2-28** (**Figure 2-7A**) indicated a mechanism similar to that with benzylic ether **2-16**. DDQ first coordinates with **2-28** to form a charge-transfer complex **2-32**. NPA calculations show the charge transfer from **2-28** to DDQ in complex **2-32** is slightly less significant than that in the complex with benzylic ether (−0.062 *e* and −0.110 *e* in **2-32** and **2-24**, respectively). In addition, the charge transfer in the hydride transfer transition states **2-TS4** and **2-TS5** is also less significant than that in **2-TS1** and **2-TS2**. This is consistent with the lower polarizability and higher oxidation potential of **2-28**. The O-attack hydride transfer (**2-TS4**) is favored by 1.4 kcal/mol, in contrast to the reaction with benzylic ether **2-16** that favors the C-attack. The carbocation resulting from the hydride transfer (**2-31**) then undergoes intramolecular nucleophilic attack (**2-TS6**) to form a new C−C bond in intermediate **2-35**.

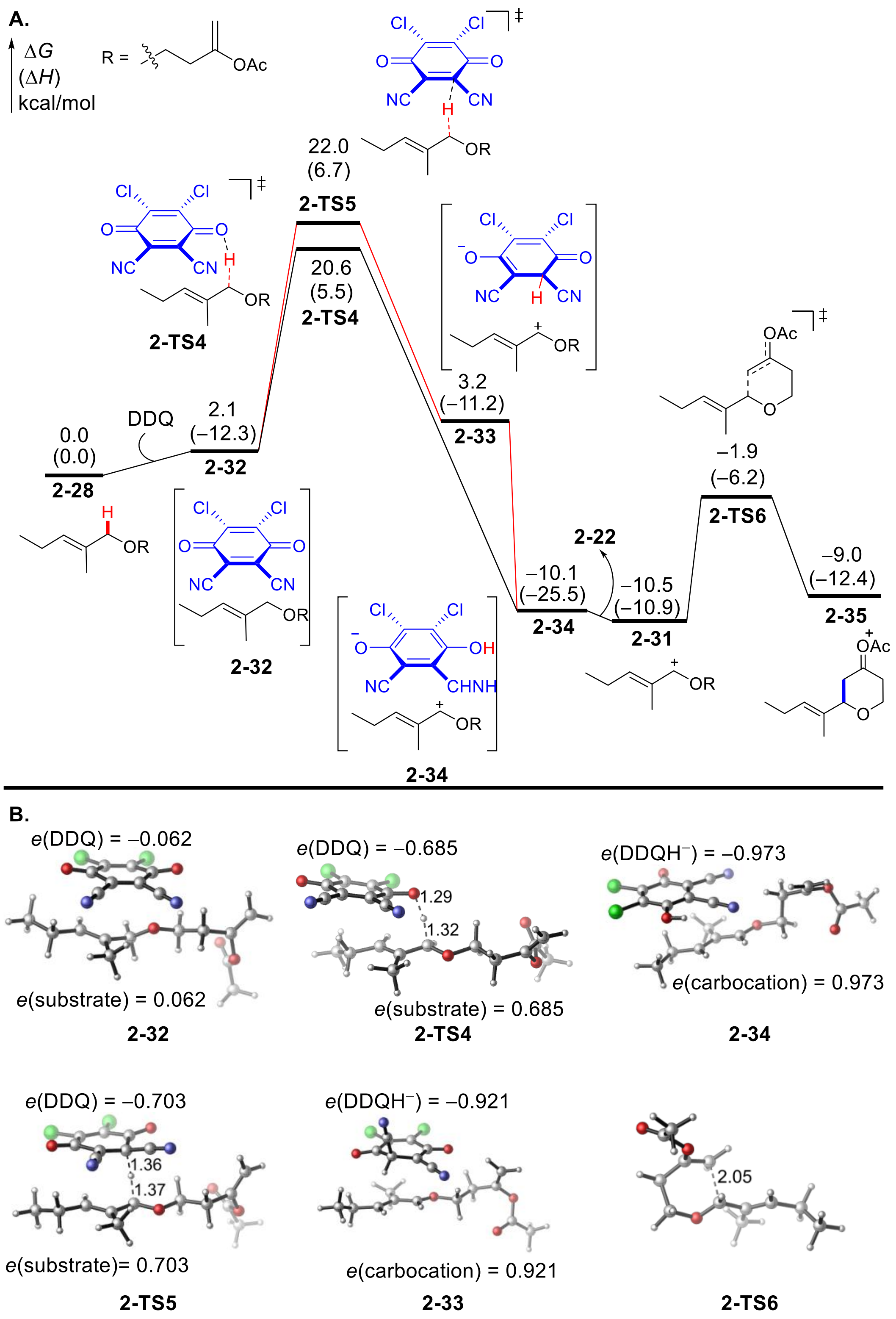

Figure 2-7. A. Energy profile of the DDQ-mediated intramolecular oxidative C−C coupling of allylic ether 2-28. B. 3D structures of key intermediates and transition states.

In summary, the DFT calculations revealed that the most favorable mechanism of the DDQ-mediated C−H cleavage of benzylic and allylic ethers is a one-step hydride transfer from the charge-transfer complex of the substrate and DDQ. Two competing pathways involving hydride transfer to the oxygen and carbon atoms on DDQ, namely O- and C-attack, respectively, have similar activation energies. This indicates that both mechanisms need to be considered in the computational investigation of reactivities of different substrates.

2.3.3 Effects of the Stability of the Carbocation Intermediate on the Reactivity of C−H Cleavage

Activation energies of the O- and C-attack hydride transfer pathways of various benzylic ether, allylic ether, and alkenyl ether substrates were computed in order to explore the origin of substituent effects on reactivity (**Table 2-1** and **Figure 2-8**). Even though large variations of the computed activation energies were observed among the substrates, the O- and C-attack pathways for a given substrate are always competitive. The reaction energies to generate the carbocation intermediate and $DDQH^-$ were also computed. In agreement with the experimentally observed trend, the stability of the carbocation plays an important role on the rate of the C−H bond cleavage. For example, the *para*-methoxy substitution stabilizes the carbocation intermediate and increases the reactivity of benzylic ether **2-16** compared to **2-36** (entries 1 and 2 in **Table 2-1** and **Figure 2-8a**). The reaction of internal allylic ether **2-28** is more exergonic and has a lower barrier than that of terminal allylic ether **2-37** (entries 3 and 4 in **Table 2-1** and **Figure 2-2b**). Forming an aromatic cation is highly thermodynamically favorable and leads to significantly increased reactivity of **9** and **38** (entries 5-7 in **Table 2-1** and **Figure 2-2c**). The stabilities of the intermediate carbocations are significant due to the capacity of these species to engage in bimolecular carbon–carbon bond forming reactions with allylic silanes and potassium alkenyl- and alkynyltrifluoroborates.[29g]

Table 2-1. Electronic effects on the activation and reaction energies of hydride transfer[a].

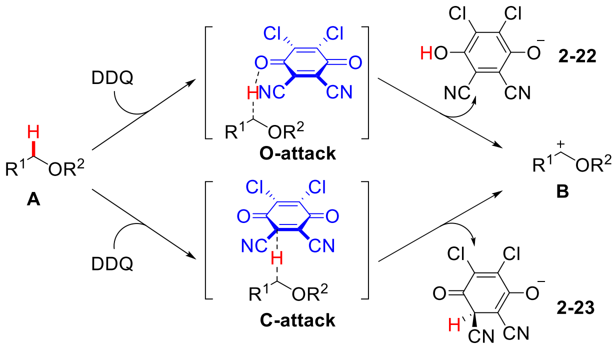

entry	substrate	O-attack $\Delta G^{\ddagger}$ [$\Delta H^{\ddagger}$]	C-attack $\Delta G^{\ddagger}$ [$\Delta H^{\ddagger}$]	$\Delta G_{(A\rightarrow B)}$ [$\Delta H_{(A\rightarrow B)}$]^{b}	$E^{0}_{1/2}{}^{c}$
1	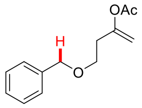 **2-36**	22.9 [10.7]	23.8 [10.2]	−6.8 [−5.3]	2.17
2	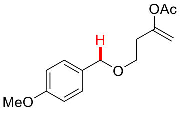 **2-16**	20.5 [5.8]	19.2 [6.8]	−10.8 [−8.1]	1.50
3	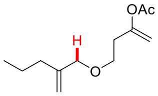 **2-37**	26.5 [10.7]	26.1 [12.4]	−4.9 [−5.0]	2.21
4	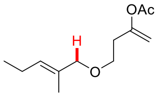 **2-28**	20.6 [5.5]	22.0 [6.7]	−10.5 [−10.9]	1.73
5	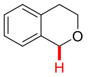 **2-11**	24.9 [11.1]	25.0 [11.3]	−7.4 [−6.8]	2.08
6	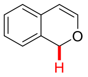 **2-9**	19.0 [5.8]	17.9 [4.8]	−12.8 [−12.2]	1.19
7	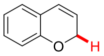 **2-38**	18.6 [4.7]	20.4 [7.0]	−15.2 [−15.0]	1.29

a All energies are in kcal/mol with respect to the separate reactants (A and DDQ). b the reaction energy of **A** and DDQ to form **B** and **2-22**. c Oxidation potential in V vs SCE (for more information refer to section 2.4)

Steric repulsions and ring strain can also destabilize the carbocation intermediate and impede hydride transfer. In the reactions shown in **Figure 2-8A**, *cis*-allylic ether **2-40** is less reactive than the corresponding *trans*-isomer **2-39** due to the unfavorable A^{1,3}-strain in carbocation **2-46**. This agrees with the lower reactivity of *cis* allylic ethers in experiment (**Figure 2-2d**). The cyclic allylic ether **2-41** is much less reactive than the acyclic allylic ethers **(2-39** and **2-40**), because the hydride transfer to form **2-48** is much less exergonic. This is attributed to the increased ring strain of the cyclic allylic cation **2-48**. The same reactivity trend is observed for alkenyl ethers. The *trans* isomer **2-42** is more reactive than the *cis* isomer (**2-43**) and the cyclic alkenyl ether **2-44** is the least reactive (**Figure 2-8B**).

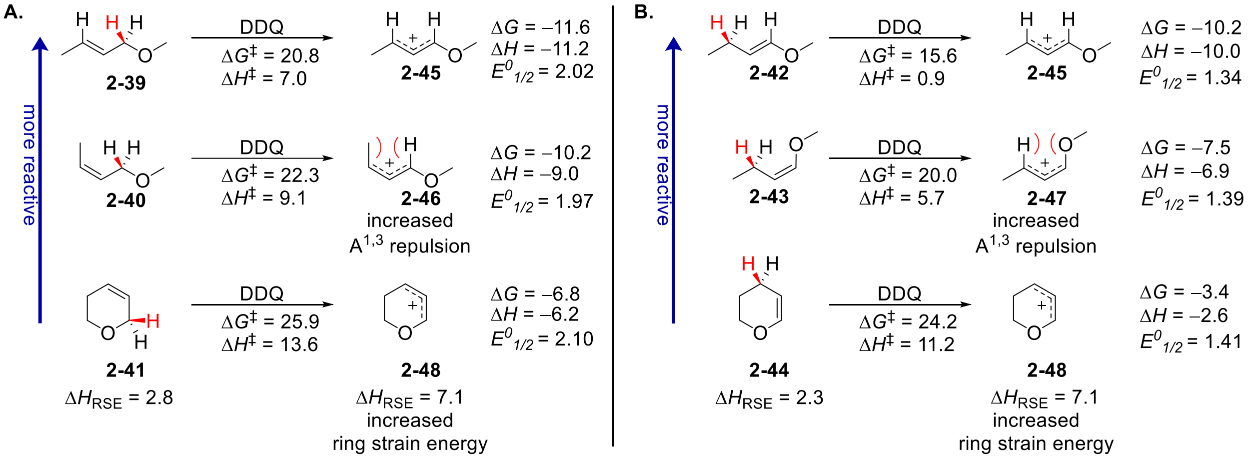

Figure 2-8. Effects of steric repulsions and ring strain energy on the reactivity of (A) allylic and (B) alkenyl ethers. All energies are in kcal/mol. Oxidation potential in V vs SCE (for more information refer to section 2.4).

Homodesmotic reaction were used to the determine the ring strain energies of substrates **2-41**, **2-44**, and the carbocation intermediate **2-48** (**Figure 2-9**). These types of reactions are chemical equations in which the reactants and products contain equal numbers of carbon atoms in the same state of hybridization and equal numbers of CH_3, CH_2, and CH groups being a reliable way for calculating ring strain energy.

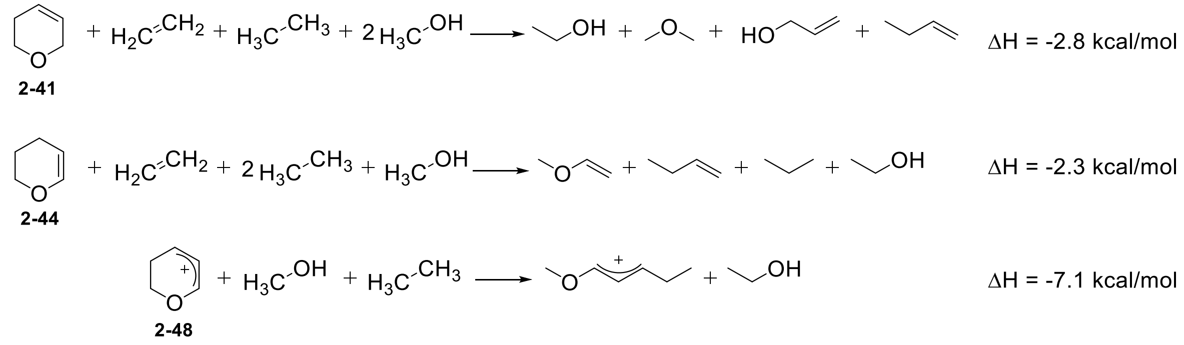

Figure 2-9. Homodesmotic reactions for the determination of ring strain energies of substrates 2-41, 2-44, and the carbocation intermediate 2-48.

The above discussions clearly indicated the importance of the stability of the carbocation intermediate on the rate of C−H bond cleavage. Nonetheless, a few notable outliners indicate that other factors also contribute to the observed reactivity trend. The reactions of alkenyl ether **2-13** and allylic ether *trans*-**2-15** generate the same oxocarbenium ion after the hydride transfer (**Figure 2-2d**). Thus, the hydride transfer from **2-13** should be less exergonic than that from **2-15** because of the greater thermodynamic stability of alkenyl ethers relative to allylic ethers. However, **2-13** reacts much faster. Here, the reactivity trend is opposite to the thermodynamic driving force of hydride transfer. These experimental observations are confirmed by the DFT calculations shown in **Figure 2-8**. The hydride transfer from the alkenyl ether **2-42** has much lower activation energy than that from the allylic ether **2-39**, despite being less exergonic.

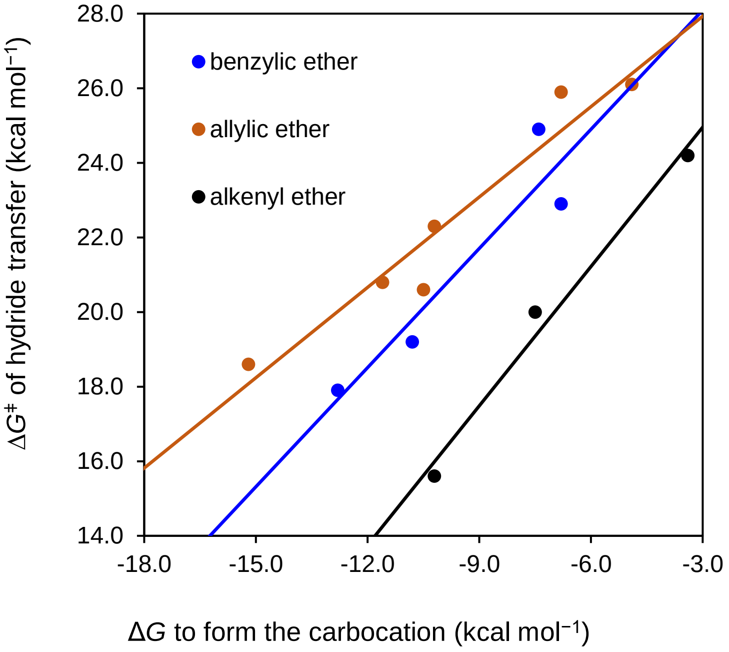

Figure 2-10. Activation energies (Δ*G*‡) and reaction energies (Δ*G*) of hydride transfer with three different types of substrates.

The relationship between the activation energy and the reaction energy of the hydride transfer of the substrates discussed above is illustrated in **Figure 2-10**. Within each type of substrate (benzylic, allylic, or alkenyl ethers), a good correlation was obtained − the more stable carbocation leads to a lower activation energy. When comparing different types of substrates, alkenyl ethers are substantially more reactive than the other two types of substrates if the reaction energy to form the carbocation is comparable. Thus, the stability of the carbocation itself is not adequate for establishing a generally applicable model for reactivity. These results prompted us to perform a detailed analysis on the origin of the increased reactivity of alkenyl ethers and to reveal other factors that affect the reactivity of the DDQ-mediated C−H bond cleavage.

2.3.4 Origin of the Increased Reactivity of Alkenyl Ethers

Several factors may stabilize the hydride transfer transition states and thus increase the reactivity of alkenyl ethers, including electrostatic attraction[54] and secondary orbital interactions[55] between DDQ and the substrate. A detailed computational analysis on these possible factors in the O- and C-attack transition states with alkenyl ether **2-42** and allyllic ether **2-39** was performed (**Figure 2-11**). Distortion/interaction energy analysis[56] indicates the hydride transfer transition states with alkenyl ether (**2-TS7** and **2-TS9**) are stabilized by the stronger interaction energy[57] between DDQ and the alkenyl ether (ΔE_{int} = −30.6 and −40.1 kcal/mol in **2-TS7** and **2-TS9**, respectively). In contrast, the interaction energies between DDQ and the allylic ether in **2-TS8** and **2-TS10** are significantly smaller (−18.5 and −30.9 kcal/mol, respectively).[58]

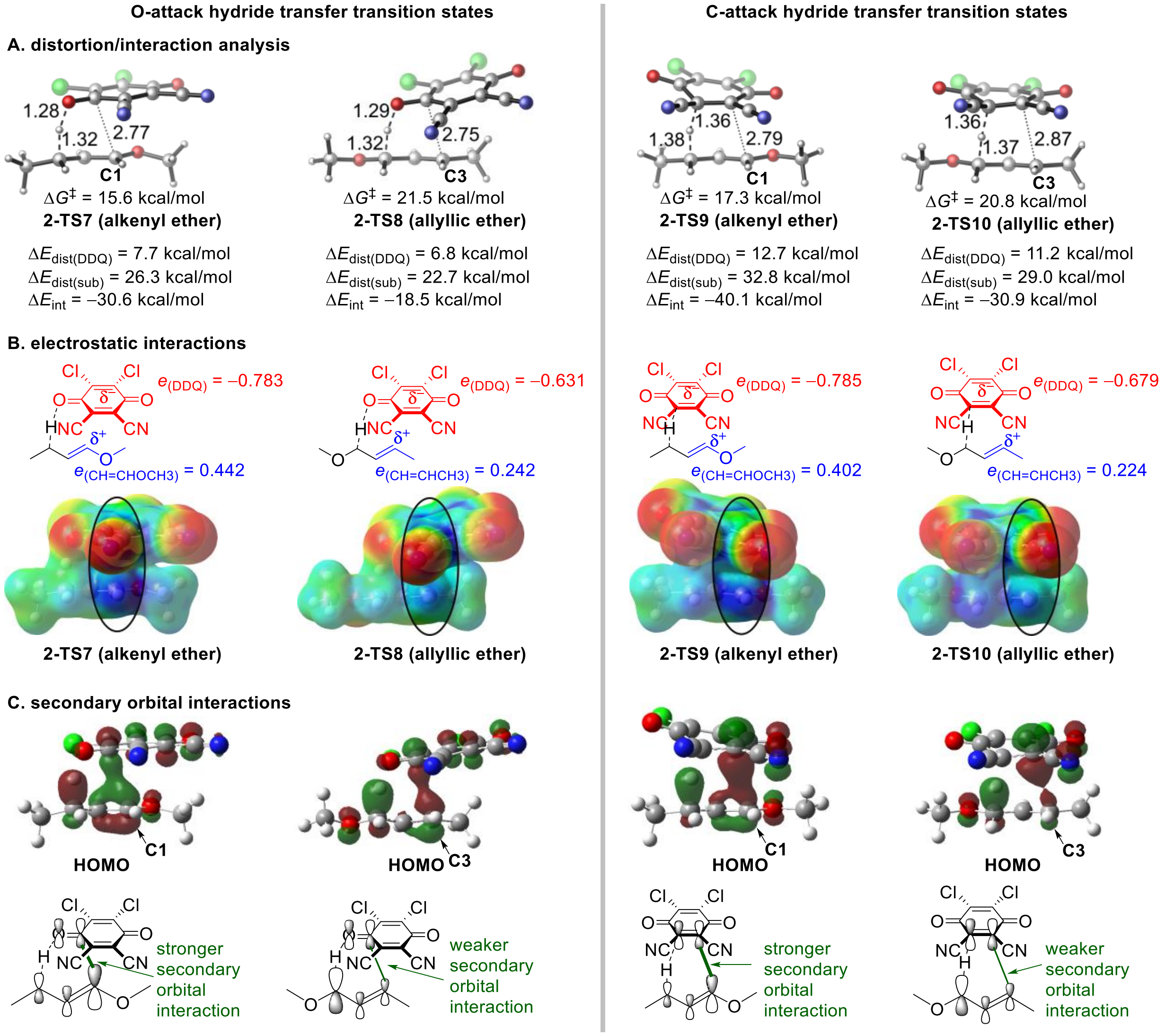

Figure 2-11. Factors that contribute to the greater reactivity of alkenyl ether 2-42 compared to that of allylic ether 2-39. The O- and C-attack hydride transfer transition states with 2-42 are stabilized by greater electrostatic attraction and secondary orbital interactions between the DDQ and the substrate. The HOMO of the transition states were generated using the HF/3-21G level of theory.

The difference in interaction energies with the two different substrates is mostly attributed to the through-space interactions between DDQ and the substrate in the hydride transfer transition state.[59] Significant electron transfer from the substrate to DDQ is observed in all the hydride transfer transition states. The negative charge on DDQ and the positive charge on the substrate lead to strong electrostatic attraction in the transition states. In fact, the quinone ring in DDQ always aligns above the C=C double bond in the substrate to maximize the electrostatic attractions.[60] NPA charge calculations indicate that the DDQ is more negatively charged in **2-TS7** than in **2-TS8** and the double bond moiety in the substrate is more positively charged in **2-TS7** (**Figure 2-11B).** Thus, the greater amount of substrate-to-DDQ electron transfer promotes the electrostatic attraction in **2-TS7**. Similar electrostatic interactions provide greater stabilization to **2-TS9** than **2-TS10**. These electrostatic interactions are visualized in the electrostatic potential (ESP) surfaces of the transition states. The circled and highlighted region on the ESP surfaces indicate the attractive interactions between DDQ (red, indicating negative potential that attracts positive charge) and the double bond in the substrate (blue, indicating positive potential that attracts negative charge). The darker blue in **2-TS7** and **2-TS9** indicates these double bonds are more positively charged and have stronger electrostatic attraction with the DDQ, in agreement with the NPA population analysis.

Examination of the frontier molecular orbitals in the hydride transfer transition states (2-**TS7 - 2-TS10**) revealed moderate secondary orbital interactions between the HOMO of the allylic system and the π* orbital of C=O or C=C bond on the DDQ (**Figure 2-11C**). These secondary donor-acceptor interactions are a result of the relatively short distance between the terminal allylic carbon on the alkenyl and allylic ethers and the carbonyl carbon or the cyano-substituted carbon on the DDQ (*ca.* 2.8 Å). In the reaction with alkenyl ethers (**2-TS7**), the HOMO of the alkenyl ethers is polarized in a way that there is a larger lobe on C1. This allows better secondary orbital interactions between the HOMO of the alkenyl ethers and the π* orbital of the C=O bond on DDQ, as indicated by the large HOMO orbital coefficients on C1 in **2-TS7** (**Figure 2-11C**). In contrast, in the reaction with the allylic ether substrate, the lobe on C3 is smaller, and thus, a weaker secondary orbital interaction is expected with the π* orbital of the C=O bond on DDQ. Similar effects also render slightly more favorable secondary orbital interactions in the C-attack TS with alkenyl ether (**2-TS9**) than with allylic ether (**2-TS10**). In the reaction with benzylic ethers, the secondary orbital interactions with the π* orbital on DDQ are less prominent due to the weaker donor ability of the phenyl π orbital (**Figure 2-12**). Thus, secondary orbital interactions are not expected to affect the reactivity of benzylic ether substrates.

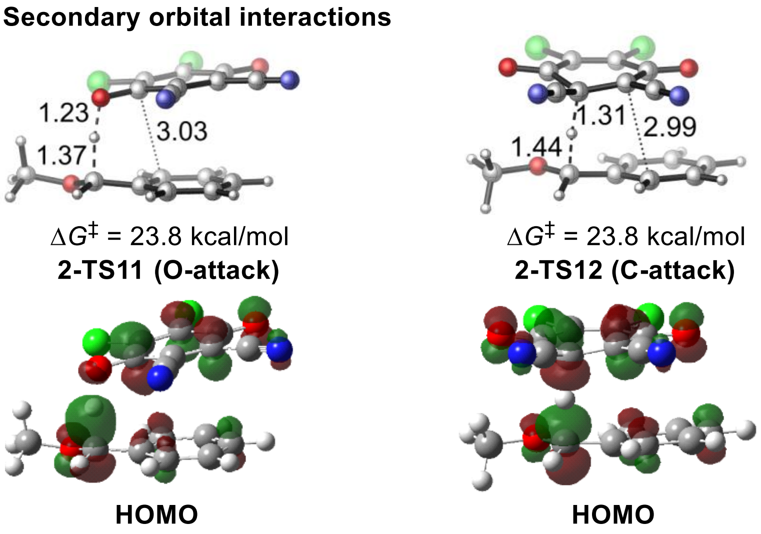

Figure 2-12. Optimized structures of the O- and C-attack transition states in the reaction of benzylic ether 2-49. The HOMO of the two transition states indicate the secondary orbital interactions in these TS are much less prominent than those in the reactions of alkenyl ethers.

2.3.5 Establishing a Predictive Model for Reactivity

The above computational studies revealed two main factors that determine the reactivity of the DDQ-mediated C−H cleavage: the stability of the carbocation intermediate and the extent of electron transfer in the transition state. This creates the possibility for determining whether a mathematical relationship can be established to predict rates based on readily determined molecular properties, in analogy to Sigman's elegant use of multidimensional analytical approaches to gain greater prognosticative capacity for reaction outcomes.[61]

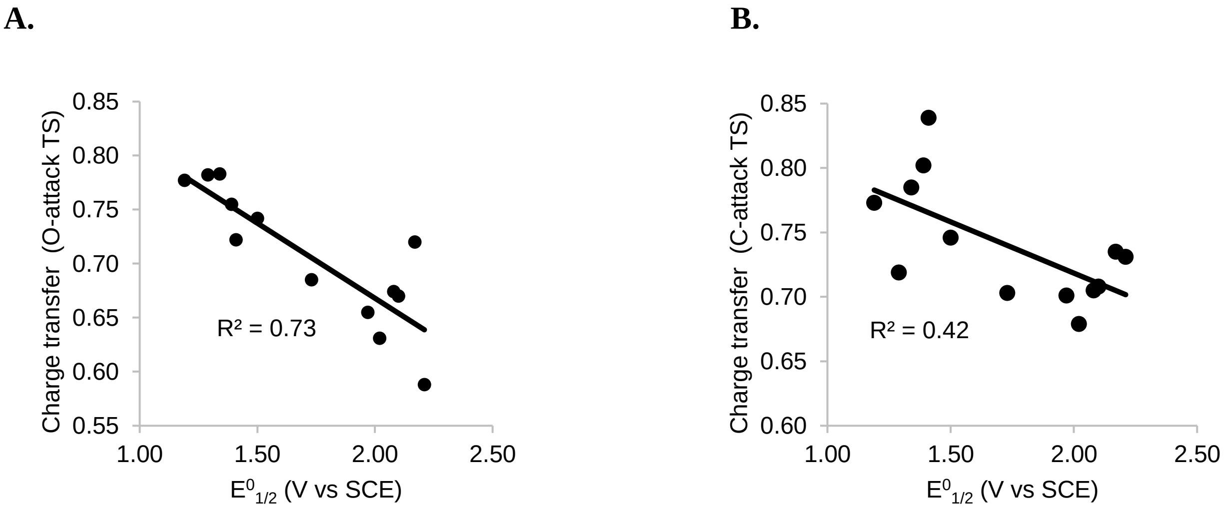

Figure 2-13. Correlation of the charge transfer in the O-attack and C-attack transition state versus the oxidation potential of the substrate (E°1/2).

Here, insights from the DFT studies about the reactivity-determining factors were utilized to rationalize the choice of descriptors for the mathematical model. A moderate correlation between the oxidation potential ($E^0_{1/2}$) of the substrate and the amount of charge transfer in the hydride transfer transition state was observed for the hydride transfer reactions in **Table 2-1** and

Figure 2-8 as shown in **Figure 2-13**. As a result, the extent of electron transfer in the transition state is related to the oxidation potential of the substrate ($E^0_{1/2}$, eq. 1). In addition, as shown in section 2.3.3, the stability of carbocation intermediate is related to the hydride dissociation energy of the corresponding C–H bond in solution (ΔG_{HDE}, eq. 2). Both quantities can be easily computed using DFT,[45,51] and are used as parameters for the mathematical relationship for reactivity of the hydride transfer.[62]

$$\mathrm{RH_{(sol)}} \rightarrow \mathrm{RH^{+\bullet}_{(sol)}} + e^{-} \qquad E^0_{1/2} \qquad (1)$$

$$\mathrm{RH_{(sol)}} \rightarrow \mathrm{R^{+}_{(sol)}} + \mathrm{H^{-}_{(sol)}} \qquad \Delta G_{\mathrm{HDE}} \qquad (2)$$

Using reactions shown in **Table 2-1** and **Figure 2-8** as the training set, a linear free energy relationship (eq. 3) was established to predict $\Delta G^{\ddagger}$ values from the hydride dissociation energies (ΔG_{HDE}, kcal/mol) and the oxidation potentials ($E^0_{1/2}$, V vs SCE) of the substrate. It should be noted that only the barriers of the most favorable hydride transfer pathway (either O- or C-attack) were used to train mathematical relationship.

$$\Delta\, G^{\ddagger}_{\mathrm{predicted}} = 0.485\ \Delta G_{\mathrm{HDE}} + 4.73\ E^0_{1/2} - 27.7 \qquad (3)$$

Comparing the $\Delta G^{\ddagger}$ values predicted from this relationship to the DFT-calculated values (**Figure 2-14**) shows a good correlation for benzylic, allylic, and alkenyl ethers over a wide range of oxidation potentials ($R^2 = 0.784$). The only outlier from this plot is alkenyl ether **2-42**, which has a lower $\Delta G^{\ddagger}$ value than predicted. The outlier indicates that other factors, such as secondary orbital interactions in the case of **2-42**, play a role in determining $\Delta G^{\ddagger}$. The proximity of DDQ and the substrate in the transition states indicates that sterically hindered alkenes and arenes will undergo carbocation formation more slowly than expected, as previously reported.[30c] However, the relationship in eq. 3 proves to be an excellent model for predicting transition state energies in a broad range of reactions and is consistent with experimental observations regarding the importance of oxidation potential and carbocation intermediate stability on reactivity.

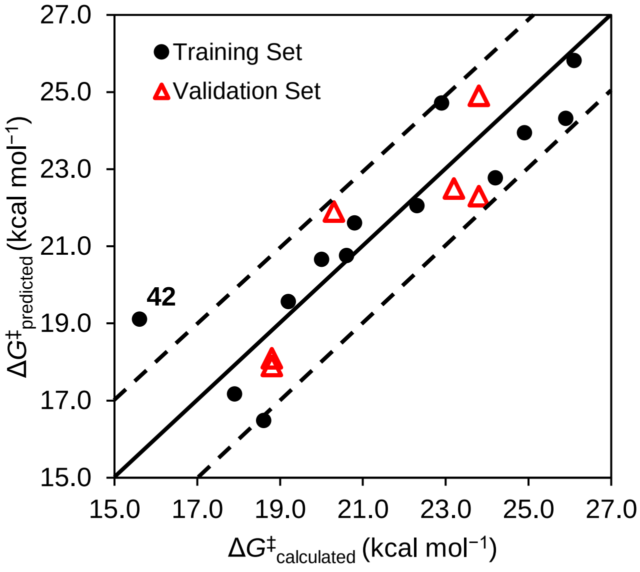

Figure 2-14. Comparison of hydride transfer activation energies from DFT transition state calculations ($\Delta G^{\ddagger}_{\text{calculated}}$) and activation energies predicted from the mathematical relationship using eq. 3 ($\Delta G^{\ddagger}_{\text{predicted}}$). Training set: reactions in Table 2-1 and Figure 2-8. Validation set: reactions in Table 2-2.

With the quantitative reactivity model in hand, it was next applied eq. 3 to a new set of substrates to validate the applicability of this mathematical relationship. It was calculated the hydride dissociation energies and the oxidation potentials of a series of benzylic ether substrates shown in **Table 2-2** and used eq. 3 to derive the predicted Gibbs free energy of activation ($\Delta G^{\ddagger}_{\text{predicted}}$). The predicted $\Delta G^{\ddagger}$ values reliably reproduced the experimental reactivity trend of these substrates.[3a] For example, although *meta*-methoxy substitution slightly destabilizes the carbocation (entries 1 vs 2, 3 vs 4), benzylic ethers **2-50** and **2-52** are still highly reactive in hydride transfer due to their low oxidation potentials. The moderate reactivities of 2-furanyl ether **2-53** and 1-naphthyl ether **2-54** are attributed to their relatively high hydride dissociation energies, although furanyl and naphthyl groups lower the oxidation potentials. Finally, the hydride transfer transition states with **2-49** – **2-54** were calculated using DFT. The DFT-calculated activation energies ($\Delta G^{\ddagger}_{\text{calculated}}$) are in good agreement with the predicted $\Delta G^{\ddagger}$ values using eq. 3 (see “validation set” in **Figure 2-14**). These validation results suggest that the mathematical relationship (eq. 3) can be applied to predict activation energies of a broad range of substrates with an uncertainty less than 2 kcal/mol and to explain the origin of experimentally observed reactivity trend.

Table 2-2. Further validation of the mathematical relationship for reactivity of the DDQ-mediated C−H cleavage.

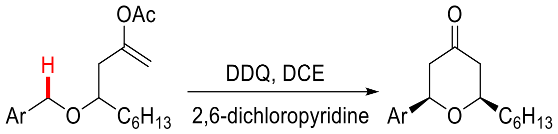

Entry	substrate[a]	$E^{0}_{1/2}$[b]	ΔG_{HDE}[c]	$\Delta G^{‡}_{predicted}$[d]	$\Delta G^{‡}_{calculated}$[e]	T (h)[f]	yield (%)[f]
1	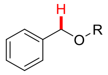 49	2.11	88.0	24.9	23.8	14	63
2	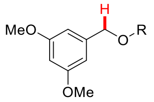 50	1.43	89.2	22.3	23.8	1.5	57
3	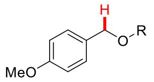 51	1.45	80.2	18.1	18.8	0.75	74
4	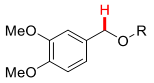 52	1.21	82.2	17.9	18.8	0.1	83
5	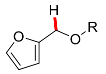 53	1.73	86.6	22.5	23.2	12	63
6	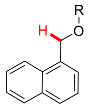 54	1.60	86.6	21.9	20.3	4	84

[a] Methyl ethers (R = Me) were used in the calculations to reduce computational time. [b] Oxidation potential (in V vs SCE) calculated from eq. 1. [c] Hydride dissociation free energy in solution (in kcal/mol) calculated from eq. 2. [d] Predicted $\Delta G^{‡}$ (in kcal/mol) calculated from eq. 3. [e] Activation free energy of hydride transfer (in kcal/mol) from DFT calculations of O- and C-attack transition states. Only the barrier of the most favorable hydride transfer pathway is shown. [f] Experimental reaction time and yield.

The significance of these studies lies in the ability of the dual dependence of cation stability and oxidation potential on the rate of carbon–hydrogen bond cleavage to explain several other observations that we did not directly study. The enhanced rate of enamides and vinyl sulfides relative to allylic amides and sulfides,[3e,f] for example, further illustrates the role of oxidation potential on transition state energy. The disparate reactions of enolsilanes in carbocycles, where nucleophilic addition occurs,[63] and heterocycles, where carbon–hydrogen bond cleavage dominates,[32e,f] illustrates the importance of cation stability on the reaction pathway. The facile oxidation of transiently generated enamines to form α,β-unsaturated iminium ions[30g] demonstrates the role of both factors. The consistency of these results with theory strongly suggests that this simple analysis provides a powerful predictive tool for understanding the rates of DDQ-mediated reactions for a broad substrate scope.

2.4 OXIDATION POTENTIAL CALCULATIONS

The oxidation potentials of the benzylic, allylic, and alkenyl ether substrates ("Sub") were calculated from the reaction Gibbs free energies of the following reduction half-reaction:

$$\text{Sub}^{+\bullet} + e^{-} \rightarrow \text{Sub}$$

For example, to calculate the oxidation potential of **2-16**, the reaction Gibbs free energy of the following reduction half-reactions was calculated using the DFT-computed Gibbs free energies in DCE solution and the Gibbs free energy of electron (−0.867 kcal/mol).[64]

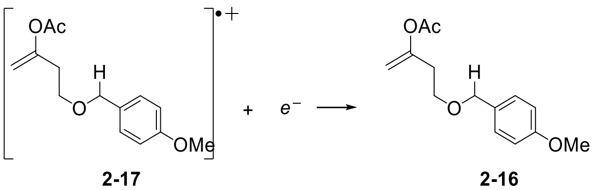

2-17 **2-16**

$\Delta G_{\text{DCE}} = -138.3$ kcal/mol

Since

$$\Delta G = -nFE$$

where n is the number of electrons transferred (one), F is the Faraday constant, the absolute standard reduction potential can be calculated as:

$$E = 6.00\ \text{V}$$

Then, the standard potential referenced to the SCE can be calculated from[65]

$$E^{\ominus,\text{SCE}}_{solvent} = E^{\ominus,\text{abs}}_{solvent} - E^{\text{abs}}_{SCE,aq} + E_L \tag{2}$$

where $E^{\text{abs}}_{SCE,aq}$ is the absolute standard potential for the aqueous saturated calomel electrode (4.522 V) and E_L is the interliquid (intersolvent) potential. Because the experimental value of interliquid potential of DCE is not available, we used the E_L value of ethanol (0.030 V),[66] which has a similar dipole moment as DCE. Thus, the oxidation potential of **2-16** can be calculated as follows:

$$E^{\ominus,\text{SCE}}_{\boldsymbol{16},DCE} = E^{\ominus,\text{abs}}_{\boldsymbol{16},DCE} - 4.522\text{V} + 0.030\ \text{V} = 6.00\ \text{V} - 4.522\ \text{V} + 0.030\text{V} = 1.51\ \text{V}$$

The oxidation potentials of other substrates were also calculated using this approach.

2.5 CONCLUSION

A computational approach to establish a predictive model for reactivity in the DDQ-mediated C−H bond functionalization of a wide variety of benzylic, allylic, and alkenyl ether substrates was employed. The mathematical model is based on insights from a thorough investigation of the mechanisms of the C−H bond cleavage and factors that affect the stability of the hydride transfer transition states. DFT calculations were performed to reveal that the most favorable mechanism of the C−H cleavage is through a concerted hydride transfer from the substrate to DDQ. Two competing pathways, in which the hydride is transferred to the oxygen and the carbon atoms on DDQ, respectively, have comparable activation barriers in reactions with benzylic, allylic, and alkenyl ether substrates, in contrast to previous mechanistic studies of the 1,4-cyclohexadiene dehydrogenation that support the O-attack hydride transfer pathway. These mechanistic studies indicate both the C- and O-attack hydride transfer transition states need to be considered in the reaction barrier calculations.

Using DFT calculations, two key factors that contribute to the reactivity of hydride transfer were identified: (1) the stability of the carbocation intermediate, which could be affected by electronic, steric effects, and ring strain energies, and (2) the electrostatic attraction between DDQ and the substrate in the hydride transfer transition state, which magnitude is affected by the amount of charge transfer in the TS. In addition, secondary orbital interactions between the π orbital of the forming allylic cation and the LUMO of DDQ further stabilize the hydride transfer transition state with alkenyl ether substrates. Based on these mechanistic insights, two parameters that describe the electronic properties of the substrates were chosen to establish a mathematical relationship to quantitatively predict the rate of the C−H cleavage. The hydride dissociation energy in solution

(ΔG_{HDE}) describes the stability of the carbocation and the oxidation potential ($E^0_{1/2}$) of the substrate is a competent parameter to describe the magnitude of charge transfer stabilization in the transition state. This mathematical relationship confirmed that the rate of hydride transfer is sensitive to both factors. This model was applied to efficiently predict activation free energies of the hydride transfer and to explain the experimentally observed reactivity trend of a wide variety of substrates.

3.0 MECHANISTIC STUDIES OF C–H BOND FUNCTIONALIZATION MEDIATED BY HYPERVALENT IODINE REAGENTS

3.1 INTRODUCTION

Functionalization of C–H bonds offers efficient and atom-economical synthetic routes from readily available staring materials. Many approaches have been reported in recent years utilizing this strategy, often with a transitional-metal catalyst.[67] However, the use of metals and the removal of potentially toxic trace metals may incur high costs. In order to avoid the use of metals and develop more economical and environmentally benign reactions, metal-free C–H bond functionalization protocols have been developed.[68] Hypervalent iodine compounds, traditionally used as oxidant in organic chemistry, are a mild yet effective reagents for promoting the activation and functionalization of C–H bonds. Benziodoxolone-based hypervalent iodine reagents have been used for the azidation[69], chlorination[69a], bromination[69a], hydroxylation[70] and formation of new carbon-carbon[71] bonds by means of C–H bond functionalization (**Figure 3-1**). These reagents are very attractive as they combine the high reactivity usually associated with metal reagents with lower toxicity and cost of main-group elements.[72]

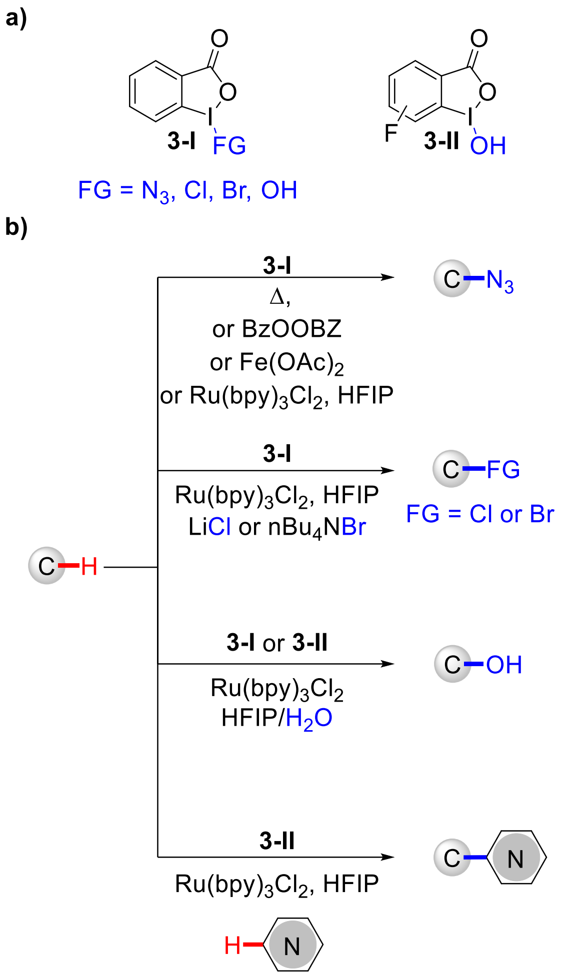

Figure 3-1. Carbon-hydrogen bond functionalization promoted by benziodoxolone-based hypervalent iodine reagents.

Benziodoxolone-based hypervalent iodine mediated 3˚ C–H bond functionalization has been used for a variety of chemical transformations, with selected examples illustrated in **Figure 3-2**. Different reaction conditions have been used to achieve these chemical transformations (**Figure 3-2a**). The use of a ruthenium photoredox catalyst ($Ru(bpy)_3Cl_2$) has been reported for the azidation and hydroxylation reactions with hypervalent iodine reagent[69a] **3-I**. The same conditions have also been employed for the 3˚ C–H bond hydroxylation with perfluoro analogue of hydroxyl hypervalent iodine reagent[71] **3-3**. In addition to the use of photoredox catalyst, thermal conditions have been also reported for the 3° C−H bond azidation reaction using reagent **3-I**[69a]. However, the thermal conditions are only applied to few chemical transformations (**Figure 3-2a**).[69a] The effects of conditions on reactivity is unclear and it needs to be further explored.

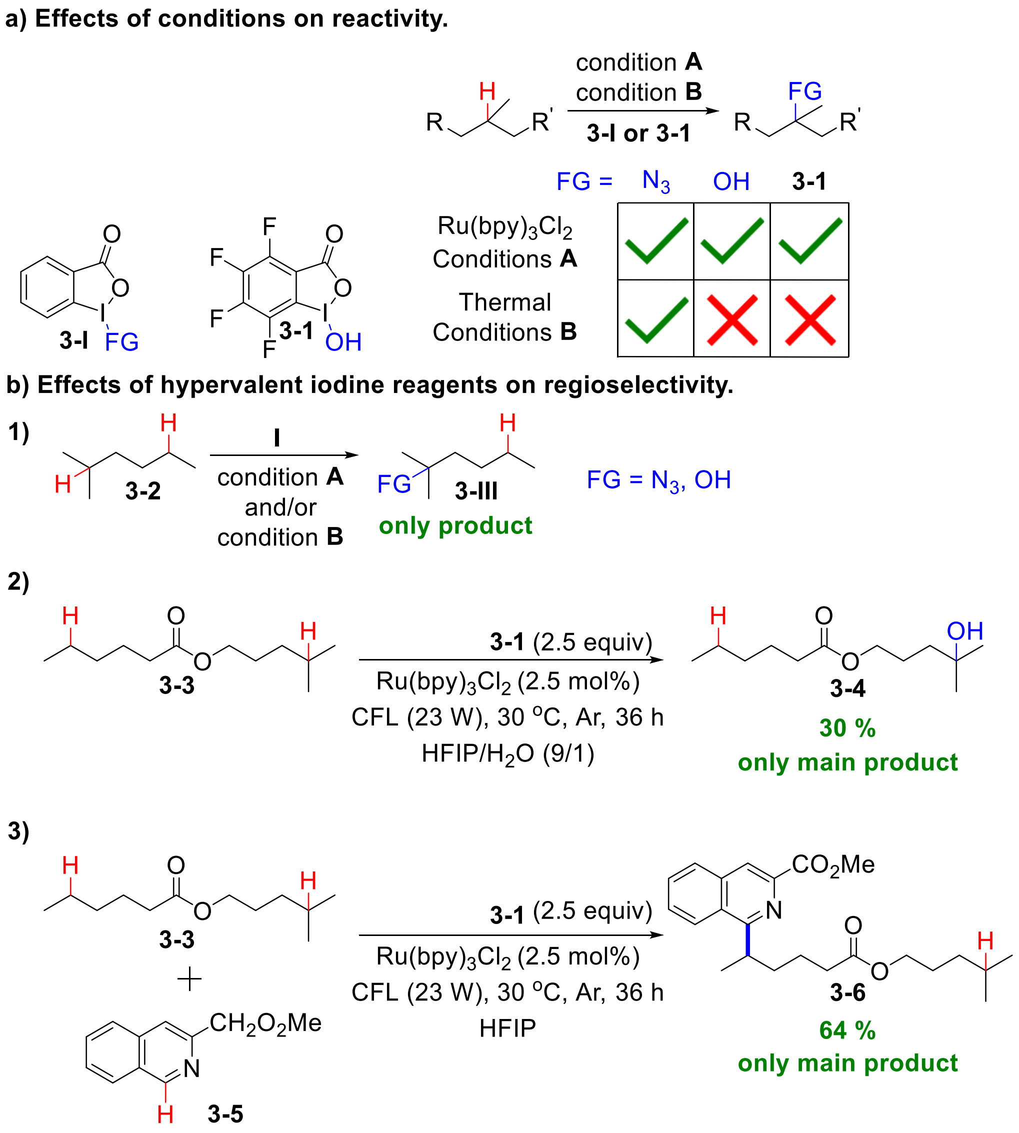

Figure 3-2. Experimental reactivity and regioselectivity of different benziodoxolone-based hypervalent iodine reagents.

Reagents **3-I** (FG = N_3 and OH) demonstrated high regioselectivity towards 3˚ C–H bonds in various functionalization reactions.[69] In contrast, reagent **3-1** is effective in the functionalization of both 3˚ and 2˚ C–H bonds with regioselectivity dependent upon the type of the reaction.[71] (**Figure 3-2b**). For example, hydroxylation of **3-3** using reagent **3-1** only takes place at the tertiary carbon. However, Minisci-type reaction of the same substrate **3-3** and reagent **3-1** selectively yields the 2˚ C–H functionalization product (**Figure 3-2b**). The observed difference between the regioselectivities with reagents **3-I** and **3-1** is unclear and needs to be further explored.

Clearly, a thorough understanding of the mechanisms of benziodoxolone-based hypervalent iodine mediated C–H activation is necessary to elucidate the effects of conditions on reactivity and the effects of reagents **3-I** and **3-1** on regioselectivity. Two different initiation/C–H activation mechanisms have been reported depending on the reaction conditions (thermal or photoredox conditions)[69a, 70, 71] (**Figure 3-3**). It has been proposed that, under thermal conditions, the first step will be the homolytic cleavage of the I-FG bond (**3-I**) generating radical intermediate **3-Ia** or **3-Ib**. The I-centered radical **3-Ia** and O-centered radical **3-Ib** have been proposed in several previous studies[73]. This radical intermediate has been proposed to cleave the C–H bond, generating a carbon centered radical (**R•**).[69a] On the other hand, under photoredox conditions, it has been proposed that the reaction initiates via a single electron transfer (SET) from the ruthenium photoredox catalyst to **3-I** to generate FG- and radical intermediate **3-Ia** or **3-Ib**, followed by the C–H activation step to generate R•.[69a] Another alternative mechanism under this condition is the formation of **3-7** and FG• after the SET, followed by C–H bond activation with the FG•.

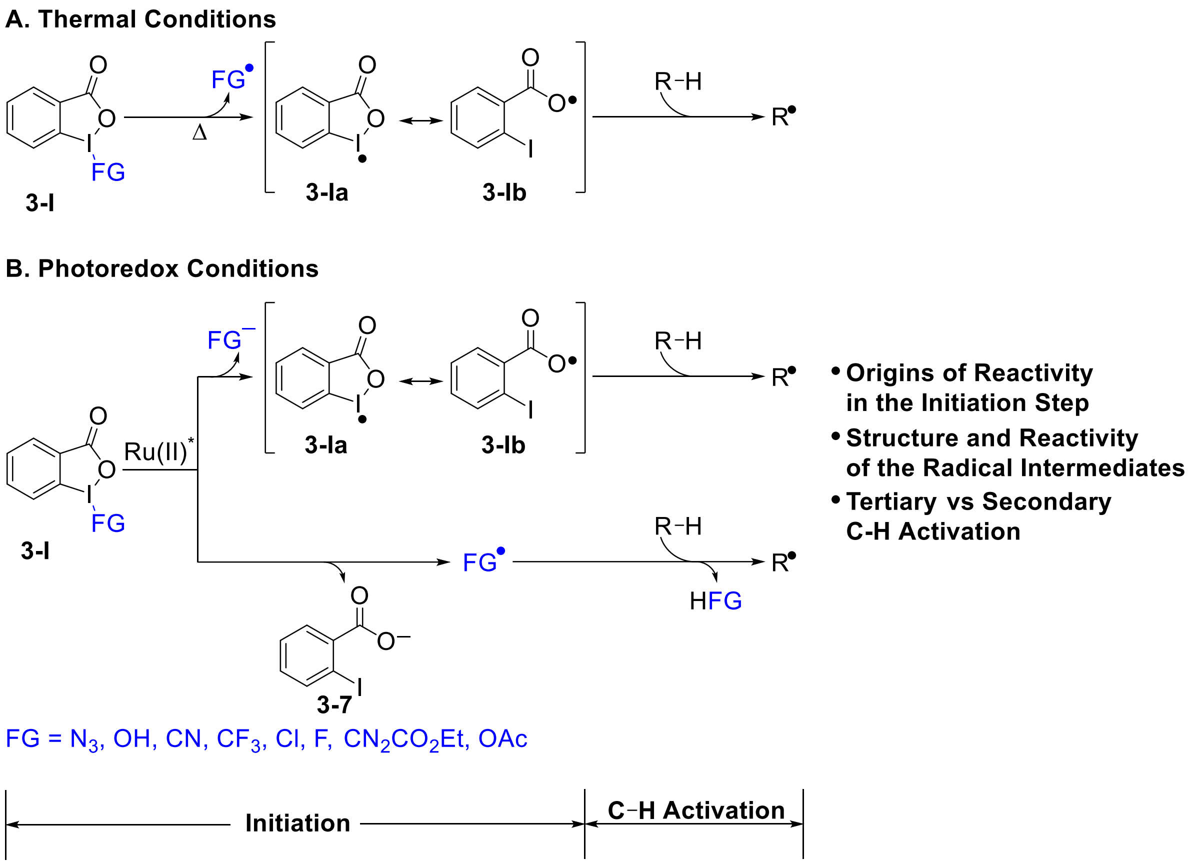

Figure 3-3. Plausible mechanisms for the benziodoxolone-based hypervalent iodine mediated C–H bond activation under thermal and photoredox conditions.

This chapter describes a computational study on the mechanisms of hypervalent iodine mediated C–H bond activation with a wide variety of benziodoxolone reagents. DFT calculations were performed to explore the effects of conditions on reactivity, the structure and reactivity of radical intermediates derived from the hypervalent iodine reagents, and the effects of hypervalent iodine reagents on regioselectivity.

3.2 COMPUTATIONAL DETAILS

All calculations were performed with Gaussian 09.[46] Images of the 3D structures of molecules were generated using CYLView.[47] The geometries of all intermediates and transition states were optimized with the M06-2X[48] functional and the 6-31+G(d) basis set in the gas phase. The SDD pseudopotential basis set was used for iodine atoms. Single point energies were calculated using M06-2X and 6-311++G(d,p) and the SMD[49] solvation model in HFIP and DMSO. Since the solvent parameters for HFIP are not available in Gaussian 09. The parameters of isopropanol were used and the dielectric constant of the solvent was modified to the dielectric constant of HFIP[74] ($\varepsilon = 16.7$) by using the "scrf=(smd,solvent=2-propanol,read)" keywords in the Gaussian 09 calculations. The reported Gibbs free energies and enthalpies include zero-point vibrational energies and thermal corrections computed at 298 K. The Gibbs free energies were corrected using the Truhlar quasi-harmonic approximation from GoodVibes.[75]

The geometry of the key reaction intermediate, the radical **3-Ia/3-Ib**, was optimized using a few different levels of theories to evaluate the effects of density functional, basis set, and solvation models on the weak intramolecular I···O interaction. The optimized I···O distance is highly dependent upon the choice of density functional and basis set (**Table 3-1**). As expected, calculations without diffuse functions significantly overestimate the I···O distance (entries 1 and 4). B3LYP and ωB97X-D also predict longer I···O distance than M06-2X when using the same basis set (entries 1, 9 versus 5). Interestingly, calculations using the 6-31+G(d) and 6-311++G(d,p) basis sets give almost identical results (entries 2 versus 3, 5 versus 6). Replacing the SDD basis set with the LANL2DZ basis set for iodine leads to slight decrease of the I···O distance (entries 7 and 8).

Finally, using solvation model in the geometry optimization also noticeably decreases the I···O distance (**Table 3-1**). Based on these test calculations, M06-2X/6-31+G(d)-SDD level of theory was selected for geometry optimization in the computational studies in this chapter.

Table 3-1. Geometry of 3-Ic optimized at different levels of theories.

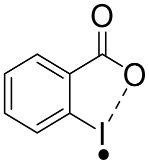

3-Ic

entry	**method for geometry optimization**	***d*(I−O) / Å**
1	B3LYP/6-31G(d)-SDD	2.81
2	B3LYP/6-31+G(d)-SDD	2.71
3	B3LYP/6-311++G(d,p)-SDD	2.71
4	M06-2X/6-31G(d)-SDD	2.78
5	M06-2X/6-31+G(d)-SDD	2.59
6	M06-2X/6-311++G(d,p)-SDD	2.59
7	M06-2X/6-31+G(d)-LANL2DZ	2.56
8	M06-2X/6-311++G(d,p)-LANL2DZ	2.56
9	*ω*B97X-D/6-31+G(d)-SDD	2.68
10	M06-2X/6-31G(d)-SDD/SMD(HFIP)	2.50
11	M06-2X/6-31+G(d)-SDD/SMD(HFIP)	2.47
12	M06-2X/6-311++G(d,p)-SDD/SMD(HFIP)	2.48

3.3 RESULTS AND DISCUSSION

3.3.1 Initiation Reactivity Under Thermal and Photoredox Conditions

As shown in **Figure 3-2**, both thermal and ruthenium photoredox-catalyzed conditions have been used to cleave the BI–FG bond to generate radical intermediate **3-Ia**, **3-Ib** or FG•. In order to explore the reactivity of the initiation process under different conditions, the initiation reaction pathways under thermal and photochemical conditions were calculated using density functional theory (DFT).

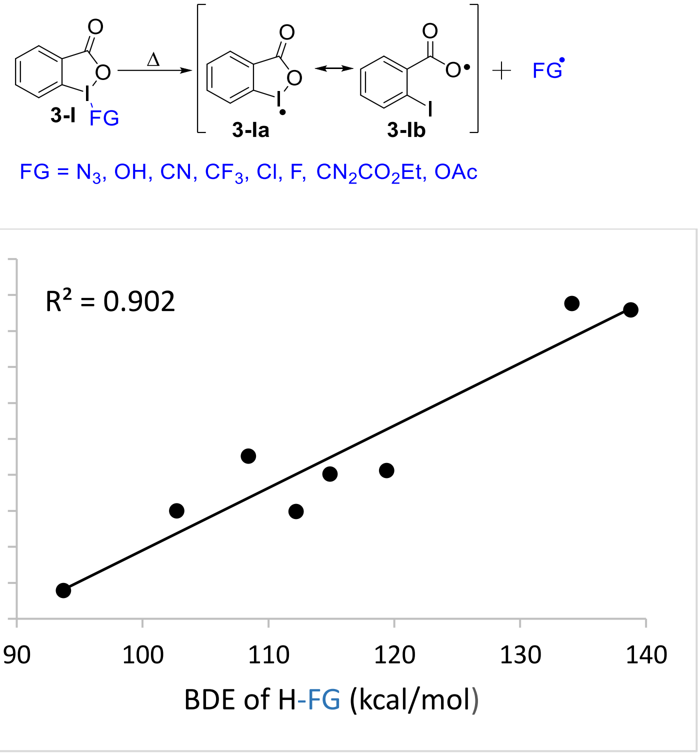

Figure 3-4. Correlation plot of BDEs of BI-FG and H-FG under thermal conditions.

Bond dissociation enthalpies (BDE) of BI–FG bonds in **3-I** containing different functional groups were calculated to study the initiation reactivities of different hypervalent iodine reagents under thermal conditions. A good correlation between the BDEs of BI–FG and H–FG was obtained (R^2 = 0.902) (**Figure 3-4**). This indicates that the initiation under thermal conditions is promoted by the thermodynamic stability of FG•. This observation agrees with Xue's [76] computational study, which also showed the reactivity of **3-I** under thermal conditions correlates with the stability of FG•.

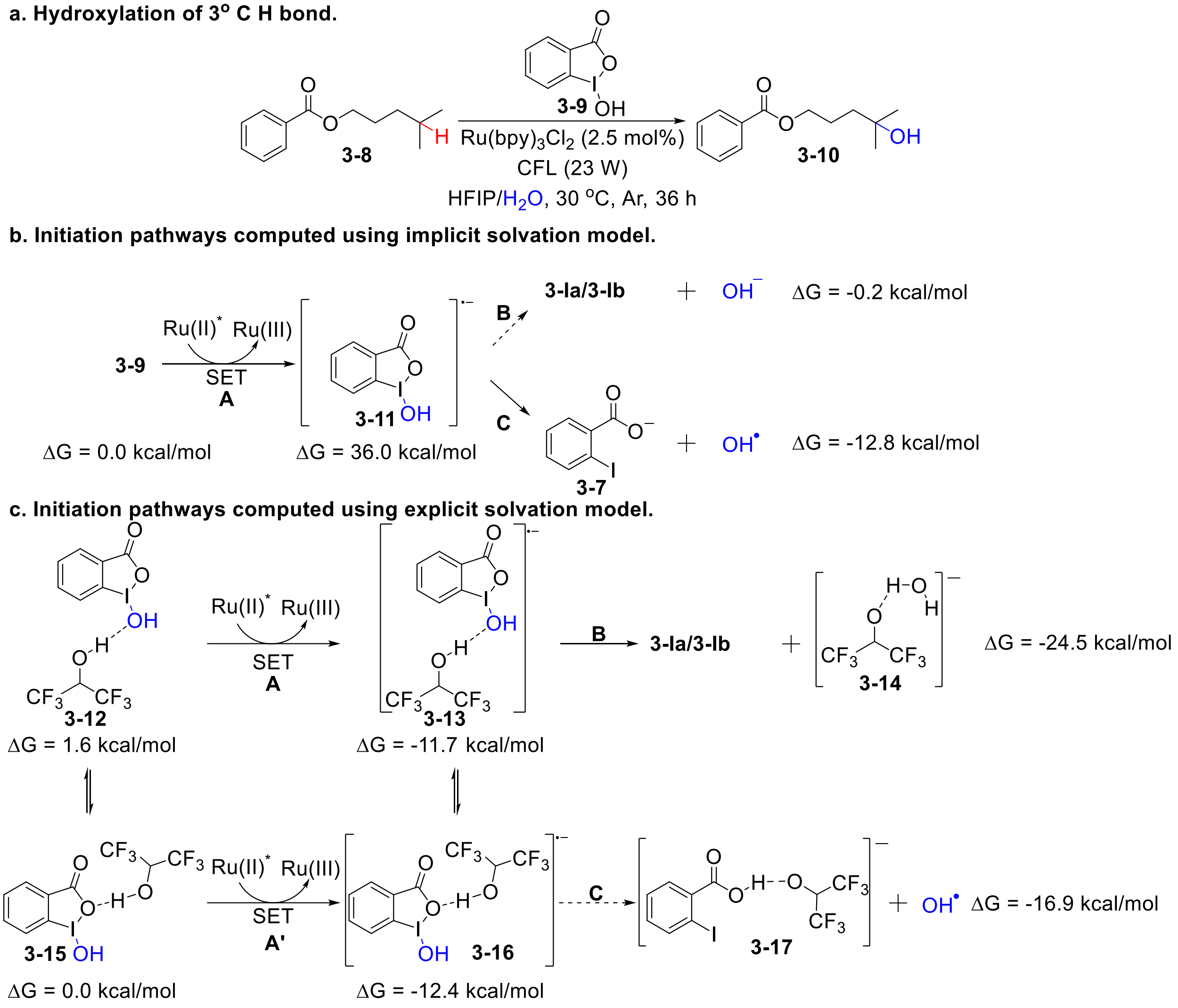
a. Hydroxylation of 3° C H bond.

b. Initiation pathways computed using implicit solvation model.

c. Initiation pathways computed using explicit solvation model.

Figure 3-5. Computed single electron transfer pathways in the photoredox-mediated initiation with 3-9 with implicit and explicit solvation models. All energies are with respect to the reactants (3-9 and 3-15, respectively).

The initiation pathways using the ruthenium photoredox-catalyst were next explored. Hypervalent iodine reagent **3-9** has been used in the hydroxylation of 3˚ C–H bonds as shown in **Figure 3-5a**. DFT calculations were carried out to explore the most favorable initiation pathways using reagent **3-9**. First, calculations were performed with the SMD implicit solvation model, which is the standard approach used in most computational studies of organic reaction systems (**Figure 3-5b**). These implicit solvation calculations showed that the reduction of **3-9** by photo-excited Ru(II)* via single electron transfer (SET) to form radical anion intermediate **3-11** is highly endergonic (ΔG = 36.0 kcal/mol). It was observed computationally that the formation of OH$^\bullet$ through pathway **C** is considerably more favorable thermodynamically (ΔG = -12.8 kcal/mol) than the formation of radical intermediate **3-Ia** or **3-Ib** through pathway **B** (ΔG = -0.2 kcal/mol). Therefore, the calculations with implicit solvents suggest that the OH$^\bullet$ is responsible for the C–H cleavage in the C–H activation step.

Because strong explicit solvent interactions are expected with the hexafluoroisopropanol (HFIP) solvent, DFT calculations were performed with explicit solvent molecules to investigate the initiation pathways described above. In these calculations, an HFIP molecule was used to form hydrogen bonding interaction with the hypervalent iodine reagent and the radical and anionic intermediates formed after the initiation step (**Figure 3-5c**). The SMD solvation model was also employed to describe the long-range electrostatic interactions with the polar solvent. These calculations with explicit HFIP coordination show that the SET from Ru(II)* to **3-15** to form radical anion intermediate **3-13** is exergonic (ΔG = -11.7 kcal/mol). In addition, the dissociation of **3-13** now favors the formation of radical intermediate **3-Ia** or **3-Ib** and a hydroxide anion (ΔG = -24.5 kcal/mol) than the formation of OH$^\bullet$ (ΔG = -16.9 kcal/mol). These results suggest that polar protic solvents promote the formation of radical intermediate **3-Ia** or **3-Ib** in the photoredox-mediated initiation process. Because HFIP stabilizes the hydroxide anion through hydrogen bond interactions, it is important to consider such explicit solvent interactions computationally.

Table 3-2. Computed Gibbs free reaction energies of the single electron transfer from the photo-excited Ru(II)* to 3-18 using HFIP explicit solvent.

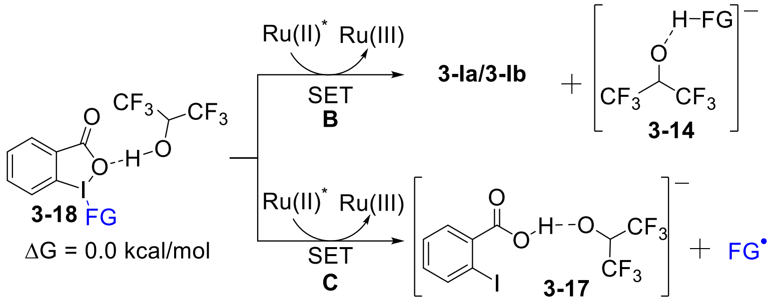

FG	ΔG_b	ΔG_c
CN	-24.0	3.7
Cl	-39.2	-17.6
OAc	-32.4	-16.3
F	-37.6	4.5
OH	-24.5	-16.9
N_3	-27.4	-37.5
CF_3	-17.8	-25.4
CN_2CO_2Et	-6.2	-14.4

Knowing that HFIP plays an important role in the initiation reaction, the explicit solvation model was used to calculate the reaction energies of SET between the photo-excited Ru(II)* and a variety of benziodoxolone-based hypervalent iodine reagents (**Table 3-2**). Reactions with benziodoxolone-based hypervalent iodine reagents containing CN, Cl, OAc, F and OH functional groups favor the formation of radical intermediate **3-Ia** or **3-Ib**. In contrast, reactions with hypervalent iodine reagents containing N_3, CF_3 and CN_2CO_2Et functional groups favor the formation of $N_3^\bullet$, $CF_3^\bullet$, and $CN_2CO_2Et^\bullet$. The generation of $CF_3^\bullet$ and $CN_2CO_2Et^\bullet$ intermediates has been proposed in several previous experimental studies, including the visible light photoredox-catalytic trifluoromethylation and C–H functionalization of *N*-aryl acrylamides (in the case CF_3-bearing benziodoxolone)[77] and the photoredox-catalysis of C–H diazomethylation of arenes with CN_2CO_2Et-bearing benziodoxolone.[78]. The N_3-bearing benziodoxolone has been proposed to form

$N_3^{\bullet}$ after the SET under photo-redox conditions.[79] In addition, $N_3^{\bullet}$ was shown to be more reactive for C–H activation than radical intermediate **3-Ia** or **3-Ib** (for more detail explanation refer to section 3.3.3).

Table 3-3. Computed Gibbs free reaction energies of the single electron transfer from the photo-excited Ru(II)* to 3-I using DMSO implicit solvent.

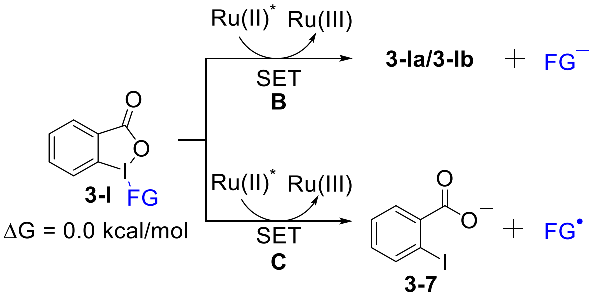

FG	ΔG_B	ΔG_C
CN	-21.1	13.3
Cl	-35.7	-12.0
OAc	-18.8	-15.2
F	-20.4	15.7
OH	10.2	-11.8
N_3	-24.2	-26.0
CF_3	19.5	-16.6
CN_2CO_2Et	1.8	-12.2

So far, explicit solvation model calculations with HFIP have shown that the I–FG cleavage under photoredox conditions generally prefer the formation of radical intermediate **3-Ia** or **3-Ib** except for N_3, CF_3 and CN_2CO_2Et-bearing benziodoxolone reagents. In order to further explore the solvation effects during the initiation step under photo-redox conditions, SET reaction energies between the photo-excited Ru(II)* and the same type benziodoxolone-based hypervalent iodine reagents were calculated using dimethyl sulfoxide (DMSO) a polar aprotic solvent (**Table 3-3**).

Because the aprotic DMSO solvent is incapable of forming hydrogen-bonding interactions with the hypervalent iodine reagents and the radical intermediate **3-Ia** or **3-Ib**. No explicit DMSO solvent molecule was used in these calculations. The implicit SMD solvation model was used instead. These calculations shown that the SET reaction energies for the formation of radical intermediate **3-Ia** or **3-Ib** (pathway B) and $FG^•$ (pathway C) are less thermodynamically favorable using aprotic solvent (DMSO) than using protic solvent (HFIP) (**Table 3-2** and **3-3)**. Similar results were observed as in the case of HFIP regarding the thermodynamically preference for the formation of radical intermediate **3-Ia** or **3-Ib** over $FG^•$ after the SET. For benziodoxolone-based hypervalent iodine reagents containing CN, Cl, OAc, and F functional groups, calculations shown that will favor the formation of radical intermediate **3-Ia** or **3-Ib**. While for benziodoxolone-based hypervalent iodine reagents containing N_3, CF_3 and CN_2CO_2Et will promote the formation of $N_3^•$, $CF_3^•$ and $CN_2CO_2Et^•$. However, in the case of reagent **3-9**, calculations shown that formation of $OH^•$ is more thermodynamically favorable than the formation of radical intermediate **3-Ia** or **3-Ib** after the SET step when using DMSO. This is in contrast with the results obtained by explicit solvation effect using HFIP that suggested the formation of radical intermediate **3-Ia** or **3-Ib**. All together, these results suggest that the solvent plays an important role in the initiation reaction of **3-9** under photo-redox conditions. Radical intermediate **3-Ia**/**3-Ib** or $OH^•$ is formed preferentially when a protic solvent (HFIP) or an aprotic solvent (DMSO) was used, respectively.

3.3.2 Structure of the Hypervalent Iodine Radical Intermediate

After exploring the reactivity in the initiation step under the different conditions, a thorough investigation on the structure of radical intermediate **3-Ia** or **3-Ib** was performed. Both the I-centered radical (**3-Ia**) and O-centered radical (**3-Ib**) have been proposed in previous experimental studies (**Figure 3-6a**).

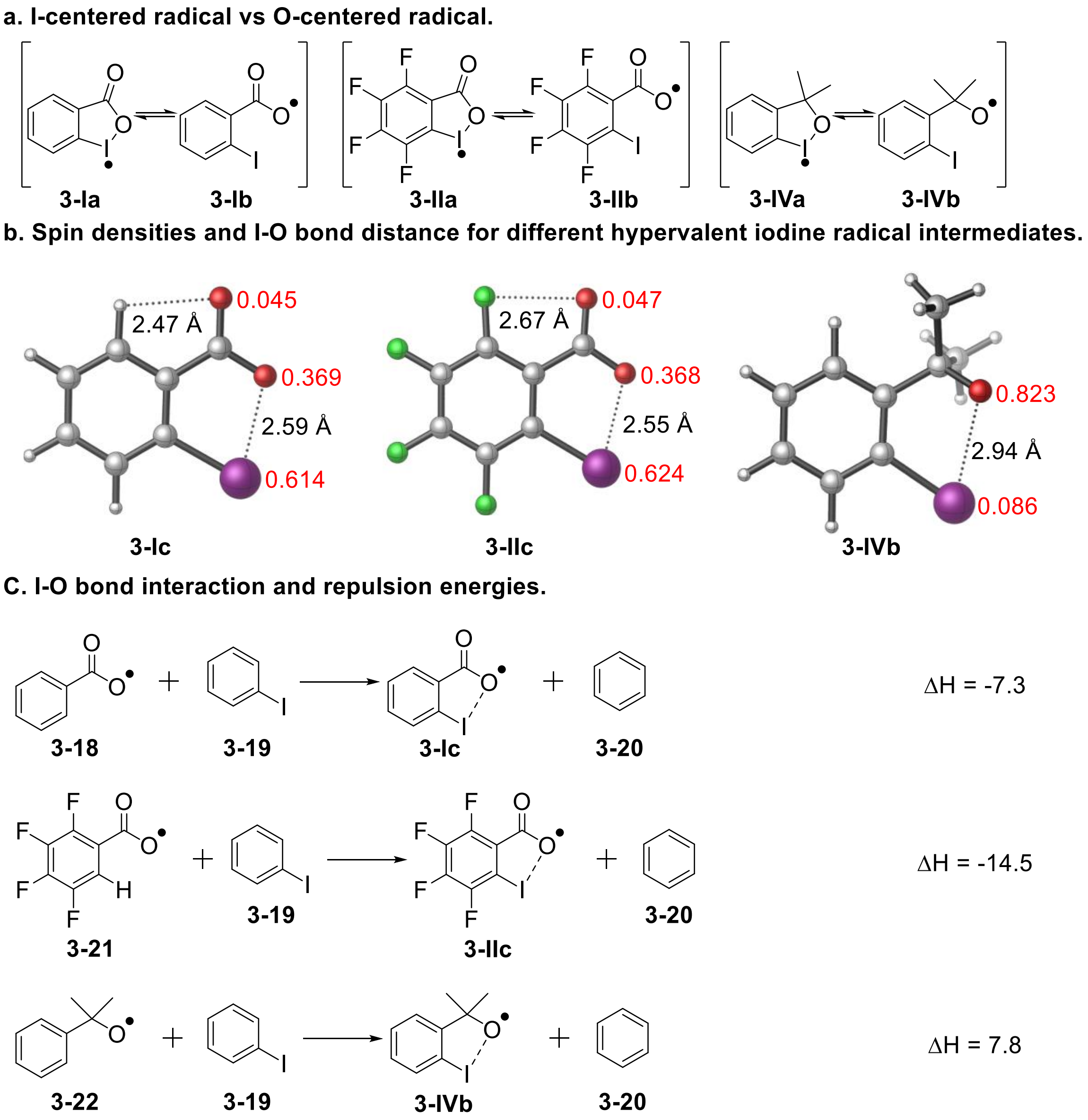

Figure 3-6. Spin densities and I–O bond interaction and repulsion energies.

DFT calculations were performed to optimize the geometries of several radical intermediates derived from different benziodoxolone-based hypervalent iodine reagents (**Figure 3-6**). Although a pair of interconvertible radical species, I-centered radical (**3-Ia**) and O-centered radical (**3-Ib**), have been proposed in previous studies,[73] calculations show that **3-Ia** and **3-Ib** are indeed resonance structures of the same compound. The postulated cyclic structure of **3-Ia** with a relatively short I-O bond of *ca.* 2.1-2.2 Å cannot be located by the DFT calculations. Instead the radical intermediate (see **3-Ic** in **Figure 3-6b**) is stabilized by the secondary interactions between I and O atoms with a longer distance than a typical I-O σ-bond (**Figure 3-6b**). The spin density of **3-Ic** is delocalized to the I and O atoms. The same analysis was performed to the proposed radical intermediates **3-IIa/3-IIb**. As in the case of radical intermediate **3-Ic**, a single structure **3-IIc** was located with spin density delocalized to the I and O atoms (**3-IIc**). The I–O bond distance in **3-IIc** also suggests some favorable interaction between the I and O atoms (**Figure 3-6b**).

Next, a different type of hypervalent iodine radical intermediate (**3-IVa** or **3-IVb**) derived from benziodoxole was studied (**Figure 3-6b**). Again, only a single structure of the intermediate (**3-IVb**) can be located. However, in contrast to the two radical intermediates discussed above, the spin density of radical intermediate **3-IVb** is mostly located on the oxygen atom, suggesting this intermediate can be better described by the O-centered radical and resonance structure **3-IVa** does not contribute. In addition, no stabilizing interaction was observed between the I and O atoms as evidenced by the longer distance between these two atoms compared to those in radical intermediates **3-Ic** and **3-IIc**.

To investigate the magnitude of stabilizing I-O interactions in **3-Ic** and **3-IIc**, the intramolecular iodine-oxygen interaction energies were calculated from the reaction energies of the isodesmic reactions depicted in **Figure 3-6c**. Calculations show that the iodine-oxygen interaction energies in **3-Ic** and **3-IIc** are is -7.3 and -14.5 kcal/mol, respectively, indicating stabilizing interactions between the I and O atoms. In contrast, a repulsive interaction of +7.8

kcal/mol was found in **3-IVb**, which indicates the I-O interactions in this radical intermediate are mostly steric repulsions between the *ortho* substituents (**Figure 3-6c**).

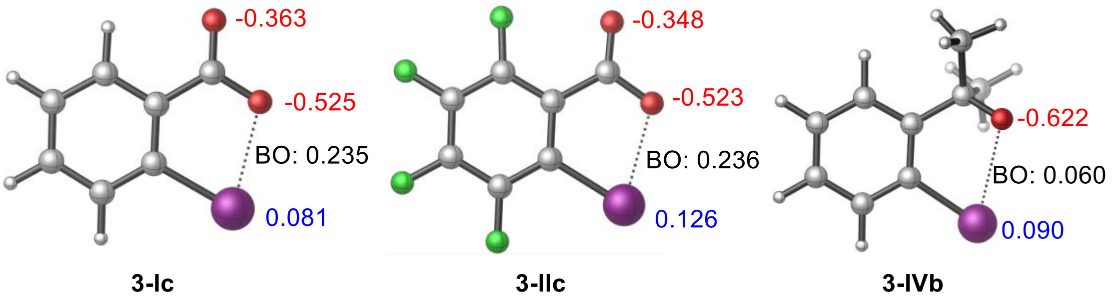

Figure 3-7. Natural population analysis charges and iodine-oxygen bond order (BO) of 3-Ic, 3-IIc, and 3-IVb.

The nature of the stabilizing interactions between the I and O atoms in **3-Ic** and **3-IIc** was next investigated. Natural population analysis (NPA) atomic charges were calculated to investigate whether electrostatic attractions contribute to the stabilizing interactions (**Figure 3-7**). In all the cases calculated, **3-Ic**, **3-IIc** and **3-IVb**, the oxygen atoms are substantially negatively charged while the iodine atoms are only slightly positively charged. These results suggest electrostatic attractions may contribute to the stabilizing iodine-oxygen interaction, but only to a very small degree. Natural bond orbital (NBO) calculations was next performed to determine the Wiberg bond indices, *i.e.* bond orders (BO), between the iodine-oxygen atoms. Calculations show that the iodine-oxygen bond orders in **3-Ic** and **3-IIc** are 0.235 and 0.236, indicating a secondary bonding interaction that is considerably weaker than a typical σ bond. In contrast, in the case of **3-IVb**, the I-O BO is only 0.060, which suggests a much weaker bonding interaction, in agreement with the intramolecular I-O interaction energy calculations in **Figure 3-6**.

3.3.3 Reactivity and Regioselectivity of Hypervalent Iodine Radical Intermediate in C–H Bond Activation

Although the radical characters of intermediates **3-Ic** and **3-IIc** are delocalized to both O and I atoms, the C–H bond abstraction with these intermediates always involves the oxygen atom, rather than the iodine. The transition state energies of the tertiary and secondary C–H bond activation by **3-Ic** were calculated using isobutane and propane as model substrates (**Figure 3-8**). Two transition state isomers, namely *E* and *Z* conformations, were identified for the tertiary and secondary C–H bonds activation steps. In *E*-conformers, the forming O–H bond is *anti*-periplanar with respect to the carbonyl (C=O). While in Z-conformers, the forming O–H bond is *syn*-periplanar to the carbonyl (C=O). In both tertiary and secondary C–H abstraction, the *E* conformers (**3-*E*-TS1** and **3-*E*-TS3**) are more energetically favorable than the corresponding *Z*-conformers. This is somewhat surprising considering only the *Z*-conformer could be stabilized by the LP(O)→σ*(C=O) hyperconjugation. It is surmised this conformational preference for *E* conformers may be due to favorable C–H π interactions between the forming alkyl radical and the benzene ring in the *E* conformer that are not present in the *Z* conformer of the transition states. When comparing the activation energies of the C–H bond cleavage with the tertiary and secondary C–H bonds, a lower energy barrier was obtained for the tertiary C–H bond activation (18.9 kcal/mol, **3-*E*-TS1**). These results suggest that radical intermediate **3-Ic** is more reactive towards tertiary C–H bonds than secondary C–H bonds. This agrees with the high levels of regioselectivity for tertiary C–H bonds[69a] in the C–H azidation mediated by reagent **3-I** (**Figure 3-2b**).

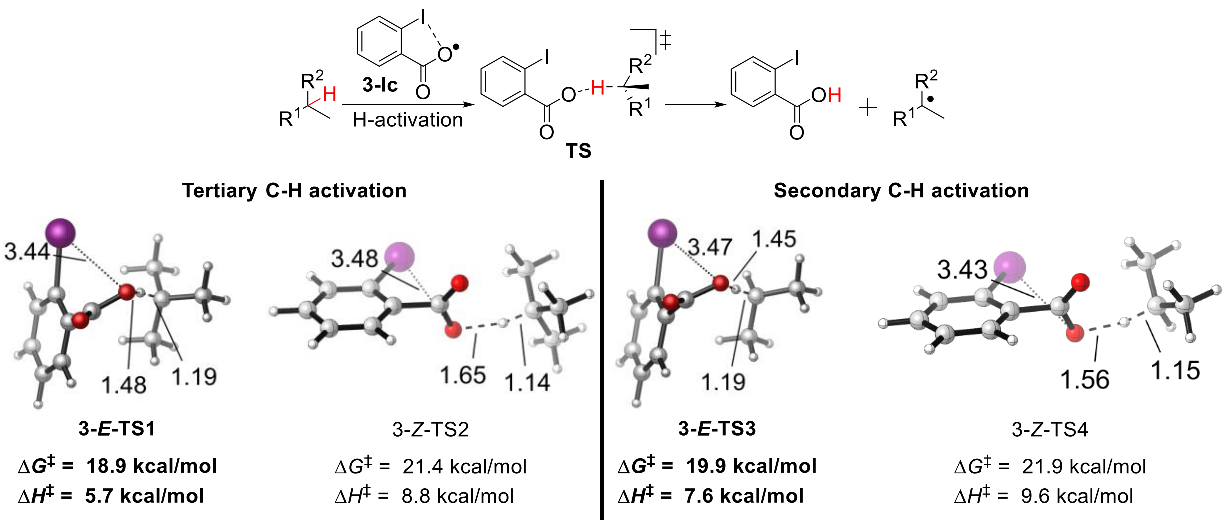

Figure 3-8. Tertiary and secondary C–H bond activation transition state energies mediated by 3-Ic using isobutane and propane as model substrates.

Next, the transition state energies of the C–H bond activation with the perfluorinated radical intermediate **3-IIc** were calculated (**Figure 3-9**). *E* and *Z* conformations of the transition states were again identified for the tertiary and secondary C–H activation. Similar to the reaction with **3-Ic**, the *E* conformation of the C–H abstraction transition state is the most favorable with transition state energies of 16.4 and 16.6 kcal/mol for tertiary and secondary C–H abstractions, respectively. These barriers are lower than those with radical **3-Ic**. These results suggest that **3-IIc** is more reactive than **3-Ic** in the C–H abstraction (**Figures 3-8** and **3-9**). Furthermore, they also suggest that the C-H abstraction with **3-IIc** is less regioselective than with **3-Ic**. These results agree with the experimental observation from Chen research group that suggest that perfluoro analogue of benziodoxolone can be used to activate both tertiary and secondary C–H bonds[71] (**Figure 3-2b**).

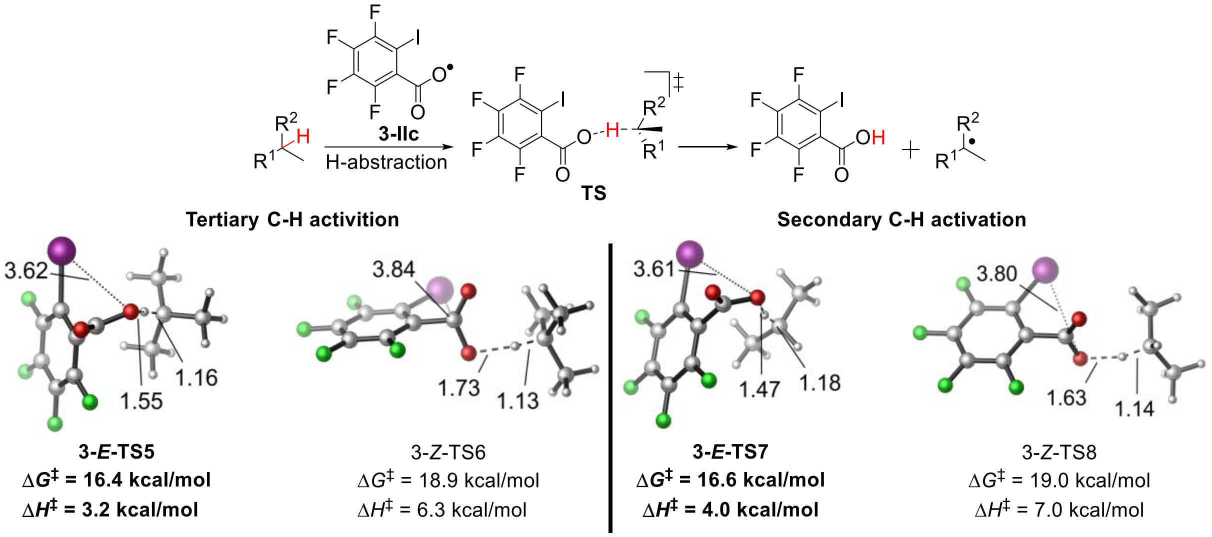

Figure 3-9. Tertiary and secondary C–H bond activation transition states energies mediated by 3-IIc using isobutane and propane as model substrates.

So far, calculations have shown that radical intermediate **3-IIc** is more reactive but less regioselective than radical intermediate **3-Ic** (**Figure 3-9** and **Figure 3-8**). The difference in regioselectivity can be attributed to how late or early the transition state of the C–H bond activation is. Based on the C–H bond distances in **3-*E*-TS5** (*C--H*, 1.16 Å) and. **3-*E*-TS1** (*C--H*, 1.19 Å), **3-*E*-TS5** is an earlier transition state that **3-*E*-TS1**. Similarly, the C–H bond distances in the secondary C-H abstraction transition states **3-*E*-TS3** (*C--H*, 1.19 Å) and **3-*E*-TS7** (*C--H*, 1.18 Å) also indicate **3-*E*-TS7** is slightly earlier that **3-*E*-TS3**. This observation is consistent with the Hammond's postulate – the more reactive radical **3-IIc** involves earlier C–H abstraction transition state, and therefore, reacts with lower regioselectivity.

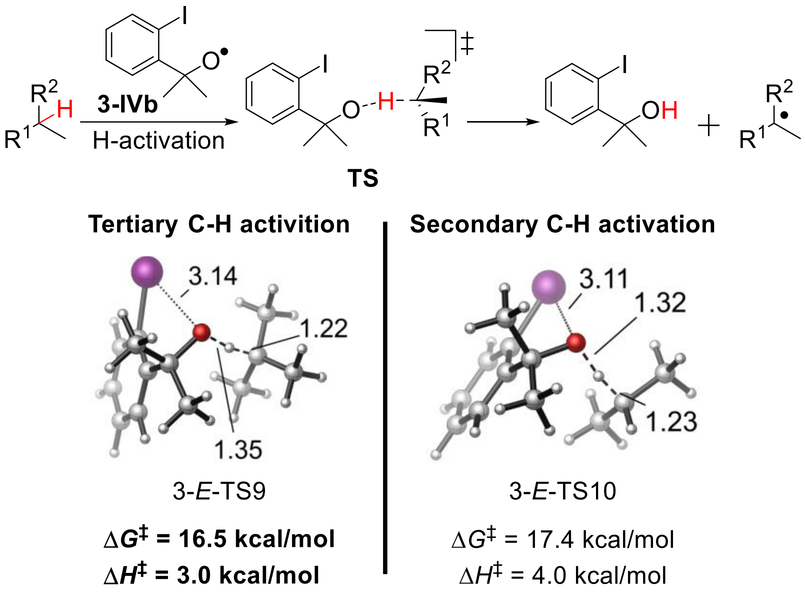

Figure 3-10. Tertiary and secondary C–H bond activation transition states energies mediated by 3-IVb using isobutane and propane as model substrates.

The transition state energies for the C–H bonds activation of tertiary and secondary C–H bonds by **3-IVb** were next calculated using isobutane and propane as model substrates (**Figure 3-10**). Calculations shown that the activation transition state energy for tertiary C–H bond was 16.5 kcal/mol (**3-TS9**), while for secondary C–H bond was 17.4 kcal/mol (**3-TS10**), meaning that the activation of tertiary C–H bond by **3-IVb** is more energetically favorable than the secondary C–H activation. Comparing the activation energies with the three different radical intermediates, **3-IIc** and **3-IVb** are more reactive than **3-Ic** (**Figure 3-8**, **Figure 3-9** and **Figure 3-10**). Calculations also shown that **3-IVb** is more regioselective than **3-IIc**. This can be also attributed to the earliness of the C–H abstraction transition state. Based on the C–H bond distances, **3-*E*-TS9** (*C--H*, 1.22 Å) is a later transition state than **3-*E*-TS5** (*C--H*, 1.16 Å) and **3-*E*-TS10** (*C--H*, 1.23 Å) is later than **3-*E*-TS7** (*C--H*, 1.18 Å). Thus, the higher regioselectivity of radical intermediate **3-IVb** can be attributed to a later transition state during the tertiary and secondary C–H bond activation compared to the transition states with radical **3-IIc** (**Figure 3-9** and **Figure 3-10**).

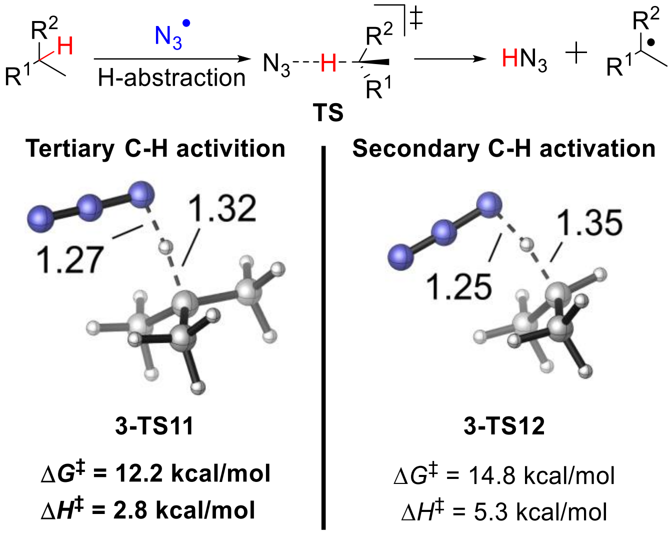

Figure 3-11. Tertiary and secondary C–H bond activation transition state energies mediated by $N_3^\bullet$ using isobutane and propane as model substrates.

The transition state energies for the tertiary and secondary C–H bond activation with the azide radical (**N_3•**) were next explored using isobutane and propane as the model substrates (**Figure 3-11**). The activation Gibbs free energy for the tertiary C–H bond activation is 12.2 kcal/mol (**3-TS11**), while for secondary C–H bond is 14.8 kcal/mol (**3-TS12**). These results suggest that the activation of tertiary C–H bond by **N_3•** is more energetically favorable than secondary C–H bond. Comparison of these results with the computed activation energies with radical intermediates **3-Ic**, **3-IIc** and **3-IVb** indicates that **N_3•** is a more reactive radical (**Figure 3-8**, **Figure 3-9**, **Figure 3-10** and **Figure 3-11**), while still more regioselective towards tertiary C–H bonds than **3-IIc**. This is in agreement with the regioselective functionalization of tertiary

C−H bonds involving the **N$_3$•** radical. Interestingly, the optimized geometries of **3-TS11** (*C--H*, 1.32 Å) and **3-*E*-TS12** (*C--H*, 1.35 Å) indicate the **N$_3$•** C−H abstraction occurs via relatively late transition states, which positively contribute to the regioselectivity for tertiary C−H bond abstraction (**Figure 3-9** and **Figure 3-11)**. It should be noted that the relatively small size of **N$_3$•** compared to radicals **3-Ic**, **3-IIc** and **3-IVb** suggests the reaction with **N$_3$•** is the least sensitive to the steric effects of the tertiary C−H bonds.

3.4 CONCLUSION

Density functional theory (DFT) calculations were performed to study the mechanisms of the C−H bond activation mediated by benziodoxolone-based hypervalent iodine reagents. The reactivities of different hypervalent iodine reagents under thermal and photoredox conditions, the structure and reactivity of the radical intermediates derived from the hypervalent iodine reagents, and their effects on regioselectivity were investigated.

The reactivities of different hypervalent iodine reagents in the initiation step under thermal and photoredox conditions were studied. Under thermal conditions, the initiation reactivity correlates with the stability of FG$^\bullet$. Under photoredox conditions, the initiation occurs via a SET process that transfers an electron from the photoexcited photoredox catalyst to the hypervalent iodine. Explicit solvent coordination between protic solvents and the anionic species generated after the SET with the photoredox catalyst may play an important role on the reaction mechanisms and reactivities of the initiation step. In protic solvents, such as HFIP, the SET process forms an *ortho*-iodobenzoate radical from benziodoxolone-based hypervalent iodine reagents containing CN, Cl, OAc, F, and OH functional groups. However, for benziodoxolone-based hypervalent iodine reagents containing N_3, CF_3 and CN_2CO_2Et functional groups, the SET process favors the formation of $N_3^\bullet$, $CF_3^\bullet$, and $CN_2CO_2Et^\bullet$ radicals and *ortho*-iodobenzoate anion. The SET with the OH-bearing benziodoxolone is sensitive towards solvation effects. Calculation suggest that HFIP (protic solvent) promotes the formation of *ortho*-iodobenzoate radical while DMSO (aprotic solvent) promotes the formation of the hydroxyl radical ($OH^\bullet$).

Structures and properties of radical intermediates **3-Ic**, **3-IIc** and **3-IVb** were elucidated by calculating the spin density, the intramolecular I–O interaction energies, and the I–O bond order (BO). Spin density in radical intermediates **3-Ic** and **3-IIc** is delocalized to the I and O atoms. In radical intermediate **3-IVb**, the spin density is mostly located on the O atom. In radical intermediates **3-Ic** and **3-IIc** the I–O distance is shorter in comparison to radical intermediate **3-IVb**. This suggests some favorable I–O interactions in **3-Ic** and **3-IIc**. Bond order calculations suggest that the favorable I–O interactions in **3-Ic** and **3-IIc** are due to secondary bonding interactions.

The reactivity and regioselectivity of radical intermediates **3-Ic**, **3-IIc**, **3-IVb**, and $N_3^\bullet$ in tertiary and secondary C–H bond activations were explored by calculating the transition state energy barriers. Calculations showed that radical intermediate 3-IIc is more reactive than 3-Ic and 3-IVb. However, $N_3^\bullet$ is the most reactive radical as showed by calculations. The perfluorinated radical **3-IIc** has low regioselectivity between tertiary and secondary C–H bond activation. The low regioselectivity of **3-IIc** is associated with an early transition state with relatively short C–H distances. In contrast, C–H abstraction reactions with radicals **3-Ic**, **3-IVb**, and $N_3^\bullet$ have later transition states and are more regioselective towards tertiary C–H bonds than secondary C–H bonds.

4.0 COMPUTATIONAL STUDIES OF C–H HYDROXYLATION, EPIMERIZATION OF TERTIARY CARBON CENTERS, AND C–H ALKYLATION OF *N*-HETEROARENES USING HYPERVALENT IODINE REAGENTS

Reproduced in part with permission from Yaxin Wang, Xiafei Hu, Cristian A. Morales-Rivera, Guo-Xing Li, Xin Huang, Gang He, Peng Liu, and Gong Chen. "Epimerization of tertiary Carbon Centers via Reversible Radical Cleavage of Unactivated C(sp^3)–H Bonds" *J. Am. Chem. Soc.*, **2018**, *140,* 9678-9684. Copyright 2018, American Chemical Society. In this work, I designed and carried out DFT calculations and analysis of computational results. The experimental studies were performed by the Chen research group.

A significant part of this chapter was published as Guo-Xing Li, Cristian A. Morales-Rivera, Yaxin Wang, Fang Gao, Gang He, Peng Liu, and Gong Chen. " Photoredox-Mediated Minisci C–H Alkylation of *N*-Heteroarenes Using Boronic Acids and Hypervalent Iodine" *Chem. Sci.* **2016**, *7,* 6407-6412; Guo-Xing Li, Cristian A. Morales-Rivera, Fang Gao, Yaxin Wang, Gang He, Peng Liu, and Gong Chen. "A Unified Photoredox-Catalysis Strategy for C(sp^3)–H Hydroxylation and Amidation Using Hypervalent Iodine" *Chem. Sci.,* **2017**, *8*, 7180-7185. In this work, I designed and carried out DFT calculations and analysis of computational results. The experimental studies were performed by the Chen research group.

4.1 INTRODUCTION

In Chapter 3, it was discussed how radical intermediates are generated under thermal and photoredox conditions with hypervalent iodine reagents. In addition, calculations were performed to explore the structure of these radical intermediates and their reactivity towards tertiary and secondary C−H bond activation. The purpose of this chapter is to further explore the role of hypervalent iodine reagents in several specific examples of C−H bond functionalization reactions. Calculations were performed to explore their role during the photoredox-mediated Minisci-type C−H alkylation of *N*-heteroarenes and C(sp^3)−H hydroxylation. In addition, calculations were performed to explore the role of hypervalent iodine reagents in the epimerization of tertiary carbon centers.

N-heteroarenes are one of the most widely used structural motifs in molecular science, and are routinely found in natural products, drug molecules, organic materials, and ligands for transition metal catalysts.[80] Synthetic methods which enable the selective functionalization of the C−H bonds of *N*-heteroarenes could greatly facilitate their applications in these areas.[81] C−H alkylation could provide more regiochemically diverse modifications.[82] Recently, the C−H functionalization of electron-deficient heteroarenes via addition of carbon-centered radicals under oxidative conditions, known as the Minisci reaction, has undergone a remarkable renaissance, offering increasingly powerful methods for synthesizing alkyl-substituted heteroarenes.[83] However, despite these significant advances, practical and broadly applicable methods for Minisci C−H alkylation of *N*-heteroarenes that are able to couple complex alkyl groups are still lacking. In 2016, the Chen[84] research group reported the first photoredox-mediated Minisci C−H alkylation reaction of *N*-heteroarenes with a variety of easily accessible primary and secondary alkyl boronic acids (**Figure 4-1**). Its high efficiency, broad substrate scope, excellent functional group tolerance, and mild operation conditions make it particularly suitable for late-stage functionalization of complex substrates such as drug molecules.

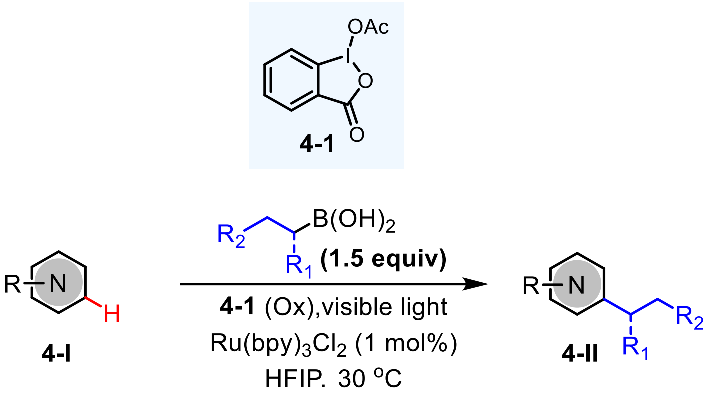

Figure 4-1. Photoredox-mediated Minisci C−H alkylation with alkyl boronic acids.

Although alkyl boron reagents are readily available and well-known precursors for alkyl radicals, they have been rarely used in photoredox-mediated C−C coupling reactions.[85, 86, 87, 88]. In 2015, Chen reported a decarboxylative alkenylation of alkyl trifluoroborates with vinyl carboxylic acids using a hypervalent iodine oxidant, acetoxybenziodoxolone (**4-1**), under Ru photoredox catalysis.[89] Recently, in the investigation performed by Chen on radical-mediated C(sp^3)−H azidation reactions, they discovered that azidobenziodoxolone can be readily activated by visible light in the presence of [Ru(bpy)$_3$]Cl$_2$, initiating a radical chain reaction.[69a] Intrigued by the unique radical reactivity of benziodoxolone reagents under visible light irradiation, they questioned whether they can facilitate Minisci C−H alkylation. Section 4.2.1 of this chapter describes a computational study of the mechanism of the Minisci alkylation with alkyl boronic acids and **4-1**. DFT calculations were performed to explore the reaction mechanisms and the role of the photoredox catalyst and the hypervalent iodine reagent in promoting the formation of the alkyl radical intermediates under the mild reaction conditions.

Methods for efficient and selective alkyl C−H oxidation could streamline the synthesis of fine chemicals, natural products, and drug metabolites.[90,91] Despite rapid advances in the development of transition metal-catalyzed reactions and metal-free reagents, synthetically useful C(sp^3)−H oxidation chemistry is still in great demand.[92, 93] In this aspect, in 2017, Chen[94] reported an efficient and broadly applicable photoredox-catalysis strategy for the selective hydroxylation of tertiary and benzylic C−H bonds using hydroxyl benziodoxolone as oxidant and H_2O as cosolvent and hydroxylation reagent (**Figure 4-2**). Section 4.2.2 of this chapter describes a computational study of the mechanism of the photoredox C(sp^3)−H hydroxylation using **4-2** and **4-4**. DFT calculations were performed to explore the role of the photoredox catalyst and the hypervalent iodine reagent. In particular, calculations were performed to explore the reactivity difference between **4-2** and **4-4** in the C−H oxygenation reaction.

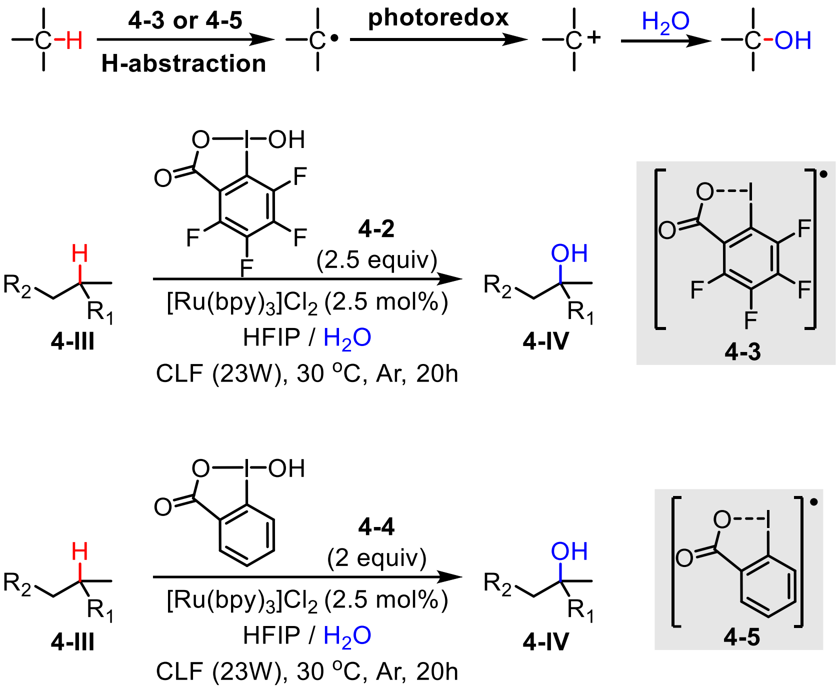

Figure 4-2. C(sp^3)−H oxygenation with hypervlent iodine.

As previously discussed, selective functionalization of alkyl C−H bonds have been greatly advanced over the past few decades, offering streamlined strategies for the synthesis and modification of complex molecules. A wide range of reactions have been developed to transform C(sp^3)−H bonds into different functional groups. However, reactions featuring reversible cleavage of unactivated C(sp^3)−H bonds have received much less attention. Racemization or epimerization via reversible cleavage of C(sp^3)−H bonds could offer an invaluable tool for editing the stereochemistry of organic compounds. In 2018, Chen[95] reported an efficient and synthetically useful protocol for epimerizing tertiary carbons via radical cleavage of nonacidic 3° C(sp^3)−H bonds with hypervalent iodine reagent benziodoxolone azide and H_2O under mild conditions (**Figure 4-3**). Section 4.2.3 of this chapter describes a computational study on the epimerization of tertiary carbon centers via reversible radical cleavage of unactivated C(sp3)−H bonds. DFT calculations were performed to explore the role of the hypervalent iodine reagent during the reaction. In specific, calculations were performed to explore the reactivity of $N_3^{\bullet}$ and **4-5** in the C−H activation step and the H donor ability of HN_3 on the epimerization of 3° C−H bonds of cyclic alkanes.

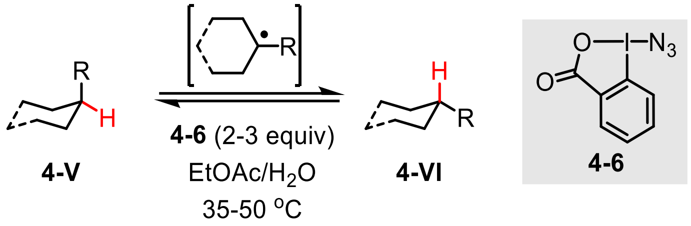

Figure 4-3. Epimerization of nonacidic 3° C−H bonds of cyclic alkanes.

4.2 RESULTS AND DISCUSSION

4.2.1 Photoredox-Mediated Minisci C–H Alkylation of *N*-Heteroarenes Using Alkyl Boronic Acids and Hypervalent Iodine Reagent

4.2.1.1 Computational details

All DFT calculations were performed with the Gaussian 09 software package.[46] Geometries were optimized using the M06-2X[48] functional and the 6-31+G(d) basis set in the gas phase. The SDD pseudopotential basis set was used for iodine atoms. Single point energies were calculated using M06-2X and 6-311++G(d,p) and the SMD[49] solvation model in HFIP. Since the solvent parameters for HFIP are not available in Gaussian 09 the parameters of isopropanol were used and the dielectric constant of the solvent was modified to the dielectric constant of HFIP[96] ($\varepsilon = 16.7$) by using the "scrf=(smd,solvent=2-propanol,read)" keywords in the Gaussian 09 calculations. The reported Gibbs free energies and enthalpies include zero-point vibrational energies and thermal corrections computed at 298 K. All reported Gibbs free energies and enthalpies are corrected to the standard concentration in solution (1 mol/L).

4.2.1.2 The reaction energy of the one electron reduction of 4-1 using the excited state Ru(II)*(bpy)$_3^{2+}$

The following procedures were taken to calculate the single electron transfer reaction from the photoredox catalyst to **4-1** (**Figure 4-4**).

The photoexcited [Ru(II)(bpy)$_3^{2+}$]* is a potent reductant with an experimental standard reduction potential (SRP) of −0.81 V vs. SCE in MeCN.[97] Thus, the absolute SRP in MeCN can be calculated as follows[98]

$$E^{\ominus,\mathrm{abs}}_{\mathrm{Ru(bpy)}_3^{3+/2+*}} = E^{\ominus,\mathrm{SCE}}_{\mathrm{Ru(bpy)}_3^{3+/2+*}} + 4.429\mathrm{V} = -0.81\mathrm{V} + 4.429\mathrm{V} = 3.62\mathrm{V}$$

Since

$$\Delta G = -nFE$$

where n is the number of electrons transferred (one), F is the Faraday constant, the Gibbs free energy of the following reduction half reaction is

$$\mathrm{Ru(bpy)}_3^{3+} + e^- \rightarrow \mathrm{Ru^*(bpy)}_3^{2+} \qquad \Delta G_{\mathrm{MeCN}} = -83.5\ \mathrm{kcal/mol} \qquad (1)$$

The reaction Gibbs free energies of the following reduction half reactions are calculated using the DFT-computed Gibbs free energy in HFIP solution and the Gibbs free energy of electron (−0.867 kcal/mol).[99]

$$\mathbf{4\text{-}1} + e^{-} \rightarrow \mathbf{4\text{-}11} \qquad \Delta G_{\mathrm{HFIP}} = -102.2\ \mathrm{kcal/mol} \tag{2}$$

$$\mathbf{4\text{-}1} + e^{-} \rightarrow \mathbf{4\text{-}5} + \mathbf{4\text{-}12} \qquad \Delta G_{\mathrm{HFIP}} = -107.7\ \mathrm{kcal/mol} \tag{3}$$

$$\mathbf{4\text{-}1} + e^{-} \rightarrow \mathbf{4\text{-}13} + \mathbf{4\text{-}14} \qquad \Delta G_{\mathrm{HFIP}} = -99.9\ \mathrm{kcal/mol} \tag{4}$$

The reaction energies of the SET reactions (eq. 5-7) can be calculated from equations 1-4. Since the experimental reduction potential of $\mathrm{Ru(bpy)}_3^{3+}/\mathrm{Ru^*(bpy)}_3^{2+}$ in HFIP is not available, the reduction half-reaction energy in MeCN (eq. 1) was used in the calculations.

$$\mathrm{Ru^*(bpy)}_3^{2+} + \mathbf{4\text{-}1} \rightarrow \mathrm{Ru(bpy)}_3^{3+} + \mathbf{4\text{-}11} \qquad \Delta G_{\mathrm{HFIP}} = -18.7\ \mathrm{kcal/mol} \tag{5}$$

$$\mathrm{Ru^*(bpy)}_3^{2+} + \mathbf{4\text{-}1} \rightarrow \mathrm{Ru(bpy)}_3^{3+} + \mathbf{4\text{-}5} + \mathbf{4\text{-}12} \qquad \Delta G_{\mathrm{HFIP}} = -24.2\ \mathrm{kcal/mol} \tag{6}$$

$$\mathrm{Ru^*(bpy)}_3^{2+} + \mathbf{4\text{-}1} \rightarrow \mathrm{Ru(bpy)}_3^{3+} + \mathbf{4\text{-}13} + \mathbf{4\text{-}1} \qquad \Delta G_{\mathrm{HFIP}} = -16.4\ \mathrm{kcal/mol} \tag{7}$$

4.2.1.3 Computational study on the mechanism of the photoredox-mediated Minisci C−H alkylation

Control experiments (performed by Chen research group) and density functional theory (DFT) calculations have been carried out to probe the mechanism the photoredox-mediated Minisci alkylation with alkyl boronic acids and **4-1**. As shown in **Figure 4-4**, Chen observed that reaction of **4-7** with $BuB(OH)_2$ and benzoyl peroxide **4-8** in HFIP under visible light irradiation without photocatalyst also gave the alkylated product **4-9** in 20% yield along with 11% yield of arylated side product **4-10**, which is presumably formed from **4-16** via the decarboxylation of **4-15.** In comparison with $BuB(OH)_2$, $BuBF_3K$ showed much lower reactivity. Furthermore, **4-19** was formed as the only C−H functionalized product in 38% yield when *ortho*-iodobenzoyl peroxide **4-11** (highly explosive) was used as the oxidant for reaction of **1** with $BuB(OH)_2$ under the same conditions. These experiments suggest that benzoyloxy radicals can react with alkyl boronic acids to generate the requisite alkyl radical for the subsequent C−H alkylation.

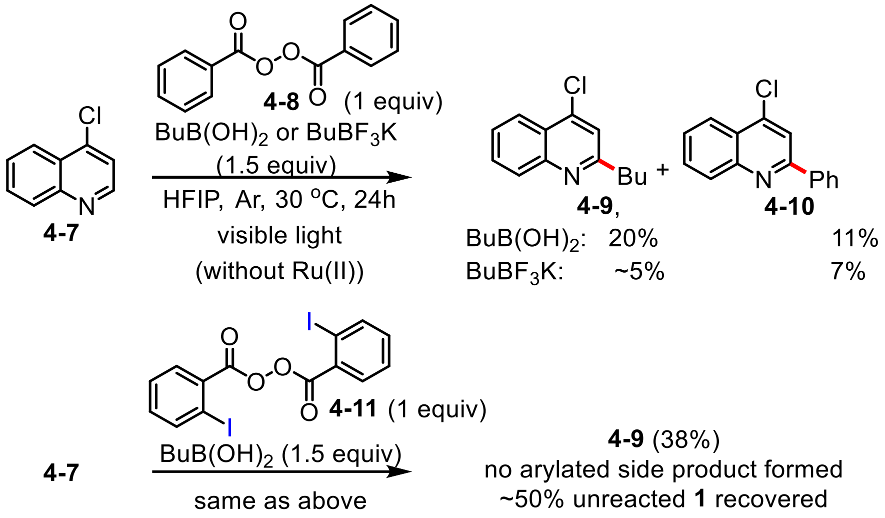

Figure 4-4. Experimental mechanistic studies performed by the Chen group.[84]

As shown in **Figure 4-5**, DFT calculations showed that oxidant **4-1** can be readily reduced by photoexcited Ru(II)* via single electron transfer (SET) to form a radical anion intermediate **4-11**, which then can undergo I−O bond cleavage to form radical **4-5** and acetate anion **4-12** via pathway *a* or form **4-13** and acetoxyl radical **4-14** via pathway *b*. Formation of **4-5** is considerably more thermodynamically favorable than formation of **4-14**. Although an implicit solvation model was used here, the predicted preferred reaction pathway (pathway *a*) is consistent with the calculations using explicit solvation model described in Chapter 3. Calculations also revealed that **4-5** is notably more stable than benzoyloxy radical **4-15** and is much less prone to undergo decarboxylation to form the corresponding aryl radical, which could cause the C−H arylation side reaction (**Figure 4-5b**). For detail explanation of the stability of **4-5** referred to chapter 3 section 3.3.2.

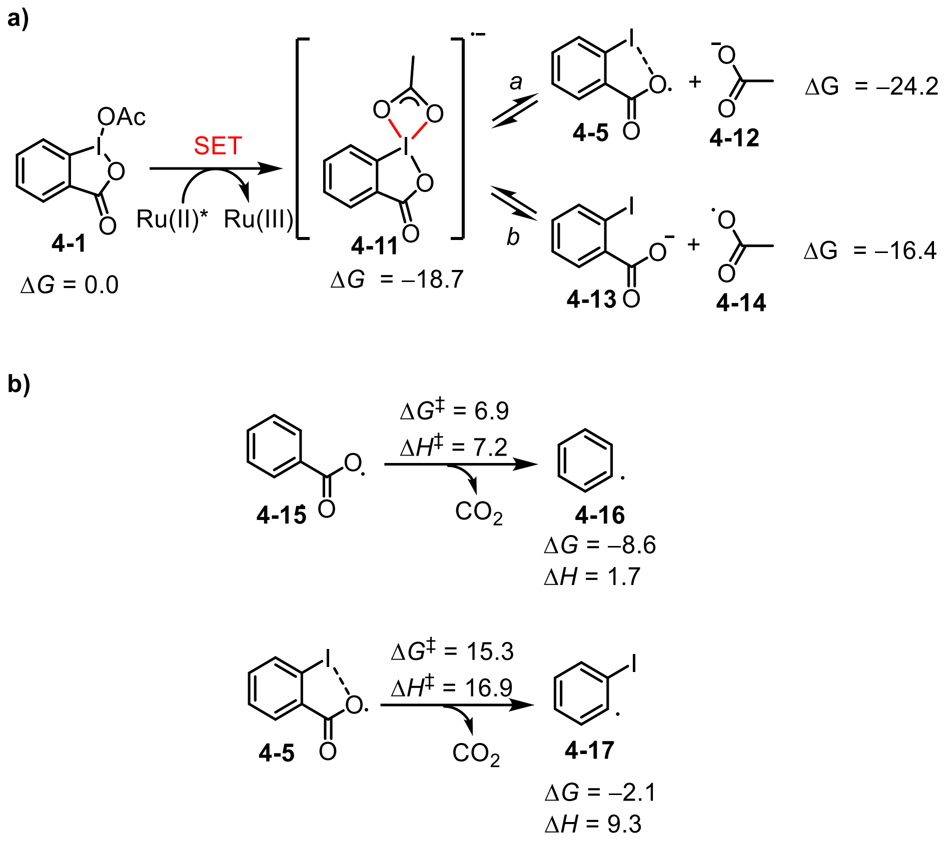

Figure 4-5. (a) Computed reaction energies of single electron transfer from the photo-excited catalyst Ru(II)* to BI-OAc and (b) decarboxylation of 4-15 and 4-5. All the energies are in kcal/mol.

Similar to the nucleo-homolytic substitution reaction of more reactive alkylboranes with *O*-centered radicals, **4-5** could react with the less Lewis-acidic boronic acids to form an alkyl radical **4-19** via a radical "ate" transition state.[100, 101, 102] DFT calculations showed that this is a facile process at ambient temperature and highly exothermic (**Figure 4-6**).

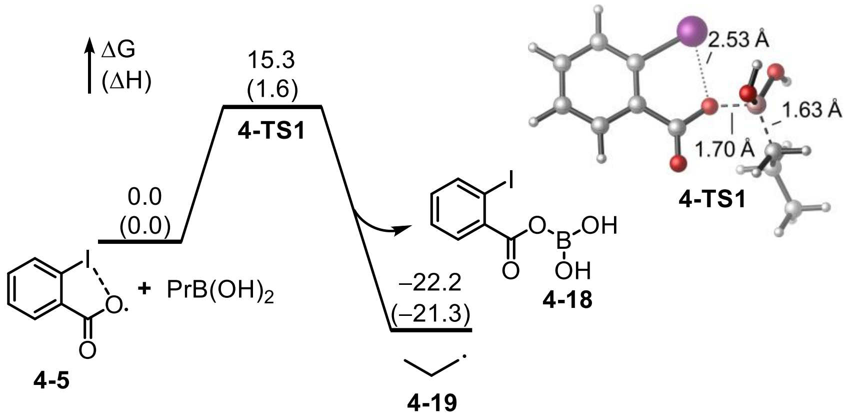

Figure 4-6. Energy profile for the generation of *n*-propyl radical intermediate from 4-5 and alkyl boronic acid.

Based on the above studies, it can be proposed that the reaction with boronic acid substrates is initiated with the SET from photoexcited Ru(II)* to **4-1** (**Figure 4-7**). The resulting **4-5** reacts with boronic acid to form an alkyl radical, which then undergoes nucleophilic addition reaction with protonated *N*-heteroarenes to form a σ-complex. Single-electron oxidation of this intermediate by Ru(III) and deprotonation gives the final C−H alkylated product and closes the photoredox cycle.

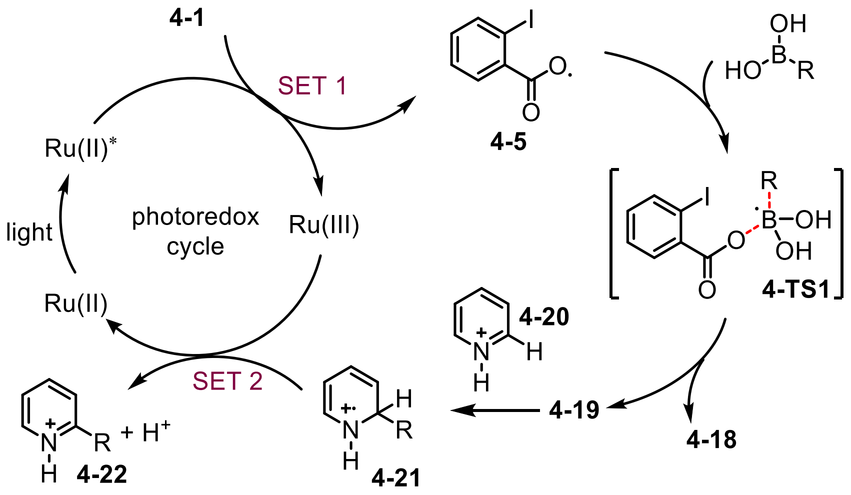

Figure 4-7. Proposed mechanism for the photoredox-mediated Minisci C−H alkylation of *N*-heteroarenes.

4.2.2 Photoredox C(sp^3)−H Hydroxylation Using Hypervalent Iodine as Oxidant

4.2.2.1 Computational details

All DFT calculations were performed with the Gaussian 09 software package.[46] Geometries were optimized using the M06-2X[48] functional and the 6-31+G(d) basis set in the gas phase. The SDD pseudopotential basis set was used for iodine atoms. Single point energies were calculated using M06-2X and 6-311++G(d,p) and the SMD[49] solvation model in HFIP. Since the solvent parameters for HFIP are not available in Gaussian 09 the parameters of isopropanol were used and the dielectric constant of the solvent was modified to the dielectric constant of HFIP[96] ($\varepsilon = 16.7$) by using the "scrf=(smd,solvent=2-propanol,read)" keywords in the Gaussian 09 calculations. The reported Gibbs free energies and enthalpies include zero-point vibrational energies and thermal corrections computed at 298 K. The experimental redox potentials of Ru(II)*(bpy)$_3$$^{3+/2+}$ (−0.81 V vs SCE in MeCN) and Ru(II)(bpy)$_3$$^{3+/2+}$ (+1.29 V vs SCE in MeCN) were used in the computation of the SET reaction energies with Ru(II)* and Ru(III) including the initial SET reduction with Ru(II) and in the subsequent SET oxidation with Ru(III). For detail explanation refer to section 4.2.1.2.

4.2.2.2 Computational study on mechanism of the photoredox C(sp^3)−H hydroxylation using hypervalent iodine as oxidant

Two C−O bond forming mechanisms were initially proposed by Chen for the C(sp^3)−H hydroxylation reaction: nucleophilic trapping of a carbocation intermediate with H_2O (pathway a) or a radical chain reaction with the hydroxyl benziodoxole reagents (pathway b) (**Figure 4-8**). However, experimental results reported by Chen suggested a non-radical chain mechanism.[94] The dependence of the reactivity on the H_2O cosolvent strongly support ionic pathway a. The mechanism of tertiary C−H hydroxylation with **4-2** likely begins with single electron transfer (SET) from photoexcited Ru(II)* to **4-2**, generating radical **4-3**. Radical **4-3** abstracts an H atom from alkane substrate **4-VII**, forming tertiary carbon radical **4-VIII**. **4-VIII** can be oxidized by the Ru(III) species, forming tertiary carbocation intermediate **4-IX**, and regenerating the photocatalyst. Finally, tertiary carbocation intermediate **4-IX** is trapped by H_2O to give the hydroxylated product **4-X**.

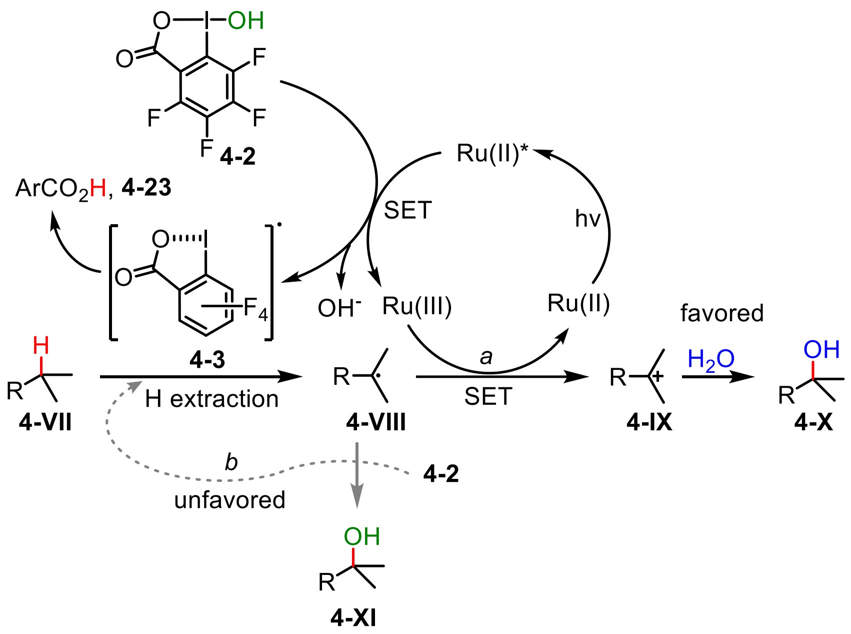

Figure 4-8. Proposed reaction mechanism for the photoredox C(sp^3)−H hydroxylation using 4-2.

DFT calculations using *t*-butane as the model substrate support the mechanism proposed by Chen (**Figure 4-9**). The reaction energy surfaces of the C−H hydroxylation using two hypervalent iodine reagents **4-2** and **4-4** were calculated. Calculations showed that the initial SET reduction of **4-2** to **4-3** is significantly more exergonic than the SET with **4-4** to **4-5** ($\Delta G = -4.9$ kcal/mol with **4-2** vs -0.9 kcal/mol with **4-4**). With its spin density delocalized over the O and I atoms, the radical intermediate **4-3** undergoes facile H-abstraction of *t*-butane through an O-centered transition state (**4-TS2**) with a $\Delta G^{\ddagger}$ of 16.6 kcal/mol to give **4-25**. This H-abstraction process is promoted by the electron-deficient perfluoroaryl group. The corresponding H-abstraction with the radical intermediate derived from **4-4** requires a noticeably higher barrier of 18.2 kcal/mol (**Figure 4-9b**). The subsequent oxidation of **4-25** by Ru(III) to **4-26** is highly exothermic. Finally, the carbocation **4-26** is trapped with H_2O, providing **4-27**. Taken together, the DFT calculations indicated the perfluorinated analogue **4-2** promotes both the initial SET reduction and the H-abstraction steps in the catalytic cycle of the tertiary C-H hydroxylation.

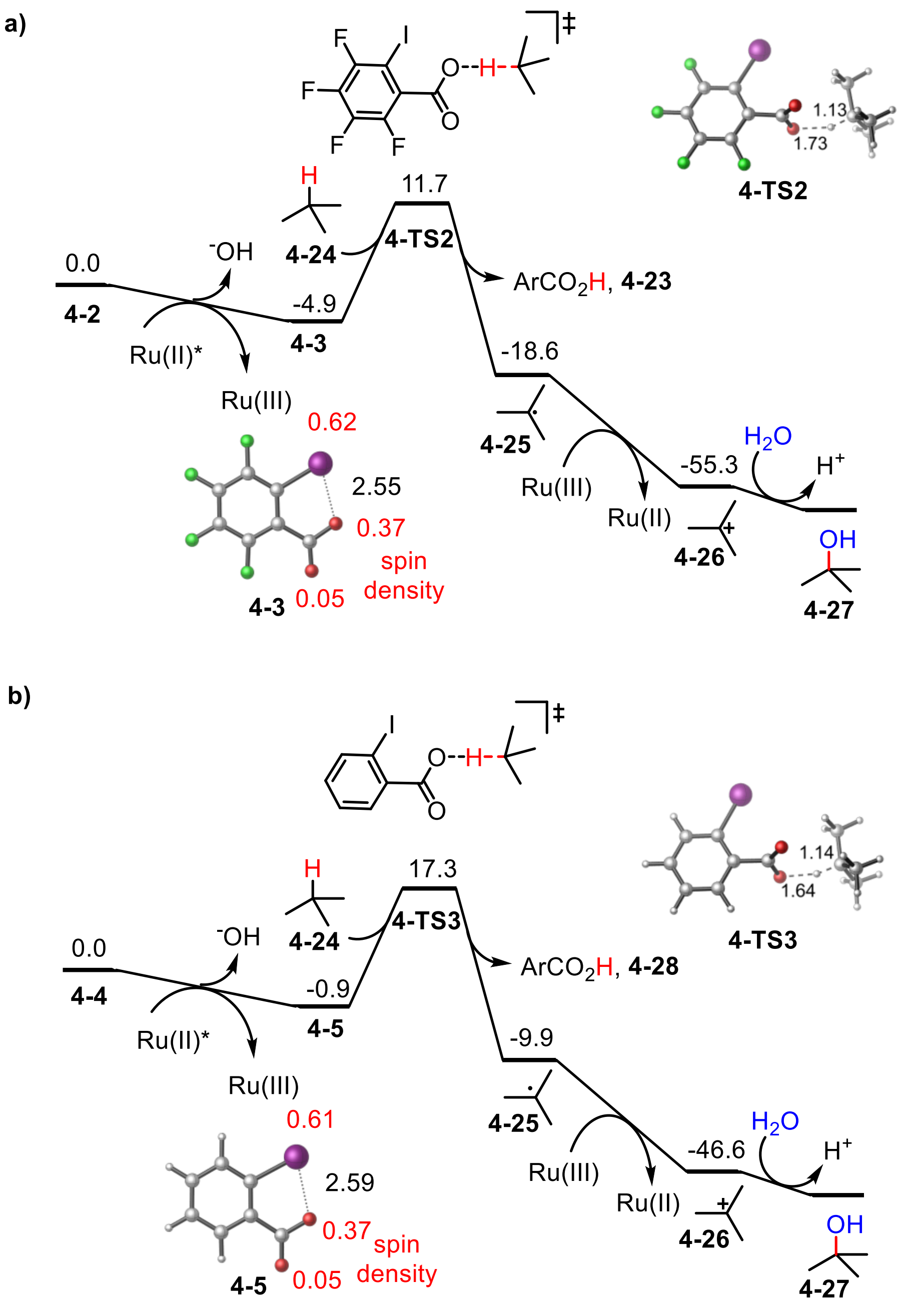

Figure 4-9. Potential energy profiles of C(sp^3)−H hydroxylation with (a) 4-2 and (b) 4-4.

4.2.3 Epimerization of Tertiary Carbon Centers via Reversible Radical Cleavage of Unactivated C(sp^3)−H Bonds

4.2.3.1 Computational details

All DFT calculations were performed with the Gaussian 09 software package.[45] Geometries were optimized using the M06-2X[48] functional and the 6-31+G(d) basis set. The SDD pseudopotential basis set was used for iodine atoms. Single point energies were calculated using M06-2X and 6- 311++G(d,p)-SDD basis set. The SMD[49] solvation model in EtOAc solvent was used in the geometry optimization and single point energy calculations.

4.2.3.2 Computational studies on the epimerization of tertiary carbon centers via reversible radical cleavage of unactivated C(sp^3)−H bonds

Control experiments performed by Chen and density functional theory (DFT) calculations have been carried out to understand the mechanism and the role of the hypervalent iodine reagent of the BlN$_3$/H$_2$O-mediated C(sp^3)−H epimerization reaction.[95] As outlined in **Figure 4-10**, a radical-mediated 3^o C−H epimerization reaction would require efficient H-abstraction by an H-acceptor (A•) as well as selective quenching of the resulting carbon radical intermediate by an H-donor (D−H). Ideally, A• should not react with D−H, avoiding non-productive consumption of donor and acceptor.[103] Furthermore, competing reaction pathways of the carbon radical intermediates need to be suppressed to achieve clean epimerization. Therefore, selection of effective H-acceptor/donor is critical for the success of the epimerization reaction. Computational studies were performed to investigate the potential radical intermediates in the reaction system and their stability and reactivity towards C−H abstraction.

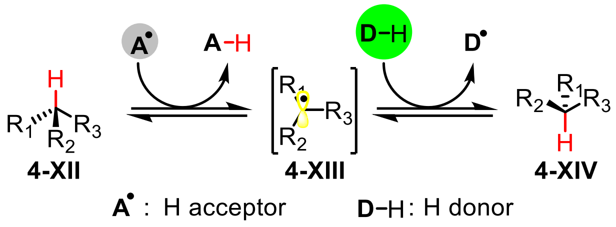

Figure 4-10. Epimerization strategy via reversible cleavage of nonacidic 3º C–H bond.

Previous studies performed by Chen have shown that **4-6** is uniquely effective at initiating the C–H activation step through the formation of H-acceptor **4-5** or N_3• via dissociative SET or homolytic cleavage of the I–N bond at elevated temperature (**Figure 4-11**).[69a] In this reaction system, homolytic I–N cleavage of **4-6** is expected to occur at ambient temperature in the absence of light irradiation. This is supported by the DFT calculations that indicated a very small BDE of 27.8 kcal/mol for the I–N bond of **4-6**, compared to the calculated I–O BDEs for **4-4** and **4-1** (42.3 and 42.5 kcal/mol, respectively). More importantly, $H–N_3$ has a BDE of 93.3 kcal/mol, which is very close to the BDE of unactivated 3º C–H bonds (93.3 and 96.1 kcal/mol for 3º C-H of **4-33** and **4-31**, respectively). In comparison, the 2º C–H bonds of cyclohexane **4-29** have a larger BDE of 97.5 kcal/mol. The close match in BDE of $H–N_3$ and unactivated 3º C-H not only renders N_3• a competent H-acceptor for 3º C–H bond but also makes $H–N_3$ a suitable H-donor to 3º carbon radical intermediate, making N_3• an effective hydrogen atom shuttle for 3º C-H bonds. Although H_2O is critical to the success of this epimerization reaction, H_2O is unlikely the immediate H-donor due to the high BDE of H-OH (~ 117.2 kcal/mol).

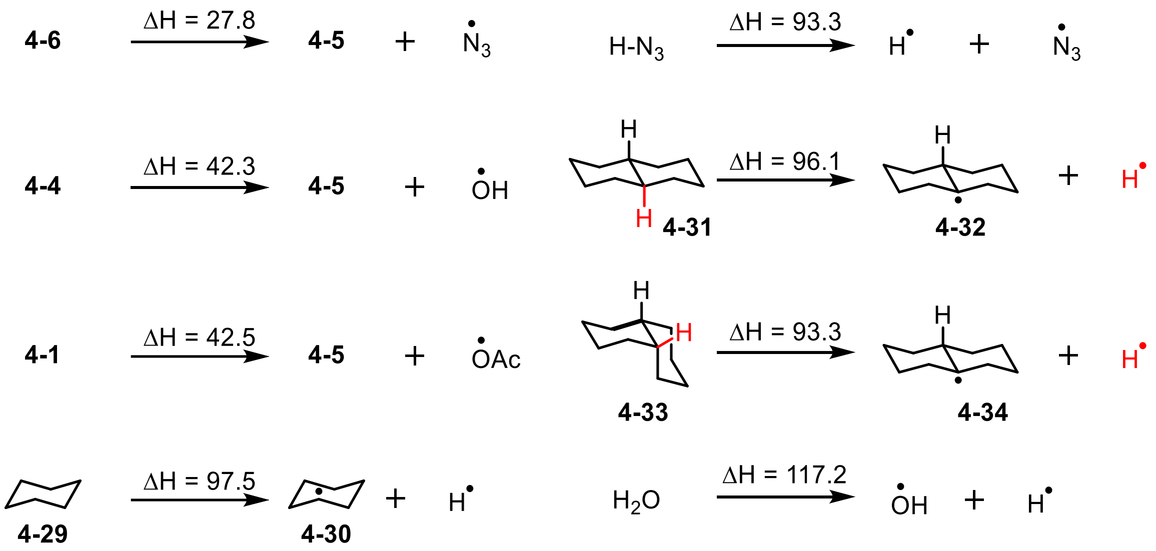

Figure 4-11. Computed BDE using DFT calculations. All energies are in kcal/mol.

Experimental results from Chen research group suggest that the residual **4-6**, rather than HN_3 or **4-4**, is responsible for the initiation of C–H epimerization.[69a] Since **4-6** is an excellent azidation reagent for carbon radicals, the low concentration of **4-6** and the abundance of HN_3 in the reaction system might contribute to the suppression of the competing C–H azidation pathway. As outlined in the proposed reaction pathway by Chen in **Figure 4-12**, this epimerization reaction likely starts with a homolytic cleavage of the residual **4-6**, generating **4-5** and N_3• radical. N_3• then selectively cleaves a 3^o C-H bond of alkane **4-V** forming carbon radical **4-XVII** and HN_3.[104] Nucleophilic carbon radical **4-XVII** then reacts with the electrophilic H-donor HN_3[105] to give the epimerization product **4-VI** or **4-V** and regenerate N_3•, thus propagating a radical chain reaction.

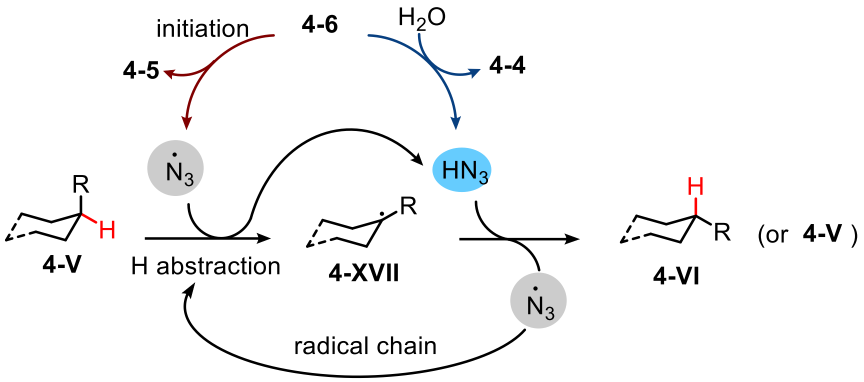

Figure 4-12. Proposed reaction mechanism for the epimerization of carbon centers via reversible radical cleavage of unactivated C(sp^3)−H bonds.

DFT calculations of the epimerization of *cis*-decalin **4-33** show that both the initial H abstraction by N_3• and the subsequent quenching of tertiary carbon radical with HN_3 proceed with low energy barriers.[106,107] The late transition state (r(C-H) = 1.32 Å) suggests the rate and selectivity of the C−H abstraction are sensitive to the BDE of the C−H bonds.[108] This is in agreement with the high levels of regioselectivity for 3^o C−H bonds in this epimerization reaction. DFT calculations also indicate the more sterically hindered **4-5** is less effective than N_3• at cleaving the 3^o C−H bond of alkane **4-33**. Overall, the facile activation of **4-6**, the proper equilibrium between 4-6 and HN_3 in the presence of H_2O, and the unique ability of N_3• as a catalytic hydrogen atom shuttle enable an efficient, selective, and clean radical 3^o C−H epimerization under mild conditions.

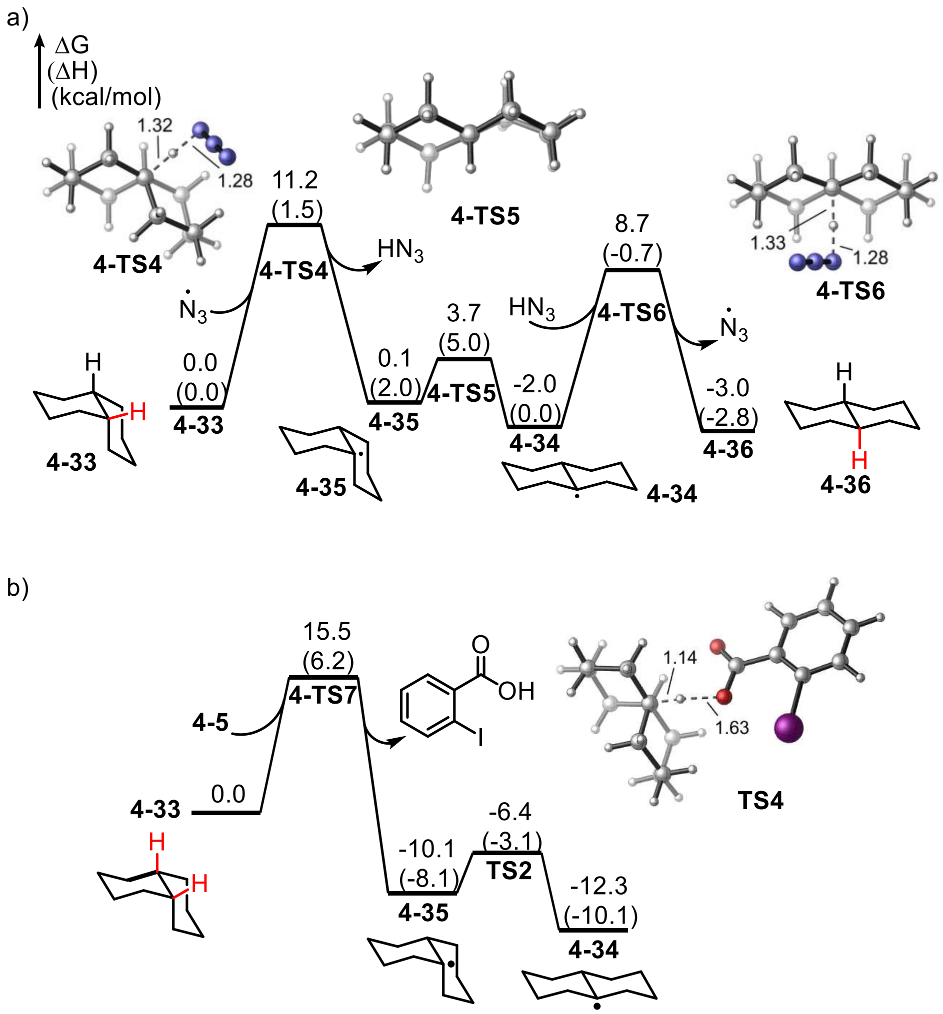

Figure 4-13. Computed potential energy profiles for the epimerization of carbon centers via reversible radical cleavage of unactivated C(sp^3)−H bonds by (a) N$_3$• and (b) 4-5.

4.3 CONCLUSION

DFT calculations were performed to investigate the mechanism of the photoredox-mediated Minisci C−H alkylation of *N*-heteroarenes using boronic acid and hypervalent iodine reagents (section 4.2.1). Calculations showed that acetoxybenziodoxolone **4-1** serves as a facile precursor to generate an O/I radical intermediate **4-5** under photoredox catalysis. This intramolecularly stabilized radical **4-5** is prone to the undesired decarboxylation reaction. Instead, it reacts favorably with the alkyl boronic acids to form alkyl radicals to initiate the Minisci C−H alkylation.

Perfluorinated analogue **4-2** was found to be a useful reagent for the photoredox-mediated $C(sp^3)$−H hydroxylation (section 4.2.3). Calculations showed that **4-2** promotes both the initial SET reduction and the H-abstraction steps in the catalytic cycle of the tertiary C−H hydroxylation. Distinct from the radical chain mechanism proposed by Chen[69a] for the C−H azidation reaction with **4-6**, DFT calculations suggest a photoredox catalyzed formation of a carbocation intermediate, followed by nucleophilic trapping with H_2O.

DFT calculations were also performed for the mechanistic study of epimerization of tertiary carbon centers via reversible radical cleavage of unactivated $C(sp^3)$−H bonds (section 4.2.3). Calculations showed that the facile activation of **4-6** at ambient temperature, the proper equilibrium between **4-6** and HN_3 in the presence of H_2O, and the unique ability of $N_3\bullet$ as a catalytic hydrogen atom shuttle enable efficient, selective, and clean radical 3° C−H epimerization.

Taken together, computational results in this Chapter demonstrated that DFT calculation can provide useful insights into the reactivity of potential reaction intermediates, the origin of reactivities of different hypervalent iodine reagents, and the detailed reaction mechanisms in the initiation, C-H abstraction, and functionalization steps.

5.0 COMPUTATIONALS STUDIES OF C–H BOND TRIFLUOROMETHOXYLATION AND DIFLUOROMETHOXYLATION OF ARENES AND HETEROARENES

Reproduced from Katarzyna N. Lee, Zhen Lei, Cristian A. Morales-Rivera, Peng Liu, and Ming-Yu Ngai. “Mechanistic Studies on Intramolecular C−H Trifluoromethoxylation of (Hetero)arenes via OCF_3-migration” *Org. Biomol. Chem.* **2016**, 14, 5599-5605 with permission from the Royal Society of Chemistry.

A significant part of this chapter was published as; Weijia Zheng, Cristian A. Morales-Rivera, Johnny W. Lee, Peng Liu, Ming-Yu Ngai. “Catalytic C−H Trifluoromethoxylation of Arenes and Heteroarenes” *Angew. Chem. Int. Ed.* **2018**, 57, 9645-9649; Weijia Zheng, Johnny W. Lee, Cristian A. Morales-Rivera, Peng Liu, and Ming-Yu Ngai. “Redox-Active Reagents for Photocatalytic Generation of the OCF_3 Radical and (Hetero)Aryl C−H Trifluoromethoxylation” *Angew. Chem. Int. Ed.* **2018**, 57, 13795-13799; Johnny W. Lee, Weijia Zheng, Cristian A. Morales-Rivera, Peng Liu, and Ming-Yu Ngai. “Catalytic Radical Difluoromethoxylation of Arenes and Heteroarenes” *Chem. Sci.* **2019**, 10, 3217-3222. In this work, I designed and carried out DFT calculations and analysis of computational results. The experimental part was performed by Ngai research group.

5.1 INTRODUCTION

Modern drug discovery and development involves extensive fine-tuning of physicochemical properties of drug candidates. A common approach to modify the physicochemical properties involves the incorporation of fluorinated functional groups, such as the trifluoromethoxy (OCF_3) and difluoromethoxy (OCF_2H) groups, into drug candidates[109]. The OCF_2H and OCF_3 groups are privileged functional groups in the realm of medicinal chemistry because their incorporation into organic molecules often enhances efficacy by increasing metabolic stability, enhancing cellular membrane permeability, and improving pharmacokinetic properties[110]. Thus, tri- and difluoromethoxylation of arenes and heteroarenes are of great importance in medicinal chemistry (**Figure 5-1**). Although a number of prescribed pharmaceutical agents bear OCF_3 or OCF_2H motifs in an aromatic system, access to such analogues often requires the installation of these groups at the early stage of a multi-step synthetic sequence.

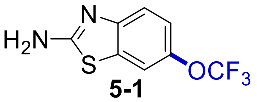

5-1
Riluzole
(treatment of
amyotrophic lateral sclerosis)

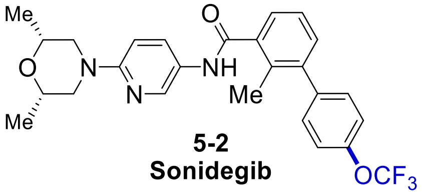

5-2
Sonidegib
(anticancer agent)

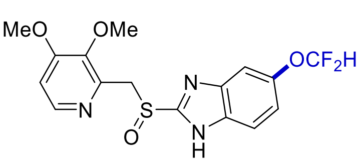

5-3
Pantoprazole
(Anti-inflamatory Drug)

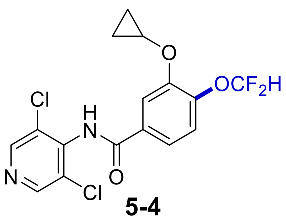

5-4
Roflumilast
(Anti-inflamatory Drug)

Figure 5-1. OCF_3- and OCF_2H-containing marketed drugs.

In 2016, the Ngai research group developed a new method for preparation of *ortho*-OCF_3 (hetero)arylamine derivatives *via* a two-step process: *O*-trifluoromethylation of *N*-(hetero)aryl-*N*-hydroxylamine derivatives followed by OCF_3-migration step (**Figure 5-2**).[111] This approach is operationally simple and amenable to gram-scale synthesis, features a broad substrate scope and high functional group compatibility, and provides a wide range of valuable *ortho*-trifluoromethoxylated (hetero)arylamine scaffolds that would otherwise be difficult to synthesize.

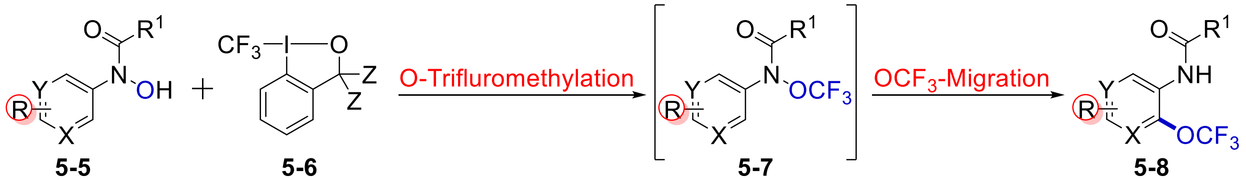

5-5 **5-6** **5-7** **5-8**

R1 = Me, OMe, Ph, or NMe_2
X, Y = CH or N

Togni reagents
(1.2 equiv)
Z = O or Me

Isolable

> 50 examples
up to 95% yield

Figure 5-2. Synthesis of (hetero)aryl trifluoromethyl ethers via O-trifluromethylation of N-(hetero)aryl-N-hydroxylamine derivatives followed by OCF_3-migration.

In order to develop better synthetic strategies for the C–H trifluoromethoxylation of arenes and heteroarenes, Ngai research group synthetized a novel OCF_3-reagent **5-9**[111, 112] (**Figure 5-3**). They took advantage of the relatively weak N-OCF_3 bond to generate $OCF_3^{\bullet}$ by means of Ru(II) photo-redox catalyst. They found that the $OCF_3^{\bullet}$ may be trapped intermolecularly by arenes and heteroarenes to afford the product of trifluoromethoxylation (**Figure 5-3a**). Although reagent **5-9** is capable of trifluoromethoxylation of arenes and heteroarenes, the reaction is complicated by the formation of the *N*-arylated side product **5-III.**[113a] This is due to the fact that the formation of $OCF_3^{\bullet}$ is a stochiometric process because whenever reagent **5-9** is photoexcited, the N-OCF_3 bond would homolyze to form two radical species. In order to avoid this, they synthesized reagents **5-10** and **5-11** for the C–H tri- and difluoromethoxylation of arenes and heteroarenes by means of Ru(II) photo-redox catalyst (**Figure 5-3b** and **Figure 5-3c**).[113] Under these conditions they were able to generate the $OCF_3^•$ and $OCF_2H^•$ as the only radical species. They demonstrated that this protocol is applicable to late-stage functionalization of marketed drugs, which provides a useful tool in the synthesis and development of new medicinal agents.

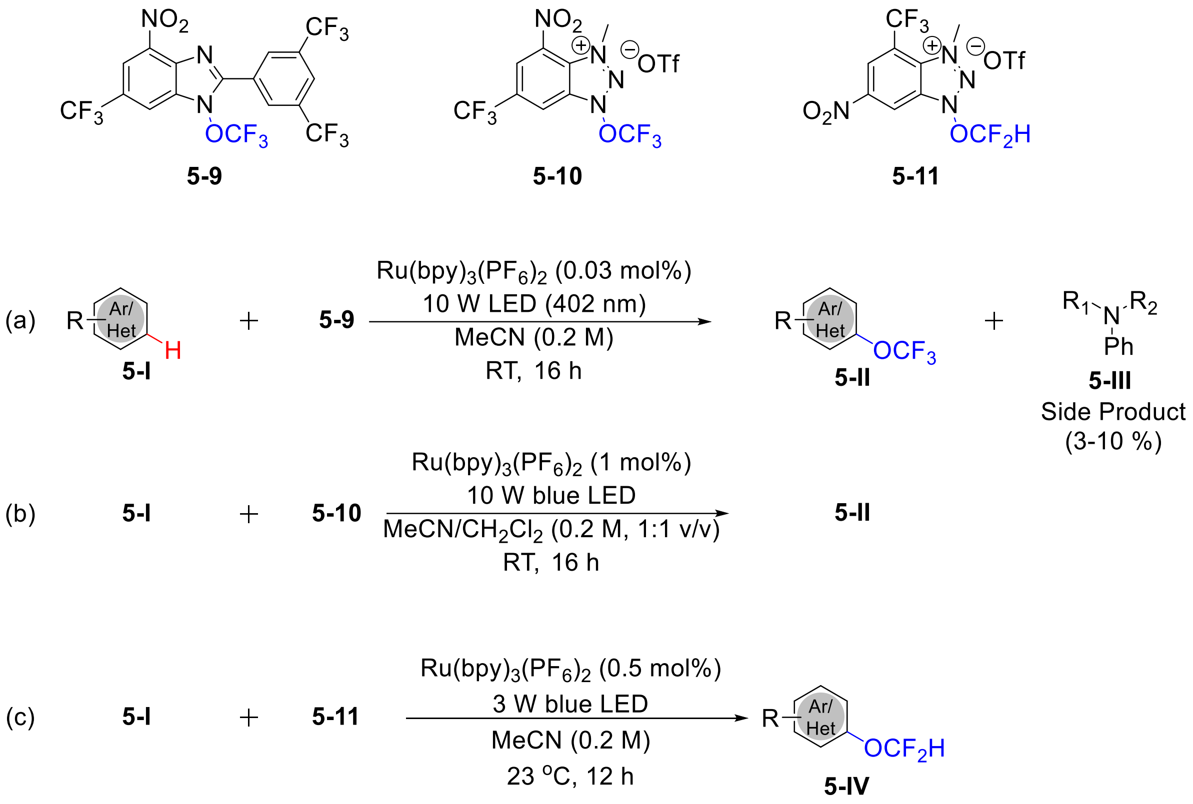

Figure 5-3. Tri- and difluoromethoxylation of arene and heteroarenes by means of Ru(II) photo-redox catalyst.

In view of the synthetic utility of C–H tri- and difluoromethoxylation of arenes and heteroarenes by OCF_3-migration or by the use of OCF_3- (**5-9** and **5-10**) and OCF_2H-reagents (**5-**

11) under photo-redox catalyst conditions, an in-depth understanding of the reaction mechanisms is desirable. This chapter describes a computational study on the mechanisms of C–H tri- and difluoromethoxylation of arenes and heteroarenes by OCF_3-migration and by means of photo-redox catalysis.

5.2 RESULTS AND DISCUSSION

5.2.1 Intramolecular C–H Trifluoromethoxylation of (Hetero)arenes via OCF_3-Migration

DFT calculations were conducted in order to elucidate whether the migration of the OCF_3 group from intermediate **5-7** occurs through a concerted or a stepwise mechanism. Calculations were also performed in order to explore the stability and the reactivity of the intermediate involved in the stepwise pathway.

5.2.1.1 Computational details

All DFT calculations were performed with the Gaussian 09 software package.[46] Geometries were optimized using the M06-2X[48] functional and the 6-31+G(d). The SMD[49] solvation model and $MeNO_2$ solvent were used in the calculations. Single point energies were calculated using M06-2X and 6-311++G(d,p) and the SMD solvation model in $MeNO_2$. Reported Gibbs free energies and enthalpies in solution include thermal corrections computed at 298 K.

5.2.1.2 Experimental mechanistic studies performed by the Ngai research group on the OCF3-migration of N-(trifluoromethoxy)-N-aniline derivatives (5-7)

To gain mechanistic insights into the OCF3-migration step, Ngai group first examined whether the N–O bond is broken homo- or heterolytically. Homolytic cleavage of the N–OCF3 bond would generate *N*-amidyl and trifluoromethoxyl (OCF3) radicals; if these radicals are indeed being formed, the reaction yield is expected to drop upon addition of a radical trap, which would disable radical recombination process. Thus, Ngai research group performed the rearrangement reaction of **5-7a** in the presence of a stoichiometric amount of BHT (**Figure 5-4**). Similar yields were obtained regardless the presence or absence of BHT, which indicates that formation of long-lived radical species under the reaction conditions is unlikely.

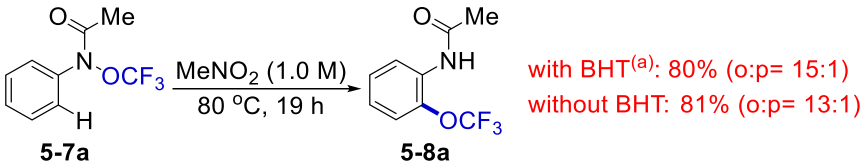

Figure 5-4. OCF3-migration in presence of a radical trap. (a) 1 equiv.

In order to further shed light to the nature of cleavage of the N–O bond, Ngai group performed linear free energy relationship analysis using Hammett plot. The Hammett plot of log (k_R/k_H) versus σ showed a highly negative linear slope ($\rho = -11.86$; $R^2 = 0.99$) (**Figure 5-5**), which is commonly observed in organic reactions involving formation of a positive charge.[114] Therefore, these results strongly suggest a heterolytic cleavage of the N–OCF3 bond, in which a nitrenium ion and trifluoromethoxide are generated. While the presence of nitrenium ion was evidenced by the Hammett analysis, the intermediacy of trifluoromethoxide was corroborated by detection of fluorophosgene (decomposition product of trifluoromethoxide) and BF_4^- by ^{19}F NMR spectroscopy.[115]

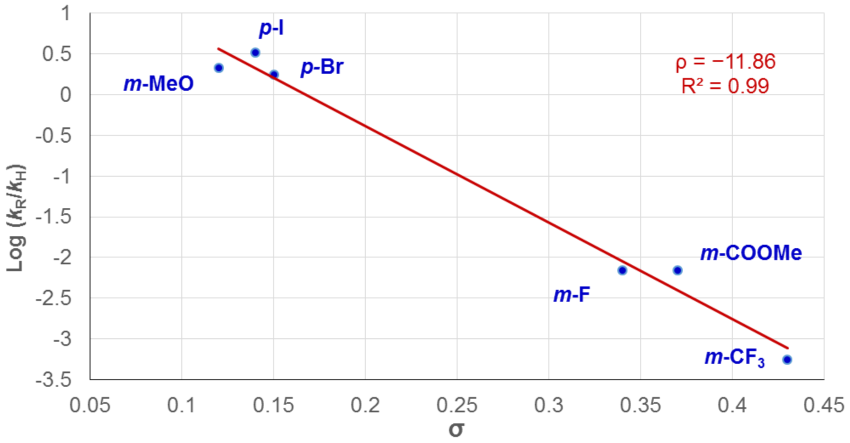

Figure 5-5. Hammett plot for OCF3-migration of R–C6H4N(OCF3)C(O)Me (R = m-OMe, p-I, p-Br, m-F, m-CO2Me, and m-CF3).

The last step performed by Ngai research group in order to elucidate the mechanism for the OCF_3-Migration was to determine if the final carbon–OCF_3 bond forming step is an intramolecular reaction. To do so, they performed a cross-over experiment using *N*-(4-bromophenyl)-*N*-(trifluoromethoxy)acetamide (**5-7b**) and *N*-(4-chlorophenyl)-*N*-(perfluoroethoxy)acetamide (**5-12**). Heating **5-7b** and **5-12** together either in $MeNO_2$ or neat at 80 °C formed only non-crossover products (**5-8b** and **5-13**) as monitored by GC-MS or ^{19}F NMR (**Figure 5-6a**). The lack of cross-over products suggests that the OCF_3-migration is likely an intramolecular process and that the rate of recombination of a tight ion pair is much faster than an intermolecular OCF_3-group transfer, which would require dissociation of two ions of opposite charge. The intramolecular mechanism is further corroborated by formation of benzoxazole **5-8c’** during the rearrangement reaction of methyl 4-(*N*-(trifluoromethoxy)benzamido)benzoate (**5-7c**)

(**Figure 5-6b**). This side product results from a competing intramolecular trapping of the nitrenium ion by an internal nucleophile, and its isolation further confirms that the nitrenium ion intermediates are very reactive and thus short lived.

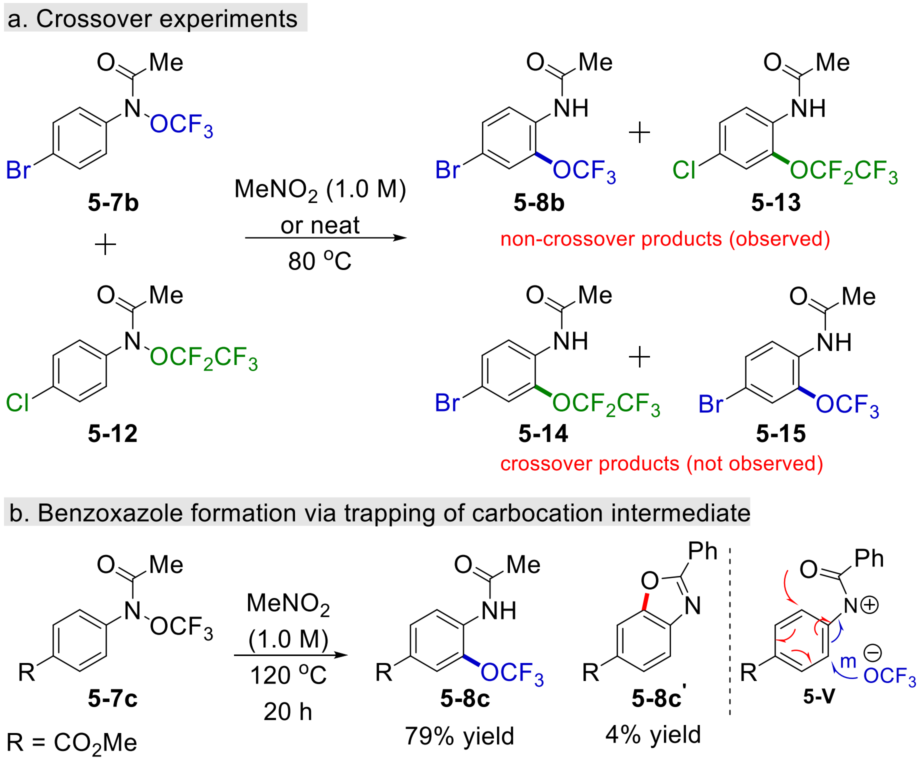

Figure 5-6. Crossover and trapping of carbocation intermediate experiments.[116]

5.2.1.3 Computational study of the mechanism of the OCF_3-migration

The computed reaction energy profile of the stepwise OCF_3 migration is shown in **Figure 5-7a**.[117] The heterolytic cleavage of the N–OCF_3 bond of **5-7a** to form the ion pair intermediate (**5-16**) requires an activation free energy of 27.6 kcal mol^{-1} (**5-TS1**),[118] which is feasible under the experimental conditions (80 °C). The ion pair (**5-16**) is an anion–π complex[119] between trifluoromethoxide and the highly electron-deficient phenyl ring. The relatively strong anion–π interaction is evidenced by the short O(OCF3)–C distances (**Figure 5-7b**). The recombination of the ion pair (**5-16**) through O–C (ortho) bond formation to yield the dearomatized intermediate **5-17** requires a very low barrier and is highly exothermic. This indicates a very short lifetime of the ion pair intermediate, which agrees with the crossover experiments. The low barrier of the ion pair recombination is attributed to the structural similarity of **5-16** and **5-TS2**. The O(OCF3)–C(ortho) distance is only slightly shortened to 2.45 Å in the recombination transition state (**5-TS2**). The subsequent 1,3-hydrogen shift from the dearomatized intermediate **5-17** to the final product **5-8a** occurs through a stepwise mechanism involving the autoionization of **5-17** to form **5-18a** and **5-18b** followed by the highly exothermic proton transfer from **5-18a** to **5-18b** to form **5-8a**.[120]

a. Reaction energy profile of the OCF_3-migration of **5-7a**

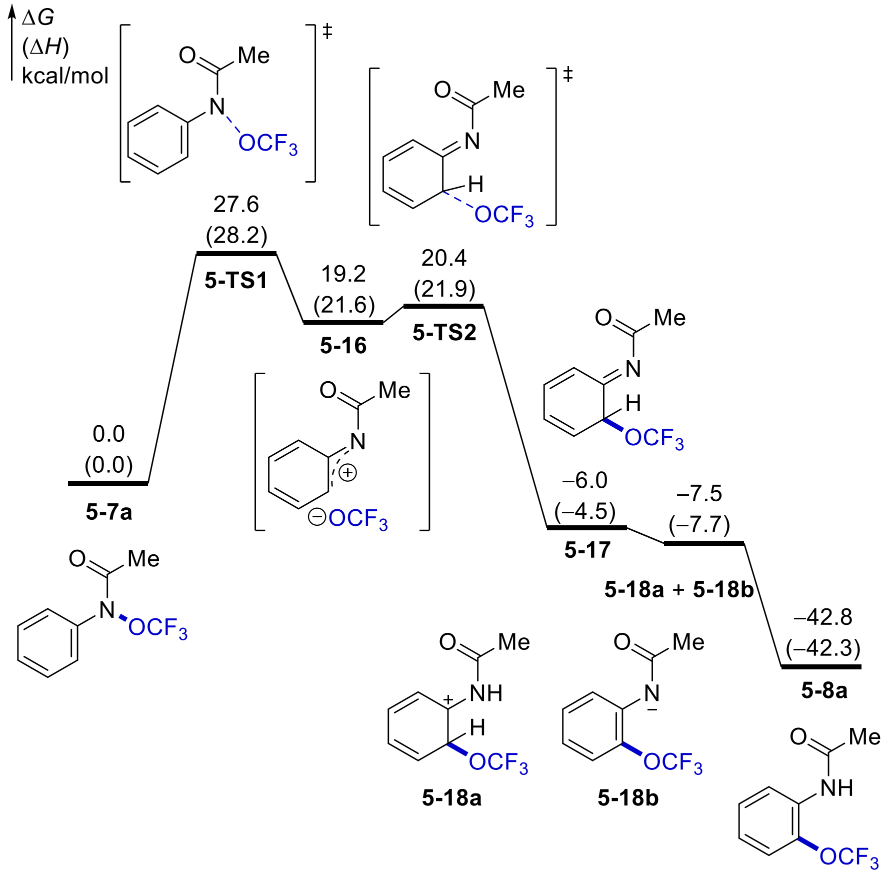

b. Optimized geometries of the ion-pair intermediate **5-16** and the transition states of N–O cleavage (**5-TS1**) and C–O formation (**5-TS2**)

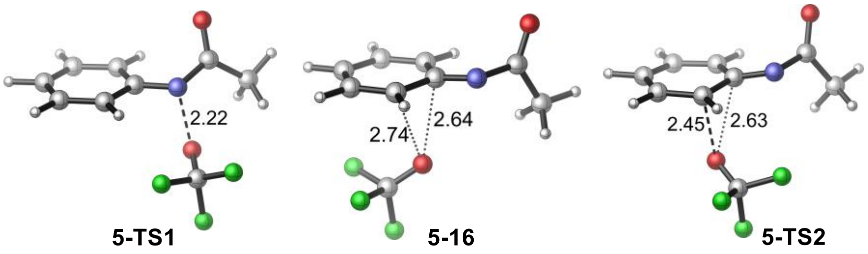

Figure 5-7. Computational investigations of the mechanism of OCF_3-Migration of 5-7a.

The concerted OCF_3 migration transition state that directly connects **5-7a** and the dearomatized intermediate **5-17** cannot be located in the geometry optimization. To evaluate if such concerted pathway exists and competes with the stepwise process, the potential energy surface of the OCF_3 migration was constructed at the M06-2X/6-31+G(d)/SMD($MeNO_2$) level of theory and is shown in **Figure 5-8**. The stationary points in the stepwise pathway (**5-7a**, **5-TS1**, **5-16**, **5-TS2**, and **5-17**) are labeled on the surface. The potential energy surface clearly indicates that the concerted reaction pathway, in which the C-O bond formation and the N-O bond cleavage take place simultaneously, requires a much higher barrier than the stepwise pathway (**5-TS1** and **5-TS2**). The stepwise pathway described in **Figure 5-7** is thus more favorable than the concerted process.

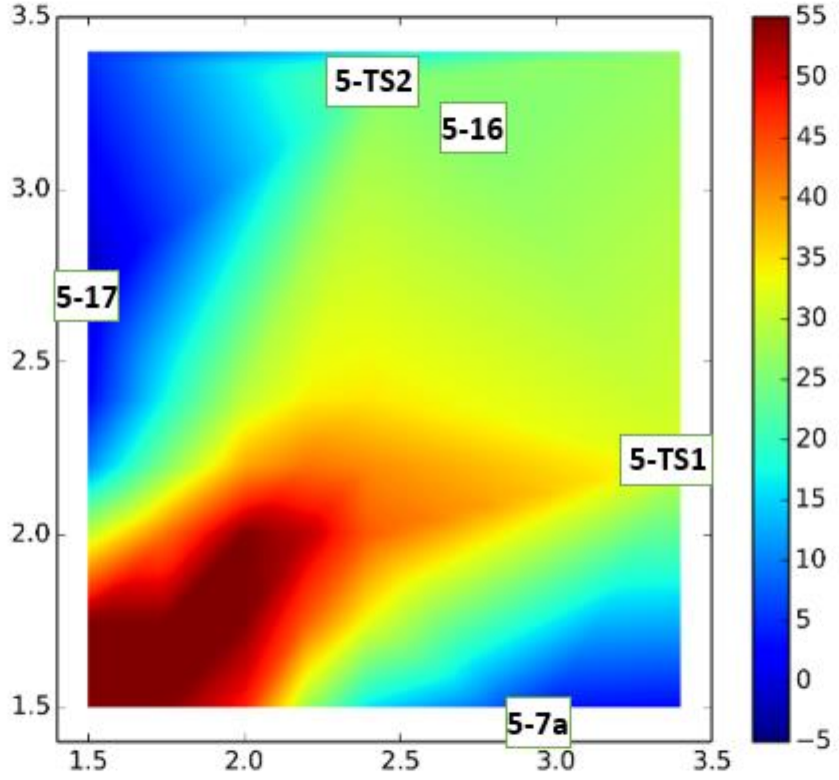

Figure 5-8. Potential energy surface of OCF_3 migration from 5-7a to form 5-17.

Altogether, these results are consistent with the proposed mechanism from Ngai group shown in **Figure 5-9**. The N–O bond of **5-7** undergoes the thermally induced heterolytic cleavage to form a short-lived ion pair of a nitrenium ion and trifluoromethoxide. Rapid recombination of this ion pair affords intermediate **5-VI**, which then tautomerizes to restore aromaticity and generates the desired product **5-8**. The ionic mechanism for the N–O bond cleavage of N-protected N-aryl-N-hydroxylamines is also well precedented in the literature.

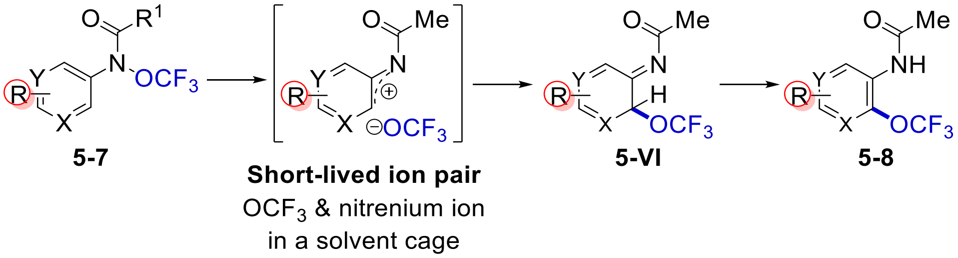

Figure 5-9. Proposed mechanism for the OCF_3-migration process.

In addition to studying the reaction mechanism of the OCF_3 migration of **5-7a**, the reaction with compound **5-7c** was also computed in order to explore the effect of electron-withdrawing group on reactivity. The experimental Hammett plot indicated electron-withdrawing group dramatically slows down the OCF_3 migration (**Figure 5-5**). The computed reaction energy profile of the stepwise OCF_3 migration of **5-7c** is shown in **Figure 5-10a**. The rate-determining heterolytic cleavage of the N–OCF_3 bond of **5-7c** to form the ion pair intermediate (**5-19**) requires an activation free energy of 32.2 kcal mol^{-1} (**5-TS3**). This energy barrier is 4.6 kcal/mol higher than that of the heterolytic cleavage of the N–OCF3 bond for substrate **5-7a**. The intermediate nitrenium ion (**5-19**) is destabilized with by the electron-withdrawing group. These results are in complete agreement with the experimental results from the Ngai group that the OCF_3-migration is very slow at 80 ^{o}C for substrate bearing a strongly electron withdrawing group at the para-position.

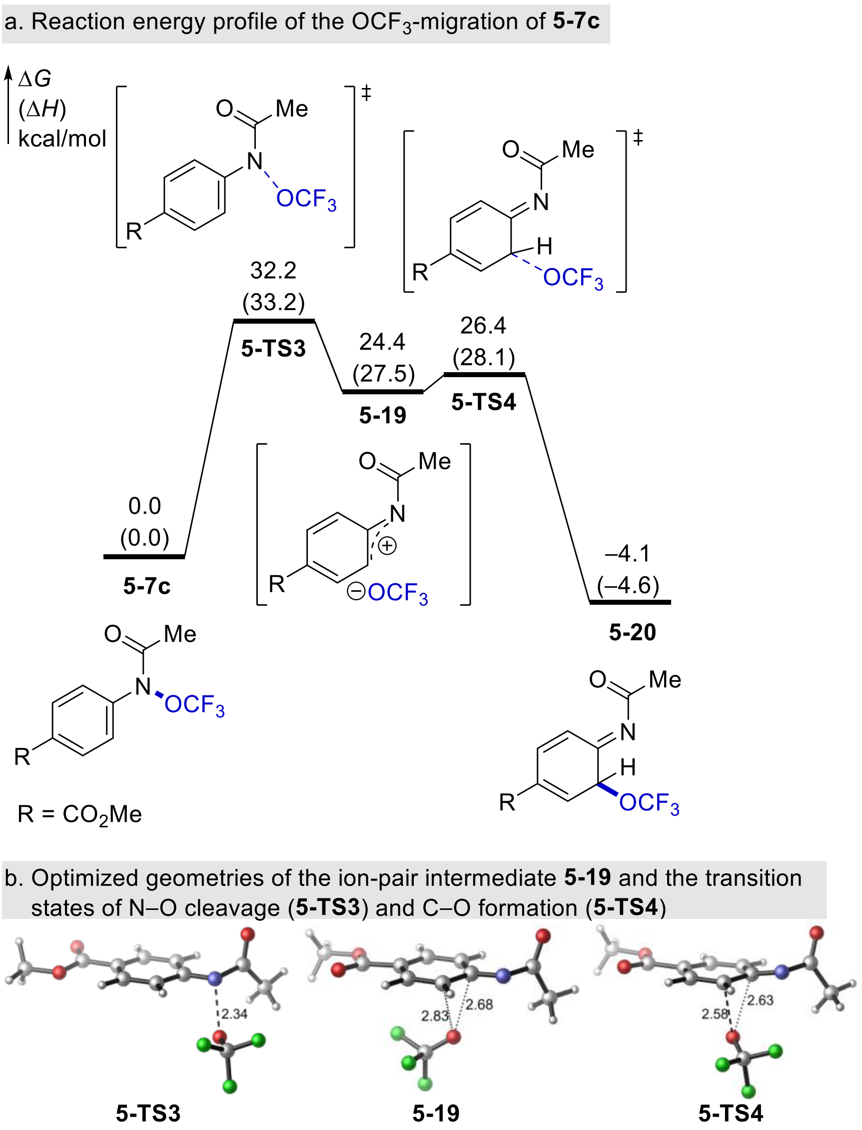

a. Reaction energy profile of the OCF_3-migration of **5-7c**

b. Optimized geometries of the ion-pair intermediate **5-19** and the transition states of N–O cleavage (**5-TS3**) and C–O formation (**5-TS4**)

Figure 5-10. Computational investigations of the mechanism of OCF_3-Migration of 5-7c.

The recombination of the ion pair (**5-19**) through O–C (ortho) bond formation to yield the dearomatized intermediate **5-20** requires a very low barrier and is highly exothermic. This indicates once again a very short lifetime of the ion pair intermediate, which agrees with the crossover experiments. The low barrier of the ion pair recombination can also be attributed to the structural similarity of **5-19** and **5-TS4**. The $O(OCF_3)$–C(ortho) distance is only slightly shortened to 2.58 Å in the recombination transition state (**5-TS4**).

5.2.2 C–H Trifluoromethoxylation of Arenes and Heteroarenes Using OCF_3-Reagent 5-9 by Means of Ru(II) Photoredox Catalyst

Mechanistic DFT calculations describe in this section were conducted in order to shed light on the reaction mechanism of C–H trifluoromethoxylation of arenes and heteroarenes using OCF_3-reagent **5-9** under photo-redox conditions (**Figure 5-3a**). Calculations were performed in order to explore the role of the photoredox catalyst and 5-9.

5.2.2.1 Computational details

All DFT calculations were performed with the Gaussian 09 software package.[46] Geometries were optimized using the M06-2X[48] functional and the 6-31+G(d). The SMD[49] solvation model and MeCN solvent were used in the calculations. Single point energies were calculated using M06-2X and 6-311++G(d,p) and the SMD solvation model in MeCN. Reported Gibbs free energies and enthalpies in solution include thermal corrections computed at 298 K. The experimental standard reduction potential (SRP) of $Ru^*(bpy)_3^{2+}$ (−0.81 V vs. SCE in MeCN)[121] was used in the computations of the reaction Gibbs free energies of the single electron transfer (SET) processes with the photoredox catalyst.

5.2.2.2 Reaction energy of single electron transfer involving the Ru(II) photoredox catalyst

The photoexicted Ru(II)*(bpy)$_3^{2+}$ is a potent reductant with an experimental standard reduction potential (SRP) of −0.81 V vs. SCE in MeCN while its ground state SRP is 1.29 V in the same medium.[121] Thus, the absolute SRP in MeCN can be calculated as follows:[122]

$$E^{\ominus,\mathrm{abs}}_{\mathrm{Ru(bpy)}_3^{3+/2+*}} = E^{\ominus,\mathrm{SCE}}_{\mathrm{Ru(bpy)}_3^{3+/2+*}} + 4.429\mathrm{V} = -0.81\mathrm{V} + 4.429\mathrm{V} = 3.62\mathrm{V}$$

$$E^{\ominus,\mathrm{abs}}_{\mathrm{Ru(bpy)}_3^{3+/2+}} = E^{\ominus,\mathrm{SCE}}_{\mathrm{Ru(bpy)}_3^{3+/2+}} + 4.429\mathrm{V} = 1.29\mathrm{V} + 4.429\mathrm{V} = 5.72\mathrm{V}$$

Since

$$\Delta G = -nFE$$

where n is the number of electrons transferred (one), F is the Faraday constant, the Gibbs free energy of the following reduction half reaction is

$$\mathrm{Ru(bpy)}_3^{3+} + e^- \rightarrow \mathrm{Ru^*(bpy)}_3^{2+} \qquad \Delta G_{\mathrm{MeCN}} = -83.5\ \mathrm{kcal/mol} \qquad (1)$$

$$\mathrm{Ru(bpy)}_3^{3+} + e^- \rightarrow \mathrm{Ru(bpy)}_3^{2+} \qquad \Delta G_{\mathrm{MeCN}} = -131.9\ \mathrm{kcal/mol} \qquad (2)$$

The reaction Gibbs free energies of the following reduction half reactions are calculated using the DFT-computed Gibbs free energy in MeCN solution (see Computational Details) and the Gibbs free energy of electron (−0.867 kcal/mol).[123]

$$\bullet\mathbf{NR^1R^2} + e^- \rightarrow {}^-\mathbf{NR^1R^2} \qquad \Delta G_{\text{MeCN}} = -135.8 \text{ kcal/mol} \qquad (3)$$

$$\mathbf{5\text{-}35} + e^- \rightarrow \mathbf{5\text{-}27} \qquad \Delta G_{\text{MeCN}} = -120.7 \text{ kcal/mol} \qquad (4)$$

The reaction energies of the SET reactions (eq. 5-7) can be calculated from equations 1-4.

$$\text{Ru(bpy)}_3^{2+} + \bullet\mathbf{NR^1R^2} \rightarrow \text{Ru(bpy)}_3^{3+} + {}^-\mathbf{NR^1R^2} \qquad \Delta G_{\text{MeCN}} = -3.9\text{kcal/mol} \qquad (5)$$

$$\text{Ru*(bpy)}_3^{2+} + \bullet\mathbf{NR^1R^2} \rightarrow \text{Ru(bpy)}_3^{3+} + {}^-\mathbf{NR^1R^2} \qquad \Delta G_{\text{MeCN}} = -52.3 \text{ kcal/mol} \qquad (6)$$

$$\text{Ru(bpy)}_3^{3+} + \mathbf{5\text{-}27} \rightarrow \text{Ru(bpy)}_3^{2+} + \mathbf{5\text{-}35} \qquad \Delta G_{\text{MeCN}} = -11.2 \text{ kcal/mol} \qquad (7)$$

5.2.2.3 Computational mechanistic studies for the C–H trifluoromethoxylation of arenes and heteroarenes using OCF$_3$-reagent 5-9 by means of Ru(II) photo-redox catalyst

A series of experimental studies performed by Ngai research group and computational studies were conducted to shed light on the reaction mechanism. A homolytic cleavage of the N–O bond through either photoexcited **5-9** or the anion radical of **5-9** (**5-23)** generated from the single-electron transfer (SET) between **5-9** and photo-redox catalyst were proposed by Ngai research group (**Figure 5-11**). To distinguish these two possible reaction pathways, Ngai research group performed the trifluoromethoxylation reaction using a bandpass filter (488 ± 2 nm), where the photoexcitation of the reagent **5-9** is not feasible but that of Ru(bpy)$_3$(PF6)$_2$ is possible (**Figure**

5-11a). 93% of the starting material **5-9** was recovered, which implicates that the formation of $OCF_3^•$ requires the photoexcitation of reagent **5-9**. DFT calculations showed that if the anion radical of **5-9** was formed, the mesolytic cleavage of the N–O bond favors the formation of $^•NR_1R_2$ instead of $OCF_3^•$. Thus, these collective results suggest that the formation of $OCF_3^•$ via the reduction of reagent **5-9** by excited $Ru(bpy)_3(PF_6)_2$ is unlikely.

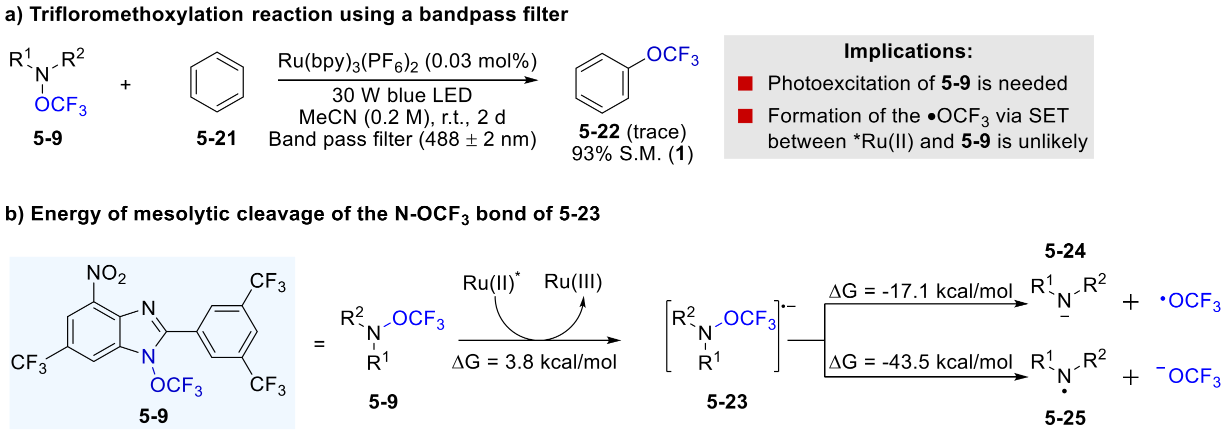

a) Trifloromethoxylation reaction using a bandpass filter

Implications:

- Photoexcitation of **5-9** is needed
- Formation of the •OCF_3 via SET between *Ru(II) and **5-9** is unlikely

b) Energy of mesolytic cleavage of the N-OCF_3 bond of 5-23

Figure 5-11. Probing the pathway for the formation of the $OCF_3^•$.

The relative reactivity of $OCF_3^•$ and $^•NR_1R_2$ towards an arene was examined next. DFT calculations showed the addition of $OCF_3^•$ to benzene is energetically more favorable than that of $^•NR_1R_2$ (**Figure 5-12a**). This result corroborates the experimental outcome where irradiation of a mixture of reagent **5-9** and 1,3,5-trichlorobenzene in the absence of a redox-active catalyst gave only the product of trifluoromethoxylation (**Figure 5-12b**). These results suggest that the redox-active catalysts will play a critical role in the final product distribution (**5-32** vs. **5-33**).

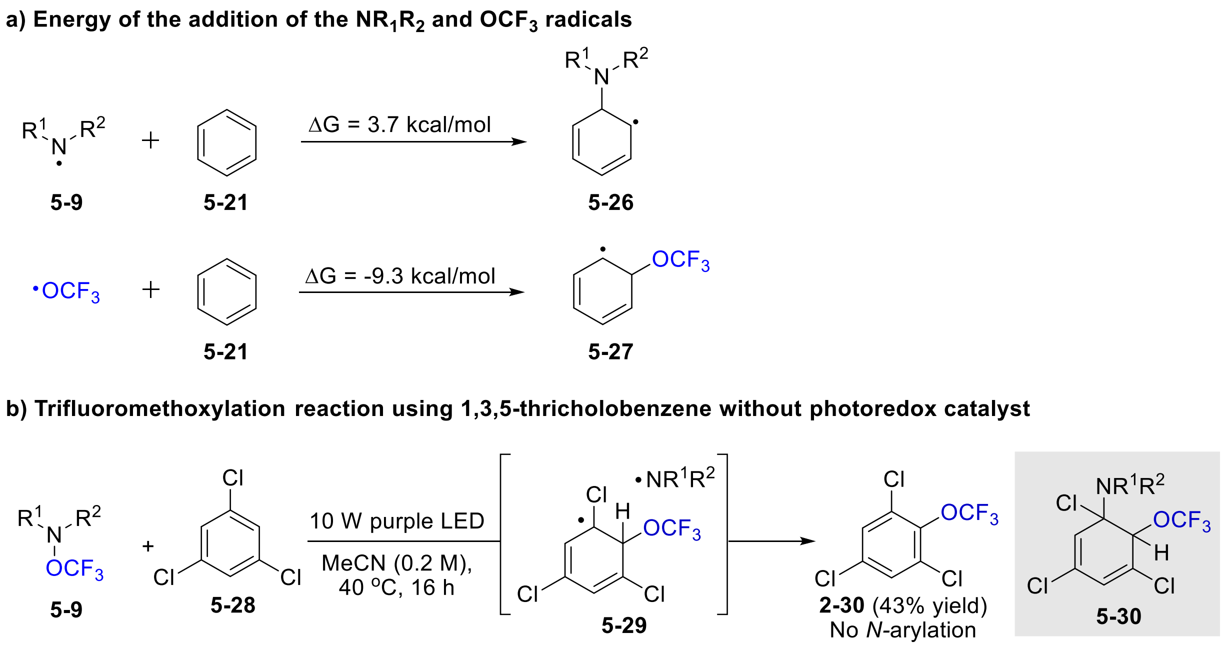
a) Energy of the addition of the NR_1R_2 and OCF_3 radicals

b) Trifluoromethoxylation reaction using 1,3,5-thricholobenzene without photoredox catalyst

Figure 5-12. Examination of the relative reactivity of the $^{\bullet}NR_1R_2$ and $OCF_3^{\bullet}$.

Experimental results from Ngai research group revealed that in the absence of a redox-active catalyst, a significant amount of N-arylation side-product (**5-33**) was obtained.[113a] It was proposed that once **5-27** and $^{\bullet}NR_1R_2$ are formed, they can undergo either hydrogen-atom abstraction to give the desired product **5-32** or the radical coupling reaction to produce cyclohexadiene **5-31**. The elimination of H-NR_1R_2 or H-OCF_3 from **5-31** would afford **5-32** or **5-33**. DFT calculations were performed to study the relative rates and thermodynamics of the base-promoted elimination from the dearomatized intermediate **5-31** to form the O- and N-arylation products (**5-32** and **5-33**). The OCF_3^{-} anion was used as a model base in the calculations. Although other bases may also promote the elimination, the relative rates between the formation of the O- and N-arylation products are not expected to be significantly affected by the base. As shown in in **Figure 5-13**, computational studies indicate that the formation of **5-33** through the elimination of H-OCF_3 is both kinetically ($\Delta\Delta G^{\ddagger}$ = -8.7 kcal/mol) and thermodynamically ($\Delta\Delta G$ = -5.3 kcal/mol, more favorable than that of H-NR_1R_2. These data indicate that once **5-31** is formed, it will be exclusively converted to N-arylation product **5-33**. Thus, the low selectivity between N- and O-arylation in the absence of a redox-active catalyst is likely due to the competing pathways of radical coupling and hydrogen-atom abstraction, which would form N- and O arylation products (**5-33** and **5-32**), respectively. However, in the presence of redox-active catalysts, the reaction favors the formation of the desired product **5-32** (**Figure 5-15**).

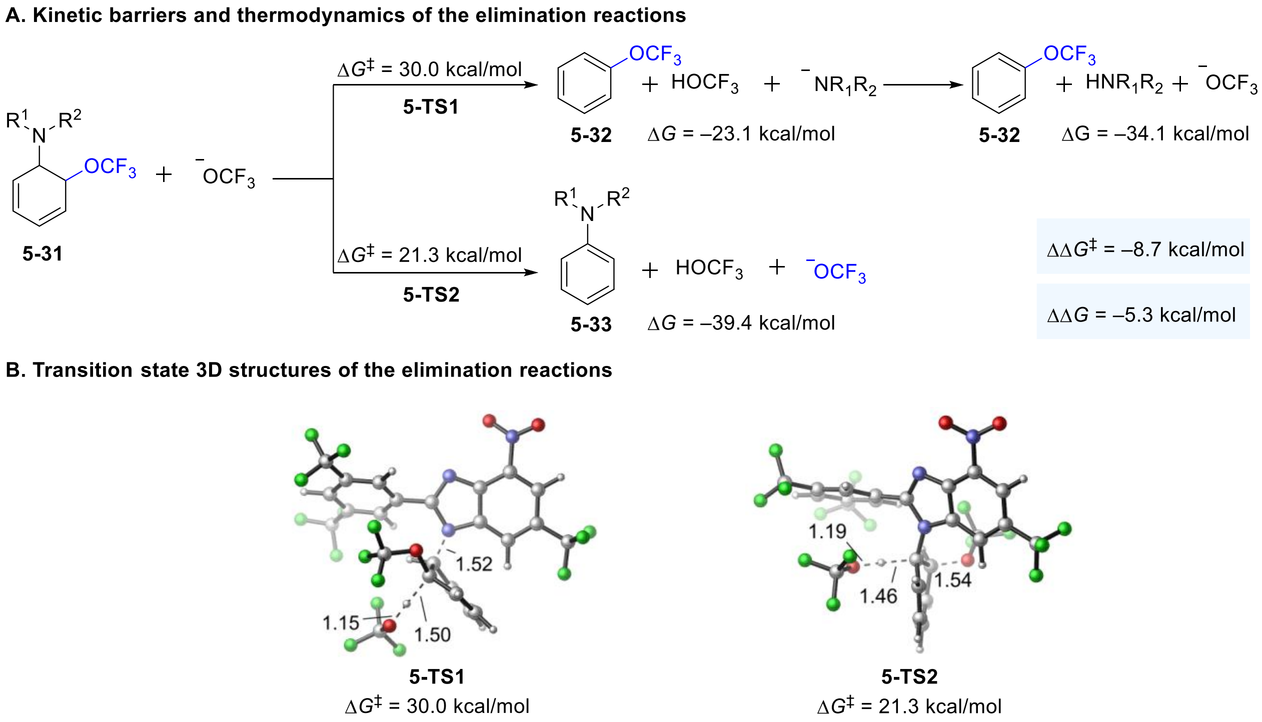
A. Kinetic barriers and thermodynamics of the elimination reactions

B. Transition state 3D structures of the elimination reactions

Figure 5-13. Kinetics and thermodynamics of the elimination reactions from the dearomatized intermediate 5-31. All energies are with respect to the separated reactants 5-31 and $OCF3^{-}$.

Presumably, redox active catalysts intervene in the reactions between $^{\bullet}NR_1R_2$ and **5-27** through SET processes. Computational data (**Figure 5-14**) demonstrate that ground-state redox-active catalysts are already effective to promote the SET processes. With the photoexcited redox-active catalyst, [Ru(bpy)$_3$(PF$_6$)$_2$*], such processes should be more efficient.[124]

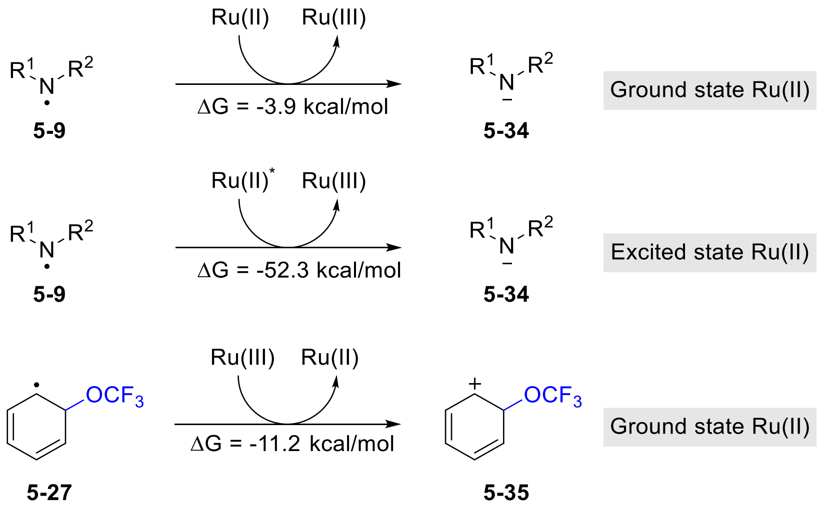

Figure 5-14. Computational studies for Ru(bpy)$_3$(PF$_6$)$_2$ mediated the SET process.

The proposed reaction mechanism based on the computational and experimental mechanistic studies are shown in Figure **5-15**. The photo-excitation of reagent **5-9** under the irradiation of violet LED light forms **5-23**, which undergoes homolytic N–O bond cleavage to generate the N-centered radical ($^{\bullet}NR_1R_2$) and the OCF$_3$ radical ($OCF_3^{\bullet}$). Once $OCF_3^{\bullet}$ is formed, it adds to an arene to afford the cyclohexadienyl radical **5-27**. Redox-active catalysts then mediate sequential single-electron transfer (SET) processes between $^{\bullet}NR_1R_2$ and **5-27** to form ionic species $^{-}NR_1R_2$ and **5-35**, respectively. Deprotonation of **5-35** restores the aromaticity and gives the desired product of trifluoromethoxylation (**5-32**).

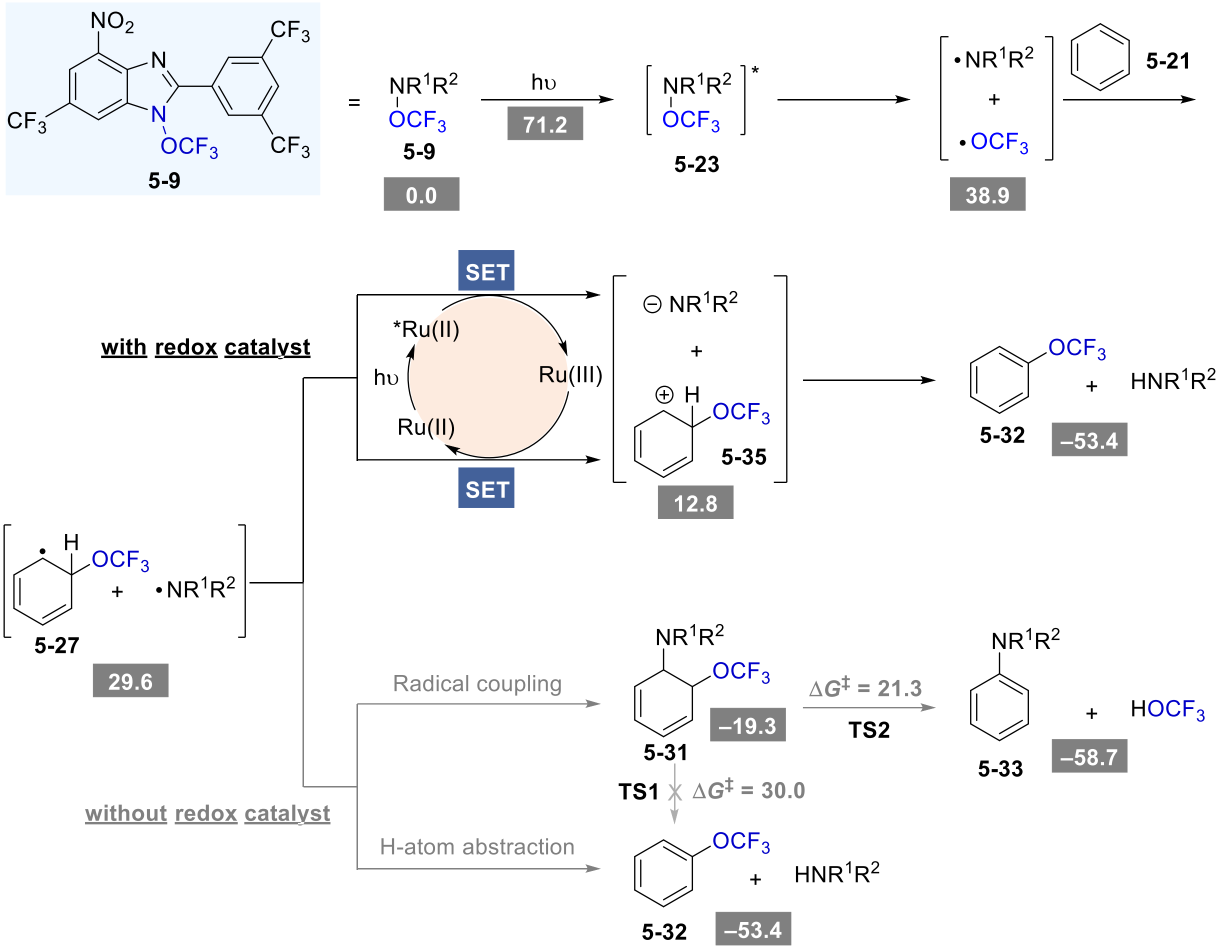

Figure 5-15. Proposed reaction mechanism for the C–H trifluoromethoxylation by OCF_3-reagent 5-9 under photo-redox conditions. Computed Gibbs free energies are in kcal/mol with respect to 5-9.

5.2.3 C–H Tri- and Difluoromethoxylation of Arenes and Heteroarenes Using OCF_3-Reagent 5-10 by Means of Ru(II) Photoredox Catalyst

Mechanistic DFT calculations described in this section were conducted in order to shed light on the reaction mechanism of C–H tri and difluoromethoxylation of arenes and heteroarenes using OCF_3- and OCF_2H-reagents (**5-10** and **5-11**) under photo-redox conditions (**Figure 5-3b** and

Figure 5-3c). Calculations were performed in order to explore the role of the photoredox catalyst and OCF_3- and OCF_2H-reagents (**5-10** and **5-11**).

5.2.3.1 Computational details

All DFT calculations were performed with the Gaussian 09 software package.[46] Geometries were optimized using the M06-2X[48] functional and the 6-31+G(d). The SMD[49] solvation model and MeCN solvent were used in the calculations. Single point energies were calculated using M06-2X and 6-311++G(d,p) and the SMD solvation model in MeCN. Reported Gibbs free energies and enthalpies in solution include thermal corrections computed at 298 K. The experimental standard reduction potential (SRP) of $Ru^*(bpy)_3^{2+}$ (−0.81 V vs. SCE in MeCN)[121] was used in the computations of the reaction Gibbs free energies of the single electron transfer (SET) processes with the photoredox catalyst (for detail explanation refer to section 5.2.2.2).

5.2.3.2 Computational mechanistic study of the C–H trifluoromethoxylation of arenes and heteroarenes using OCF_3-reagent 5-9 by means of Ru(II) photoredox catalyst

As discussed in the last section, reagent **5-9** is capable of promoting trifluoromethoxylation of arenes and heteroarenes (**Figure 5-3a**). However, the reaction is complicated by the formation of the N-arylated side product **5-III**. In an effort of selectively forming the $OCF_3^{\bullet}$, Ngai research group developed a new redox-active OCF_3-reagents that enable the first catalytic and exclusive generation of the versatile $OCF_3^{\bullet}$ for a direct aryl C−H trifluoromethoxylation of arenes and heteroarenes.[113b]

Photoredox catalysis has recently emerged as a powerful tool in organic synthesis. Ngai suggested that an appropriate combination of photoredox catalysts and 1-OCF_3-benzotriazole reagents would allow the catalytic formation of $OCF_3^{\bullet}$ through a sequential SET process. As an initial attempt they tried to use OCF_3-reagent **5-36**, but no trifluoromethoxylation product was observe.[113b] Even if the corresponding radical anion can be accessed, DFT calculations show that the mesolytic cleavage of the N−OCF3 bond would favor the formation of the N-centered benzotriazole radical **5-39** rather than that of the $OCF_3^{\bullet}$ because of the electron withdrawing group (e.g.,CF3) on the O atom (**Figure 5-16**).

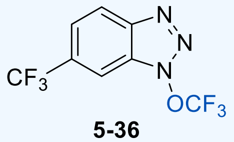

5-36

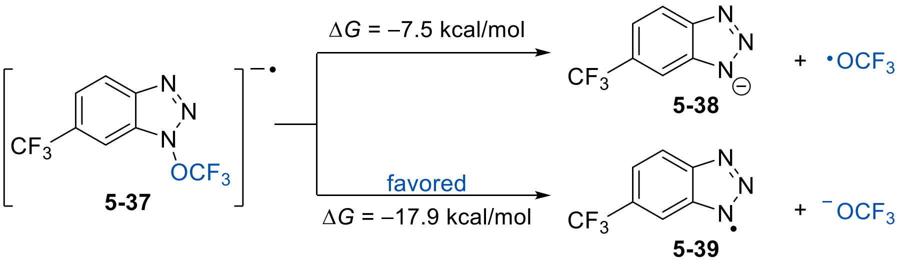

Figure 5-16. Fragmentation energies of 5-37 radical anion.

Based on the computational and experimental results, Ngai research group proposed that cationic N−OCF_3 reagents would be better electron acceptors and the resulting reduced neutral radicals generated after the SET would fragment to form the $OCF_3^{\bullet}$ selectively. OCF_3-reagent **5-10** was found to generate the trifluoromethoxylation product without the formation of any side products (**Figure 5-3b**). DFT calculations showed favorable SET between excited Ru*$(bpy)_3^{2+}$

and **5-40** to form radical **5-41** (ΔG = -20.9 kcal/mol) that readily undergoes homolytic cleavage of the N−OCF_3 bond (ΔG = -22.4 kcal/mol), thereby catalytically and exclusively forming the $OCF_3^{\bullet}$ radical (**Figure 5-17**).

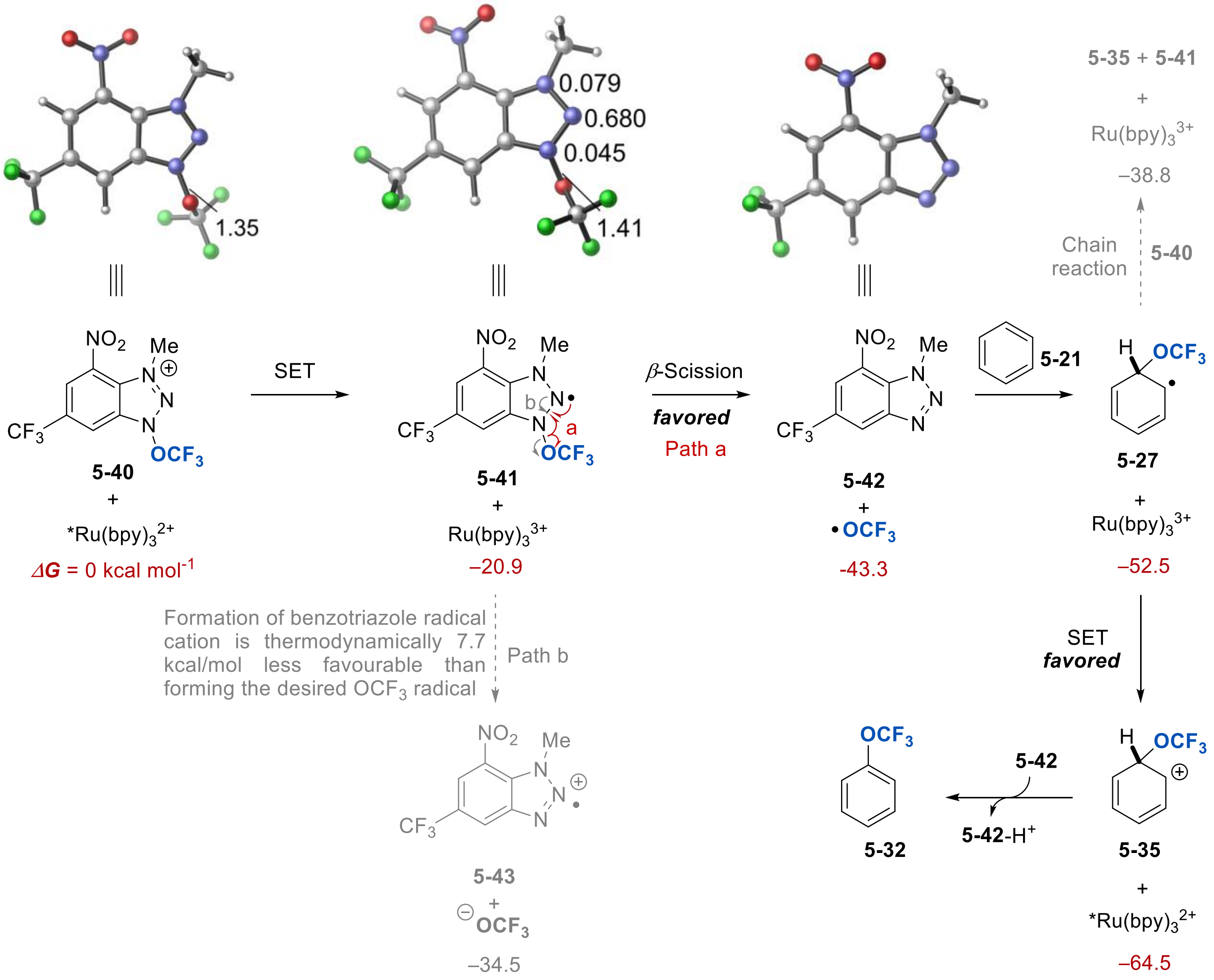

Figure 5-17. Energies of photocatalytic trifluoromethoxylation of benzene. All Gibbes free energies are in kcal/mol and are with respect to 5-40 and the photoexcited *Ru(bpy)$_3^{2+}$. The N-O bond distances in 5-40 and 5-41 are in Å. The Mulliken spin densities on the nitrgen atoms in 5-41 are provided.

After the formation of **5-41** during SET, another alternative after the N−OCF_3 cleavage is the formation of benzotriazole radical cation **5-43**. However, calculations showed that this process is 7.7 kcal/mol less favorable than forming the desired $OCF_3^{\bullet}$ (**Figure 5-17**). Once the $OCF_3^{\bullet}$ is formed it will add to **5-21** to form cyclohexadienyl radical **5-27**. This radical will be reduced by $Ru(bpy)_3^{3+}$ to form **5-35**. Deprotonation of **5-35** restores the aromaticity and gives the desired product of trifluoromethoxylation (**5-32**). Another alternative after the formation of **5-27** is a chain mechanism. However, DFT calculations shown this process is less thermodynamically favorable than the SET between $Ru(bpy)_3^{3+}$ and **5-27**. These mechanistic studies suggest a catalytic cycle (**Figure 5-18**) distinct from the previously reported photoactive OCF_3-reagent **5-9**.

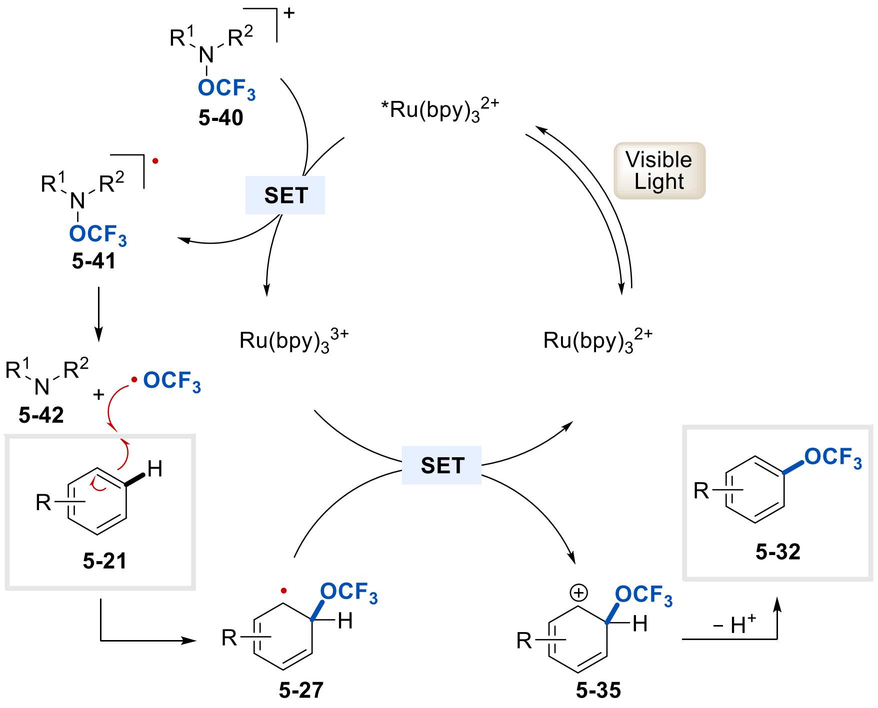

Figure 5-18. Proposed catalytic cycle for the C−H trifluoromethoxylation of arenes and heteroarenes by OCF_3-reagent 5-10 under photoredox conditions.

In addition to the generation of OCF_3-reagent **5-10**, Ngai research group developed OCF_2H-reagent **5-11** for C−H difluoromethoxylation of arenes and heteroarenes under photoredox conditions. Experimental mechanistic studies suggest the selective generation of the $OCF_2H^\bullet$. DFT calculations were performed to better understand the reactivity of the $OCF_2H^•$ and the reaction mechanism. Calculations showed favorable SET between excited Ru*(bpy)$_3^{2+}$ and **5-44** to form radical **5-45** (ΔG = -17.0 kcal/mol) that readily undergoes homolytic cleavage of the N−OCF_2H bond (ΔG = -25.4 kcal/mol), thereby catalytically and exclusively forming the $OCF_2H^•$ (**Figure 5-19**).

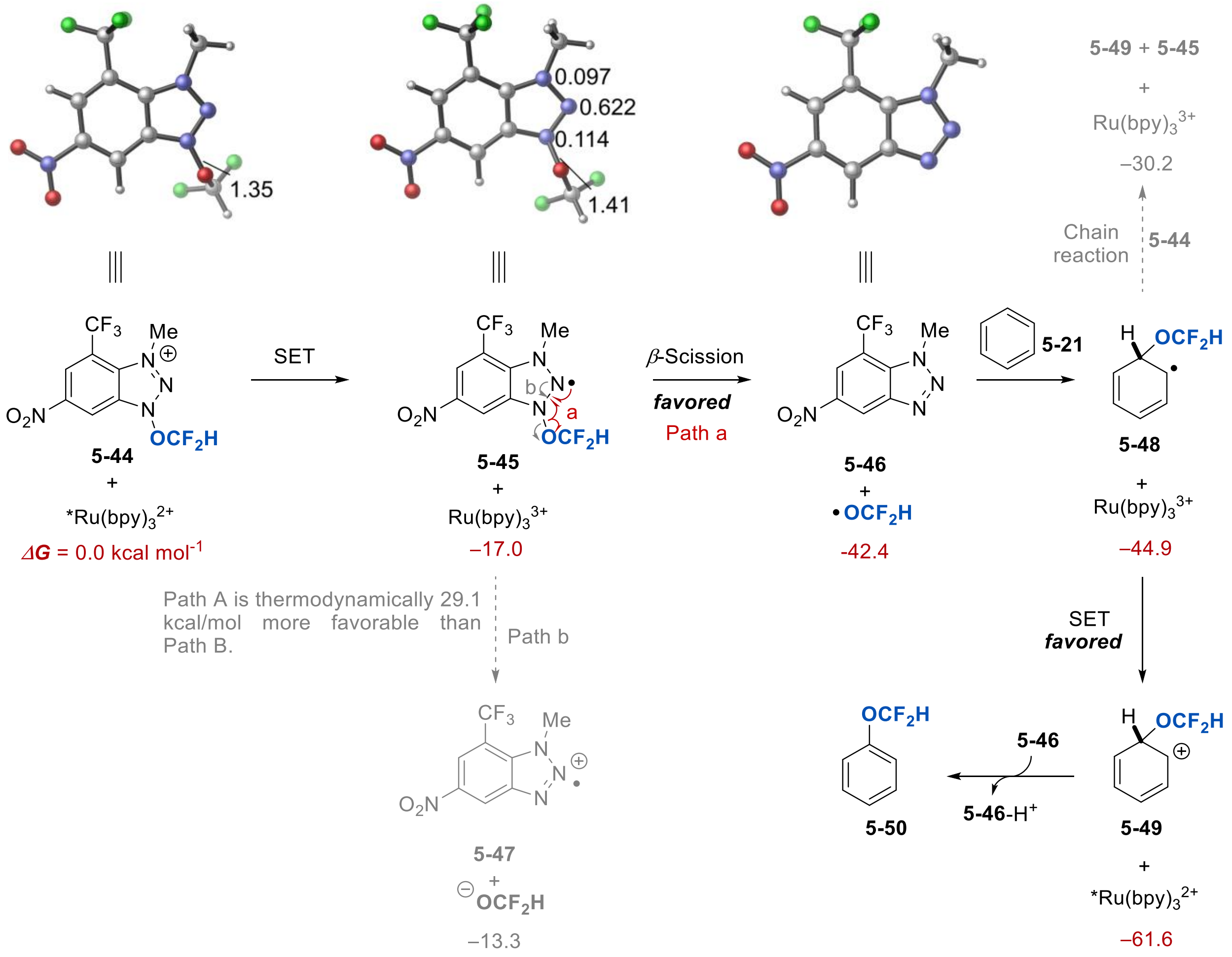

Figure 5-19. Energies of photocatalytic difluoromethoxylation of benzene. All energies are in kcal/mol and are with respect to 5-44 and *Ru(bpy)$_3^{2+}$. The N-O bond distances in 5-44 and 5-45 are in Å. The Mulliken spin densities in 5-45 are provided.

After the formation of **5-45** during SET, another alternative after the N−OCF_2H cleavage is the formation of **5-47**. However, calculations showed that path a is thermodynamically 29.1 kcal/mol more favorable than path b (**Figure 5-19**). Once the $OCF_2H^\bullet$ is formed it will add to **5-21** to form cyclohexadienyl radical **5-48**. This radical is then reduced by $Ru(bpy)_3^{3+}$ to form **5-49**. Deprotonation of **5-39** restores the aromaticity and gives the desired difluoromethoxylation product (**5-50**). Another alternative after the formation of **5-48** is a chain mechanism. However, DFT calculations show this process is less thermodynamically favorable than the SET between $Ru(bpy)_3^{3+}$ and **5-48** (Figure 5-19).

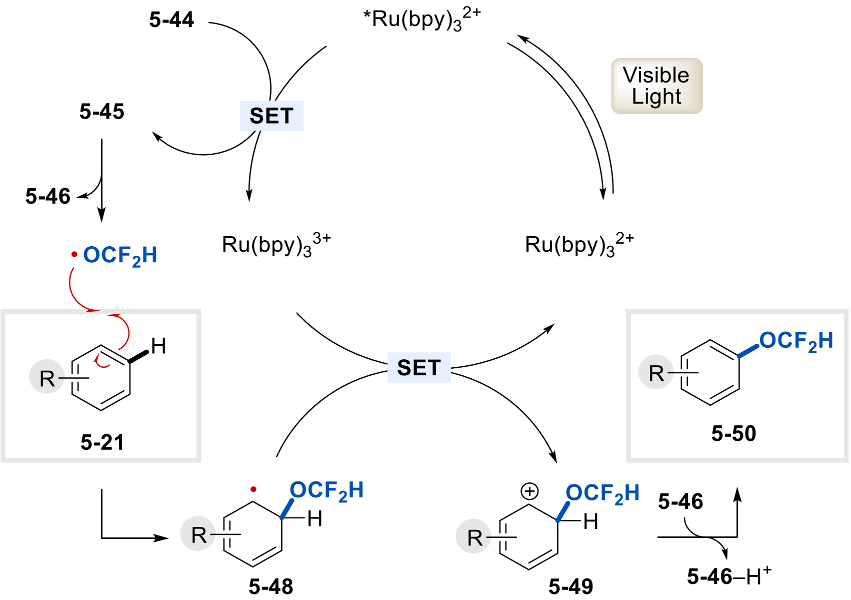

Figure 5-20. Proposed catalytic cycle for the C−H difluoromethoxylation of arenes and heteroarenes by OCF_2H-reagent 5-11 under photoredox conditions.

Based on these computational results, a catalytic cycle of this transformation was proposed as shown in **Figure 5-20**. Initial excitation of the $Ru(bpy)_3^{2+}$ photocatalyst produces the long-lived triplet-excited state of $*Ru(bpy)_3^{2+}$.**Error! Bookmark not defined.** This catalyst undergoes SET with the redox-active cationic reagent **5-44** generating $Ru(bpy)_3^{3+}$ and neutral radical **5-45** that undergoes β-scission to liberate benzotriazole (**5-46**) and the $OCF_2H^{\bullet}$. The addition of this radical to **5-21** to form cyclohexadienyl radical **5-48** is thermodynamically favourable. Oxidation of **5-48** by $Ru(bpy)_3^{3+}$ affords cyclohexadienyl cation **5-49**, which is deprotonated by benzotriazole (**5-46**) to give the desired C–H difluoromethoxylated product **5-50**.

5.3 CONCLUSION

Computations were performed to investigate the mechanism of the OCF_3-migration step in the synthesis of aryl trifluoromethyl ethers via O-trifluromethylation of *N*-aryl-*N*-hydroxylamine with the Togni reagent. The calculations indicated the OCF_3-migration occurs via a stepwise mechanism involving heterolytic N–OCF_3 bond cleavage and rapid C–O bond formation to form a dearomatized intermediate, which then undergoes rearomatization to form the *ortho*-trifluoromethoxylation product. The reaction with electron-deficient substrate requires higher activation energy, due to the destabilization of the zwitterionic intermediate. This agrees with the experimental Hammett plot obtained by the Ngai research group.

DFT calculations were performed to study the mechanism of C–H trifluoromethoxylation by OCF_3-raegent **5-9** under photoredox conditions. Mechanistic studies showed that 1) photoexcitation of reagent **5-9** forms $OCF_3^{\bullet}$ and 2) redox-active catalysts intervene in the radical coupling reaction of **5-27** and $^{\bullet}NR_1R_2$ to favor the formation of the desired product of trifluoromethoxylation. In the case of C–H tri- and difluoromethoxylation by OCF_3-reagent **5-10** and OCF_2H-reagent **5-11**, calculations showed that after SET, $OCF_3^{\bullet}$ and $OCF_2H^{\bullet}$ radicals are selectively generated. This allows the formation of the desired tri- and difluoromethoxylation products with minimal generation of any side product.

BIBLIOGRAPHY

[1] Wencel-Delord, J.; Glorius F. *Nat. Chem.* **2013**, *5*, 369-375

[2] Luo, C.; Gandeepan, P.; Wu, Y.; Tsai C.; Cheng, C. *ACS Catal.* **2015**, *5*, 4837-4841.

[3] Engelin, C.; Jensen, T.; Rodriguez-Rodriguez S.; Fristrup P. *ACS Catal.* **2013**, *3*, 294-302.

[4] Légaré, M. A.; Courtemanche, M. A.; Rochette, É.; Fontaine, F. G. *Science* **2015**, *349*, 513-516.

[5] Brueckl, T.; Baxter, R. D.; Ishihara, Y.; Baran, P. S. Acc. Chem. Res. **2012**, *45*, 826.

[6] Newhouse T.; Baran P. S. *Angew. Chem. Int. Ed*. **2011**, *50*, 3362-3374.

[7] Yuan C.; Liang Y.; Hernandez T.; Berriocha A.; Houk K. N.; Siegel D. *Nature*, **2013**, *499*, 192-196.

[8] Murray, R. W.; Jeyaraman, R. *J. Org. Chem.* **1985**, *50*, 2847.

[9] Mello, R.; Fiorentino, M.; Sciacovelli, O.; Curci, R. *J. Org. Chem.* **1988**, *53*, 3890.

[10] Curci, R.; D'Accolti, L.; Fusco, C. Acc. Chem. Res. **2006**, *39*, 1.

[11] (a) Zou L.; Paton R. S.; Eschenmoser A.; Newhouse T. R.; Baran P. S.; Houk K. N. *J. Org. Chem*. **2013**, *78*, 4037-4048; (b) Cleary, S. E.; Li, X.; Yang, Li. C.; Houk, K. N., Hong, X.; Brewer, M. *J. Am. Chem. Soc.*, **2019**, *141*, 3558-3565.

[12] (a) Tu, W.; Liu, L.; Floreacing, P. *Angew. Chem. Int. Ed.* **2008**, *47*, 4184-4187. (b) Clausen, D. C.; Floreancig, P. E. *J. Org. Chem.* **2012**, *77*, 6574-6582. (c) Jung, H. H.; Floreancig, P. *Tetrahedron* **2009**, *65*, 10830-10836.

[13] Li Y.; Hari D. P.; Vita M. V.; Waser J. *Angew. Chem. Int.* **2016**, *55*, 4436-4454.

[14] For pioneering work on azidation with hypervalent iodine reagents: (a) Magnus, P.; Lacour, J.; Weber, W.; *J. Am. Chem. Soc.*, **1993**, *115*, 9347; (b) Kita, Y.; Tohma, H.; Takada, T.; Mitoh, S.; Fujita, S.; Gyoten, M. *Synlett*, **1994**, 427.

[15] For selected examples on radical aliphatic C–H functionalization with hypervalent iodine(III) reagents: (a) Ochiai, M.; Miyamoto, K; Kaneaki, T.; Hayashi, S.; Nakanishi, W.; *Science*, **2011**, *332*, 448; (b) Maruoka, K. *Angew. Chem., Int. Ed.*, **2013**, *52*, 8657; (c) A. P. Antonchick, A. P.; Burgmann, L.; *Angew. Chem., Int. Ed.*, **2013**, *52*, 3267; (d) Zhao, Y.; Yim, W. L.; Tan, C. K.; Yeung, Y.-Y. *Org. Lett.*, **2011**, *13*, 4308; (e) Kita, Y. *ChemCatChem*, **2014**, *6*, 76.

[16] For selected reviews on hypervalent iodine chemistry: (a) Zhdankin, V. V.; Stang, P. *Chem. Rev.*, **2002**, *102*, 2523; (b) Tohma, H.; Kita, Y.; *Adv. Synth. Catal.*, **2004**, *346*, 111; (c) Narayan, R.; Manna, S.; Antonchick, A. P. *Synlett*, **2015**, *26*, 1785.

[17] Sharma, A.; Hartwig, J. F. *Nature*, **2015**, *517*, 600.

[18] Wang Y.; Li G. X.; Yang G.; He G.; Chen G. *Chem. Sci.,* **2016**, *7*,2679-2683.

[19] Minisci, F.; Vismara, E.; Fontana, F. *Heterocycles*, **1989**, *28*, 489; (b) Duncton, M. A. J. *Med. Chem. Commun.*, **2011**, *2*, 1135.

[20] Li G.; Morales-Rivera C. A.; Wang Y.; Gao F.; He G.; Liu P.; Chen G. *Chem. Sci.*, **2016**.

[21] (a) Schultz, N.; Zhao, Y.; Truhlar, D. G. *J. Phys. Chem.* A **2005**, *109*, 4388–4403. (b) Schultz, N.; Zhao, Y.; Truhlar, D. G. *J. Phys. Chem.* A **2005**, *109*, 11127–11143. (c) Harvey, J. N. On the accuracy of DFT in transition metal chemistry. Annu. Rep. Prog. Chem. Sect. C **2006**, *102*, 203–226.

[22] Zhao, Y.; González-García, N.; Truhlar, D. G. *J. Phys. Chem. A* **2005**, *109*, 2012–2018.

[23] Valero, R.; Costa, R.; de P R Moreira, I. Thrular, D. G. *J. Chem. Phys.,* **2008**, *128*.

[24] Perdew, J. P.; Schmidt, K., AIP Conf. Proc. 577, 1 ,**2001**.

[25] Zhao, Y.; Truhlar, D. G. *Acc. Chem. Res.* **2008**, *41*, 157-167.

[26] Marenich, A.V.; Cramer, C. J.; Truhlar, D. G. J. Phys. Chem. B **2009**, 113, 6378-6396.

[27] For recent reviews on functionalization of aliphatic carbon−hydrogen bonds, see: (a) Liu, L.; Floreancig, P. E. *Curr. Opin. Drug Discovery Dev.* **2010**, *13*, 733. (b) Gutekunst, W. R.; Baran, P. S. *Chem. Soc. Rev.* **2011**, *40*, 1976. (c) Davies, H. M. L. *Angew. Chem., Int. Ed.* **2006**, *45*, 6422. (d) Li, C.-J. *Acc. Chem. Res.* **2009**, *42*, 335. (e) Robertson, J.; Pillai, J.; Lush, R. K. *Chem. Soc. Rev.* **2001**, *30*, 94.

[28] (a) Walker, D.; Hiebert, J. D. *Chem. Rev.* **1967**, *67*, 153. (b) Buckle, D. R. In *Encyclopedia of Reagents for Organic Synthesis*; Paquette, L. A., Ed.; John Wiley & Sons: Chichester, UK, **1995**; Vol. 3, p 1699. (c) Wendlandt, A. E.; Stahl, S. S. *Angew. Chem. Int. Ed.* **2015**, *54*, 14638.

[29] (a) Tu, W.; Liu, L.; Floreancig, P. E. *Angew. Chem., Int. Ed.* **2008**, *47*, 4184. (b) Liu, L.; Floreancig, P. E. *Org. Lett.* **2009**, *11*, 3152. (c) Liu, L.; Floreancig, P. E. *Angew. Chem., Int. Ed.* **2010**, *49*, 3069. (d) Liu, L.; Floreancig, P. E. *Angew. Chem., Int. Ed.* **2010**, *49*, 5894. (e) Brizgys, G. J.; Jung, H. H.; Floreancig, P. E. *Chem. Sci.* **2012**, *2*, 438. (f) Cui, Y.; Floreancig, P. E. *Org. Lett.* **2012**, *14*, 1720. (g) Clausen, D. C.; Floreancig, P. E. *J. Org. Chem.* **2012**, *77*, 6574.

[30] (a) Hayashi, Y.; Mukaiyama, T. *Chem. Lett.* **1987**, *16*, 1811. (b) Zhang, Y.; Li, C.-J. *Angew. Chem., Int. Ed.* **2006**, *45*, 1949. (c) Zhang, Y.; Li, C.-J. *J. Am. Chem. Soc.* **2006**, *128*, 4242.

(d) Benfatti, F.; Capdevila, M. G.; Zoli, L.; Benedetto, E.; Cozzi, P. G. *Chem. Commun.* **2009**, 5919. (e) Yu, B.; Jiang, T.; Su, Y.; Pan, X.; She, X. *Org. Lett.* **2009**, *11*, 3442. (f) Tsang, A. S.-K.; Jensen, P.; Hook, J. M.; Hashmi, A. S. K.; Todd, M. H. *Pure Appl. Chem.* **2011**, *83*, 655. (g) Hayashi, Y.; Itoh, T.; Ishikawa, H. Angew. Chem., Int. Ed. 2011, *50*, 3920. (h) Park, S. J.; Price, J. R.; Todd, M. H. *J. Org. Chem.* **2012**, *77*, 949. (i) Reddy, B. V. S.; Borkar, P.; Yadav, J. S.; Reddy, P. P.; Kunwar, A. C.; Sridhar, B.; Gree, R. *Org. Biomol. Chem.* **2012**, *10*, 1349. (j) Meng, Z.; Sun, S.; Yuan, H.; Lou, H.; Liu, L. *Angew. Chem., Int. Ed.* **2014**, *53*, 543. (k) Grenning, A. J.;Snyder, J. K.; Porco, J. A., Jr. *Org. Lett.* **2014**, *16*, 792. (l) Wang, H.; Zhao, Y.-L.; Li, L.; Liu, Q. *Adv. Synth. Catal.* **2014**, *356*, 3157. (m) Cheng, D.; Wu, L.; Lv, H.; Xu, X.; Yan, J. *J. Org. Chem.* **2017**, *82*, 1610. (n) Fradette, R. J.; Kang, M.; West, F. G. *Angew. Chem., Int. Ed.* **2017**, *56*, 6335.

[31] (a) Cardillo, C.; Cricchio, R.; Merlin, L., *Tetrahedron* **1971**, *27*, 1875. (b) Fu, L.; Yao, C.-J.; Chang, N.-J.; Chen, J.-R.; Lu, J.-R.; Xiao, W.-J. *Org. Biomol. Chem.* **2012**, *10*, 506. (c) Yi, H.; Liu, Q.; Liu, J.; Zeng, Z.; Yang, Y.; Lei, A. *ChemSusChem* **2012**, *5*, 2143. (d) Lemercier, B. C.; Pierce, J. G. *Org. Lett.* **2015**, *17*, 4542.

[32] (a) Xu, Y.-C.; Kohlman, D. T.; Liang S. X.; Erikkson C. *Org. Lett.* **1999**, *1*, 1599. (b) Tu, W.; Floreancig, P. E. *Angew. Chem., Int. Ed.* **2009**, *48*, 4567. (c) Ghosh, A. K.; Cheng, X. *Org. Lett.* **2011**, *13*, 4108. (d) Son, Y. W.; Kwon, T. H.; Lee, J. K.; Rae, A. N.;Lee, J. Y.; Cho, Y. S.; Min, S.-J. *Org. Lett.* **2011**, *13*, 6500. (e) Peh, G. R.; Floreancig, P. E. *Org. Lett.* **2012**, *14*, 5614. (f) Han, X.; Floreancig, P. E. *Angew. Chem., Int. Ed.* **2014**, *53*, 11075. (g) Lu, Z.; Yang, M.; Chen, P.; Xiong, X.; Li, A. *Angew. Chem., Int. Ed.* **2014**, *53*, 13840. (h) Jiao, Z.-W.; Tu, Y.-Q.; Zhang,

Q.; Liu, W.-X.; Wang, S.-H.; Wang, M. *Org. Chem. Front.* **2015**, *2*, 913. (i) Hubert, J. G.; Furkert, D. P.; Brimble, M. A. *J. Org. Chem.* **2015**, *80*, 2715. (j) Jiao, Z.-W.; Tu, Y.-Q.; Zhang, Q.; Liu, W.-X.; Zhang, S.-Y.; Wang, S.-H. Zhang, F.-M.; Jiang, S. *Nat. Commun.* **2015**, *6*, 7332. (k) Kim, H.; Lee, D. *Synlett* **2015**, *26*, 2583.

[33] Liu, L. Synthesis of Structurally and Stereochemically Diverse Tetrahydropyran Structures via DDQ-Mediated Oxidative Carbon–Hydrogen Bond Activation. Ph.D. Thesis, the University of Pittsburgh, March 2011.

[34] Shehap, O.R; Mansour, A. M. *J. Mol. Struct.* **2013**, *1047*, 121.

[35] Turek, A. K.; Hardee, D. J.; Ullman, A. M.; Nocera, D. G.; Jacobsen, E. N. *Angew. Chem. Int. Ed.* **2016**, *55*, 539.

[36] (a) The reductive potential of DDQ is 0.50 V vs SCE in MeCN. Scribner, R. M. *J. Org. Chem.* **1966**, *31*, 3671. (b) The oxidation potentials of benzylic and allylic ethers are typically within 1.4~2.2 V vs SCE. See SI for oxidation potentials of various benzylic and allylic ethers calculated using DFT. (c) Roth, H. G.; Romero, N. A.; Nicewicz, D. A. *Synlett* **2016**, *27*, 714.

[37] (a) Höfler, C.; Rüchardt, C. *Liebigs Ann.* **1996**, 183. (b) Rüchardt, C.; Gerst, M.; Ebenhoch, J. *Angew. Chem. Int. Ed. Engl.* **1997**, *36*, 1406. (c) Wurche, F.; Sicking, W.; Sustmann, R.; Klärner, F.-G.; Rüchardt, C. *Chem. Eur. J.* **2004**, *10*, 2707.

[38] Pratt, D. A.; Wright, J. S.; Ingold, K. U. *J. Am. Chem. Soc.* **1999**, *121*, 4877.

[39] Jung, H. H.; Floreancig, P. E. *Tetrahedron* **2009**, *65*, 10830.

[40] (a) Braude, E. A.; Jackman, L. M.; Linstead, R. P. *J. Chem. Soc.* **1954**, 3548. (b) Braude, E. A.; Jackman, L. M.; Linstead, R. P. *J. Chem. Soc.* **1954**, 3564.

[41] Guo, X.; Zipse, H.; Mayr, H. *J. Am. Chem. Soc.*, **2014**, *136*, 13863.

[42] Chan, B.; Radom, L. *J. Phys. Chem. A* **2007**, *111*, 6456.

[43] (a) Luca, O. R.; Wang, T.; Konezny, S. J.; Batista, V. S.; Crabtree, R. H. *New J. Chem.*, **2011**, *35*, 998. (b) Batista, V. S.; Crabtree, R. H.; Konezny, S. J.; Luca, O. R.; Praetorius, J. M. *New J. Chem.*, **2012**, *36*, 1141.

[44] Yamabe, S.; Yamazaki, S.; Sakaki, S. *Int. J. Quantum Chem.*, **2015**, *115*, 1533-1542.

[45] (a) Würthwein, E. U.; Lang, G.; Schappele, L. H.; Mayr, H. *J. Am. Chem. Soc.*, **2002**, *124*, 4084. (b) Shi, J.; Huang, X. Y.; Wang, H. J.; Fu, Y. *J. Chem. Inf. Model.*, **2012**, 52, 63.

[46] Frisch, M. J.; Trucks, G. W.; Schlegel, H. B.; Scuseria, G. E.; Robb, M. A.; Cheeseman, J. R.; Scalmani, G.; Barone, V.; Mennucci, B.; Petersson, G. A.; Nakatsuji, H.; Caricato, M.; Li, X.; Hratchian, H. P.; Izmaylov, A. F.; Bloino, J.; Zheng, G.; Sonnenberg, J. L.; Hada, M.; Ehara, M.; Toyota, K.; Fukuda, R.; Hasegawa, J.; Ishida, M.; Nakajima, T.; Honda, Y.; Kitao, O.; Nakai, H.; Vreven, T.; Montgomery, J. A., Jr.; Peralta, J. E.; Ogliaro, F.; Bearpark, M.; Heyd, J. J.; Brothers, E.; Kudin, K. N.; Staroverov, V. N.; Kobayashi, R.; Normand, J.; Raghavachari, K.; Rendell, A.; Burant, J. C.; Iyengar, S. S.; Tomasi, J.; Cossi, M.; Rega, N.; Millam, N. J.; Klene, M.; Knox, J. E.; Cross, J. B.; Bakken, V.; Adamo, C.; Jaramillo, J.; Gomperts, R.; Stratmann, R. E.; Yazyev, O.; Austin, A. J.; Cammi, R.; Pomelli, C.; Ochterski, J. W.; Martin, R. L.; Morokuma, K.; Zakrzewski, V. G.; Voth, G. A.; Salvador, P.; Dannenberg, J. J.; Dapprich, S.; Daniels, A. D.; Farkas, Ö.; Foresman, J. B.; Ortiz, J. V.; Cioslowski, J.; Fox, D. J. Gaussian 09, Revision D.01; Gaussian, Inc.: Wallingford, CT, **2009**.

[47] CYLview, 1.0b; Legault, C. Y. Universitéde Sherbrooke: Quebec, Canada, (2009); http://www.cylview.org

[48] Zhao, Y.; Truhlar, D. G. *Theor. Chem. Acc.* **2008**, *120*, 215.

[49] Marenich, A. V.; Cramer, C. J.; Truhlar, D. G. *J. Phys. Chem. B*, **2009**, *113*, 6378.

[50] Marcus, R. A. *J. Chem. Phys.* **1956**, *24*, 966.

[51] (a) Winget, P.; Cramer, C. J.; Truhlar, D. G. *Theor. Chem. Acc.*, **2004**, *112*, 217. (b) Isse, A. A.; Lin, C. Y.; Coote, M. L.; Gennaro, A. *J. Phys. Chem. B*, **2011**, *115*, 678. (c) Huynh, M. T.; Anson, C. W.; Cavell, A. C.; Stahl, S. S.; Hammes-Schiffer, S. *J. Am. Chem. Soc.* **2016**, *138*, 15903.

[52] These results are in accord with previous computational studies from Chan and Radom (ref. 16), which suggested the closed-shell ionic pathway is favored in polar solvents.

[53] (a) Marcus, R. A. *J. Chem. Phys.* **1956**, *24*, 966−978. (b) Pause, L.; Robert, M.; Saveant, J.-M. *J. Am. Chem. Soc.* **2000**, *122*, 9829−9835. (c) Saveant, J. M. *J. Am. Chem. Soc.* **1987**, *109*, 6788−6795. (d) Saveant, J. M. *J. Am. Chem. Soc.* **1992**, *114*, 10595−10602.

[54] (a) Wu, Y. D.; Tucker, J. A.; Houk, K. N. *J. Am. Chem. Soc.* **1991**, *113*, 5018. (b) Paddonrow, M. N.; Wu, Y. D.; Houk, K. N. *J. Am. Chem. Soc.* **1992**, *114*, 10638. (c) Liu, P.; Yang, X.; Birman, V. B.; Houk, K. N. *Org. Lett.*, **2012**, *14*, 3288.

[55] (a) Hoffmann, R.; Woodward, R. B. *J. Am. Chem. Soc.* **1965**, *87*, 4388. (b) Levandowski, B. J.; Houk, K. N. *J. Am. Chem. Soc.* **2016**, *138*, 16731.

[56] (a) Bickelhaupt, F. M.; Houk, K. N. *Angew. Chem. Int. Ed.* **2017**, *56*, 10070. (b) Ess, D. H.; Houk, K. N. *J. Am. Chem. Soc.* **2008**, *130*, 10187.

[57] The interaction energy it is define by the fallowing ecuation:

$\Delta E_{int} = E_{TS} - E_{SUB(TS)} - E_{DDQ(TS)}$.

[58] The C-attack transition states have greater interaction energies than the O-attack transition states because the more endothermic C-attack pathway has later transition states, as evidenced by the longer C−H distances in **2-TS9** and **2-TS10** compared to those in **2-TS7** and **2-TS8**.

[59] The through-bond interaction energies in **2-TS7** and **2-TS8** are expected to be similar due to the similar forming O−H distances in these transition states. Similarly, the through-bond interactions in the forming C−H bond in **2-TS9** and **2-TS10** are also expected to be similar.

[60] The importance of contact between the DDQ and the alkene moiety is consistent with the lower reactivity of vinylsilanes (ref. 3c), which are more sterically congested to achieve the stacked geometry for the electrostatic attractions.

[61] Sigman, M. S.; Harper, K. C.; Bess, E. N.; Milo, A. *Acc. Chem. Res.*, **2016**, *49*, 1292.

[62] For an example of using redox potentials as parameters for linear free energy relationship: Sevov, C. S.; Hickey, D. P.; Cook, M. E.; Robinson, S. G.; Barnett, S.; Minteer, S. D.; Sigman, M. S.; Sanford, M. S. *J. Am. Chem. Soc.* **2017**, *139*, 1452.

36 (a) Guo, X.; Mayr, H. *J. Am. Chem. Soc.* **2013**, *135*, 12377. (b) Ryu, I.; Murai, S.; Hatayama, Y.; Sonoda, N. Tetrahedron Lett. **1978**, *19*, 3455 (c) Bhattacharya, A.; DiMichele, L. M.; Dolling, U.-H.; Grabowski, E. J. J.; Grenda, V. J. *J. Org. Chem.* **1989**, *54*, 6118. (d) Hodgson, D. M.; Moreno-Clavijo, E.; Day, S. E.; Man, S. *Org. Biomol. Chem.* **2013**, *11*, 5362.

[63] (a) Guo, X.; Mayr, H. *J. Am. Chem. Soc.* **2013**, *135*, 12377. (b) Ryu, I.; Murai, S.; Hatayama, Y.; Sonoda, N. Tetrahedron Lett. **1978**, *19*, 3455 (c) Bhattacharya, A.; DiMichele, L. M.; Dolling, U.-H.; Grabowski, E. J. J.; Grenda, V. J. *J. Org. Chem.* **1989**, *54*, 6118. (d) Hodgson, D. M.; Moreno-Clavijo, E.; Day, S. E.; Man, S. *Org. Biomol. Chem.* **2013**, *11*, 5362.

[64] (a) Bartmess, J. E. *J. Phys. Chem.* **1994**, *98*, 6420−6424. (b) Bartmess, J. E. *J. Phys. Chem.* **1995**, *99*, 6755−6755.

[65] Isse, A. A.; Gennaro, A. *J. Phys. Chem. B* **2010**, *114*, 7894−7899.

[66] Diggle, J. W.; Parker, A. J. *Aust. J. Chem.* **1974**, *27*, 1617−1621.

[67] Wencel-Delord, J.; Glorius F., *Nat. Chem.* **2013**, *5*, 369-375.

[68] Légaré, M. A.; Courtemanche, M. A.; Rochette, É., Fontaine, F. G., *Science* **2015**, *349*, 513-516.

[69] a)Wang, Y.; Li, G. X.; Yang, G.; He, G.; Chen, G., *Chem. Sci.*, **2016**, *7*, 2679-2683; b) Sharma, A.; Hartwig, *Nature*, **2015**, *517*, 600-604; c) Zhandankin, V. V.; Krasutsky, A. P.; Kuehl, C. J.; Simonsen, A. J.; Woodward, J. K.; Mismash, B.; Bolz, J. T., *J. Am. Chem. Soc.*, **1996**, *118*, 5192.

[70] Li, G. X.; Morales-Rivera, C. A.; Gao, F.; Wang, Y.; He, G.; Liu, P.; Chen, G., *Chem. Sci.*, **2017**, *8*, 7180-7185.

[71] Li, G. X.; Hu, H.; He, G.; Chen, G., *ACS. Catal.*, **2018**, *8*, 11847-11853.

[72] a) Zhdankin, V. V.; Stang, P. J. *Chem. Rev.* **2002**, *102*, 2523; b) Zhdankin, V. V.; Stang, P. J. *Chem. Rev.* **2008**, *108*, 5299; c) Zhdankin, V. V., Hypervalent Iodine Chemistry: Preparation, Structure, and Synthetic Applications of Polyvalent Iodine Compounds, Wiley, New York, 2014;

d) Wirth, T.; Hypervalent iodine chemistry: modern developments in organic synthesis, Vol. 224, Springer, New York, 2003; e) Wirth, T. *Angew. Chem. Int. Ed.* **2005**, *44*, 3656; *Angew. Chem.* **2005**, *117,* 3722; f) Dohi, T.; Kita, Y. *Chem. Commun.* **2009**, 2073; g) Merritt, E. A.; Olofsson, B. *Angew. Chem. Int. Ed.* **2009**, *48*, 9052; *Angew. Chem.* **2009**, 121, 9214; h) Merritt, E. A.; Olofsson, B. *Synthesis* **2011**, 517

[73] (a) Zhdankin, V. V.; Krasutsky, A. P.; Kuehl, C. J.; Simonsen, A. J.; Woodward, J. K.; Mismash, B.; Bolz, J. T., *J. Am. Chem. Soc.*, **1996**, *118*, 5192; (b) Ochiai, M.; Ito, T.; Takahashi, H.; Nakanishi, A.; Toyonari, M.; Sueda, T.; Goto, S.; Shiro, M., *J. Am. Chem. Soc.*, **1996**, *118*, 7716; (c) Le Vaillant, F.; Courant, T.; Waser, J., *Angew. Chem., Int. Ed.*, **2015**, *54,* 11200; (d) Jia, K.; Zhang, F.; Huang, H.; Chen, Y., *J. Am. Chem. Soc.*, **2016**, *138*, 1514.

[74] Hand book of Chemistry and Physics. 90th edition, David R. Lide, CRC Press, **2009-2010**.

[75] Ribeiro, R. F.; Marenich, A. V.; Cramer, C. J.; Truhlar, D. G. *J. Phys. Chem. B*, **2011**, *115*, 14556-14562.

[76] Yang, J. D.; Li, M.; Xue, X. S., *Chin. J. Chem.* **2019**, 37, 10.1002/cjoc.201800549.

[77] Wang, L.; Liu, J., *Eur. J. Org. Chem.* **2016**, 1813-1824.

[78] Wang, Z.; Herraiz, A. G.; del Hoyo, A. M.; Suero, M. G., *Nature* **2018**, *554*, 86-91.

[79] Rabet, P.; Fumagalli, G.; Boyd, S.; Greaney, M., *Org. Lett.* **2016**, *18*, 1646-1649.

[80] (a) Topics in Heterocyclic Chemistry, Vol. 11 – Bioactive Heterocycles V, (Ed.: R. R. Gupta), Springer Verlag, New York, **2008**. (b) Welsch, M. E.; Snyder, S. A.; Stockwell, B. R. *Curr. Opin. Chem. Biol.* **2010**, *14*, 347.

[81] (a) Seregin, I. V.; Gevorgyan, V.; *Chem. Soc. Rev.* **2007**, *36*, 1173; (b) Ackermann, L.; Vicente, R.; Kapdi, A. R. *Angew. Chem., Int. Ed.* **2009**, *48*, 9792; (c) Bruckl, T.; Baxter, R. D.; Ishihara, R. Y.; Baran, P. S. *Acc. Chem. Res.* **2012**, *45*, 826. (d) Wencel-Delord, J.; Glorius, F.; *Nature Chem.* **2013**, *5*, 369.

[82] For selected reviews and examples on C–H alkylation of *N*-heteroarenes: (a) Ackermann, L. *Chem. Commun.* **2010**, *46*, 4866. (b) Lewis, J. C.; Bergman, R. G.; Ellman, J. A. *J. Am. Chem. Soc.* **2007**, *129*, 5332. (c) Nagib, D. A.; MacMillan, D. W. C. *Nature* **2011**, *480*, 224. (d) Schonherr, H.; Cernak, T. *Angew. Chem. Int. Ed.* **2013**, *52*, 11256. (e) Xiao, B.; Liu, Z.-J.; Liu, L.; Fu. Y. *J. Am. Chem. Soc.* **2013**, *135*, 616. (f) Schramm, Y.; Takeuchi, M.; Semba, K.; Nakao, Y.; Hartwig, J. F. *J. Am. Chem. Soc.* **2015**, *137*, 12215. (g) Bering, L.; Antonchick, A. P *Org. Lett.* **2015**, *17*, 3134.

[83] (a) Minisci, F.; Vismara, E.; Fontana, F.; *Heterocycles*, **1989**, *28*, 489. (b)Duncton, M. A. J. *Med. Chem. Commun.* **2011**, *2*, 1135.

[84] Li G.; Morales-Rivera C. A.; Wang Y.; Gao F.; He G.; Liu P.; Chen G. *Chem. Sci.*, **2016**.

[85] Studer, A.; Curran, D. P. *Angew. Chem. Int. Ed.* **2016**, *55*, 58.

[86] Yasu, Y.; Koike, T.; Akita, M. *Adv. Synth. Catal.* **2012**, *354*, 3414.

[87] (a) Huang, H.; Jia, K.; Chen. Y. *Angew. Chem. Int. Ed.* **2015**, *54*, 1881. (b) Huang, H.; Zhang, G.; Gong, L.; Zhang, S.; Chen. Y. *J. Am. Chem. Soc.* **2014**, *136*, 2280.

[88] (a) Tellis, J. C.; Primer, D. N.; Molander, G. A. *Science* **2015**, *345*, 433. (b) El Khatib, M.; Serafim, R. A. M.; Molander, G. A. *Angew. Chem. Int. Ed.* **2016**, *55*, 254.

[89] (a) Huang, H.; Jia, K.; Chen. Y. *Angew. Chem. Int. Ed.* **2015**, *54*, 1881. (b) Huang, H.; Zhang, G.; Gong, L.; Zhang, S.; Chen. Y. *J. Am. Chem. Soc.* **2014**, *136*, 2280.

[90] (a) Newhouse T.; Baran, P. S.; *Angew. Chem. Int. Ed.*, **2011**, *50*, 3362; (b) White, M. C. *Science*, **2012**, *335*, 807; (c) Genovino, J.; Sames, D.; Hamann, L. G.; Touré, B. B. *Angew. Chem., Int. Ed.*, **2016**, *55*, 14218.

[91] (a) Wender, P. A.; Hilinski, M. K.; Mayweg, A. V. W. *Org. Lett.*, **2005**, *7*, 79; (b) Chen, K.; Baran, P. S. *Nature*, **2009**, *459*, 824; (c) Stang, E. M.; White, M. C. *Nature Chem.*, **2009**, 1, 547.

[92] For other selected methods for C(sp3)-H oxygenation: (a) Li, X.; Che, X.; Chen, G.-H.; Zhang, J.; Yan, J.-L.; Zhang, Y.-F.; Zhang, L.-S.; Hsu, C.-P.; Gao, Y. Q.; Shi, Z.-J. *Org. Lett.*, **2016**, *18*, 1234; (b) Ozawa, J.; Tashiro, M.; Ni, J.; Oisaki, K.; Kanai, M. *Chem. Sci.*, **2016**, *7*, 1904.

[93] For a photoredox-catalyzed sulfonate-directed C(sp3)-H hydroxylation, see: Hollister, A.; Conner, E. S.; Spell, M. L.; Deveaux, K.; Maneval, L.; Beal, M. W.; Ragains, J. R.; *Angew. Chem., Int. Ed.*, **2015**, *54*, 7837.

[94] Li, G. X.; Morales-Rivera, C. A.; Gao, F.; Wang, Y.; He, G. Liu, P.; Chen, G. *Chem. Sci.*, **2017**, *8*, 7180-7185.

[95] Wang, Y.; Hu, X.; Morales-Rivera, C. A.; Li, G. X.; Huang, X.; He, G.; Liu, P.; Chen, G. *J. Am. Soc.*, **2018**, *140*, 9678-9684.

[96] Hand book of Chemistry and Physics. 90th edition, David R. Lide, CRC Press, **2009-2010**.

[97] Bock, C. R.; Meyer, T. J.; Whitten, D. G. *J. Am. Chem. Soc.*,**1975**, *97*, 2909.

[98] Isse, A. A.; Gennaro, A. *J. Phys. Chem. B* **2010**, *114*, 7894.

[99] (a) Bartmess, J. E. *J. Phys. Chem.* **1994**, *98*, 6420−6424. (b) Bartmess, J. E. *J. Phys. Chem.* **1995**, *99*, 6755−6755.

[100] Although the intramolecular I−O interaction stabilizes **4-5**, there is still sufficient radical character on the O atom that manifests similar reactivity as that of typical *O*-centered radicals.

[101] (a) Ollivier, C.; Renaud, P. *Chem. Rev.* **2001**, *101*, 3415. (b) Schaffner, A.-P.; Renaud, P. *Eur. J. Org. Chem.* **2004**, 2291. (c) Carra, C.; Scaiano, J. C.; *Eur. J. Org. Chem.* **2008**, 4454. (d) Liu, D.; Li, Y.; Qi, X.; Liu, C.; Lan, Y.; Lei, A. *Org. Lett.* **2015**, *17*, 998.

[102] For an excellent review on homolytic substitution reaction: Davies, A. G.; Roberts, B. P. *Acc. Chem. Res.* **1972**, *5*, 387.

[103] (a) Heberger, K. & Lopata, A. *J. Org. Chem.*, **1998**, *63*, 8646-8653; (b) De Vleeschouwer, F., Van Speybroeck, V., Waroquier, M., Geerlings, P. & De Proft, F. *Org. Lett.*, **2007**, *9*, 2721-2724; (c) Fisher, H. & Radom, L. *Angew. Chem. Int. Ed.*, **2001**, *40*, 1340-1371; (d) Mayer, J. M. *Acc. Chem. Res.*, **2011**, *44*, 36-46; (e) Capaldo, L. & Ravelli, D. *Eur. J. Org. Chem.*, **2017**, 2056-2071; (f) Crossley, S. W. M., Barabe, F. & Shenvi, R. A. *J. Am. Chem. Soc.*, **2014**, *136*, 16788-16791.

[104] Antonchick, A. P. & Burgmann, L. Direct selective oxidative cross-coupling of simple alkanes with heteroarenes. *Angew. Chem. Int. Ed.*, **2013**, *52*, 3267-3271.

[105] Azidyl radical: Workentin, M. S., Wagner, B. D., Lusztyk, J. & Wayner, D. D. M. *J. Am. Chem. Soc.*, **1995**, *117*, 119-126.

[106] Barluenga, J., Campos-Gomez, E., Rodriguez, D., Gonzalez-Bobes, F. & Gonzalez, J. M. *Angew. Chem. Int. Ed.*, **2005**, *44*, 5851-5854.

[107] Ochiai, M. et al. *J. Am. Chem. Soc.*, **1996**, *118*, 7716-7730.

[108] Liu, F., Yang, Z., Yu, Y., Mei, Y. & Houk, K. N. *J. Am. Chem. Soc.*, **2017**, *139*, 16650-16656.

[109] (a) Purser, S., Moore, P. R., Swallow, S. and Gouverneur, V. Fluorine in medicinal chemistry. *Chem. Soc. Rev.*, **2008**, *37*, 320-330. (b) Ojima, I. *Fluorine in Medicinal Chemistry and Chemical Biology*. (Blackwell Publishing Ltd, **2009**). (c) Liang, T., Neumann, C. N. & Ritter, T. Introduction of fluorine and fluorine-containing functional groups. *Angew. Chem. Int. Ed.*, **2013**, *52*, 8214-8264.

[110] Muller, K., Faeh, C. & Diederich, F. *Science*, **2007**, *317*, 1881-1886.

[111] (a) Hojczyk, K. N.; Feng, P. J.; Zhan, C. B.; Ngai, M. Y. *Angew. Chem., Int. Ed*, **2014**, *53*, 14559-14563. (b) Feng, P. J.; Lee, K. N.; Lee, J. W.; Zhan, C. B.; Ngai, M. Y. *Chem. Sci.*, **2016**, *7*, 424-429.

[112] Hojczyk, K. N.; Feng, P. J.; Zhan, C. B.; Ngai, M. Y. *Angew. Chem.*, **2014**, *126*, 14787-14791.

[113] (a) Zheng, W.; Morales-Rivera, C. A.; Peng, L.; Ngai, M. Y. *Angew. Chem. Int. Ed.* **2018**, *57*, 9645-9649. (b) Zheng, W.; Lee, J. W.; Morales-Rivera, C. A.; Liu, P.; Ngai, M. Y. *Angew. Chem. Int. Ed.* **2018**, *130*, 13991-13995. (c) Lee, J. W.; Zheng, W.; Morales-Rivera, C. A.; Liu, P.; Ngai, M. Y. *Chem. Sci.* **2019**, *10*, 3217-3222.

[114] Gassman, P. G.; Granrud, J. E. *J. Am. Chem. Soc.*, **1984**, *106*, 1498-1499.

[115] Hansch, P.; Leo, A.; Taft, R. W. *Chem. Rev.*, **1991**, *91*, 165-195.

[116] Lee, K. N.; Lei, Z., Morales-Rivera, C. A.; Liu, P.; Ngai, M. Y. *Org. Biomol. Chem.*, **2016**, 14, 5599-5605.

[117] The concerted 1,3-OCF_3 migration transition state that connects **5-7a** and **5-17** cannot be located. Scan of the potential energy surface indicates that the concerted transition state, even if it exists, would have a much higher barrier than the stepwise transition state (**5-TS1**).

[118] (a) Quinonero, D.; Garau, C.; Rotger, C.; Frontera, A.; Ballester, P.; Costa, A.; Deya, P. M.; *Angew. Chem. Int. Ed.*, **2002**, *41*, 3389-3392; (b) Schottel, B. L.; Chifotides, H. T.; Dunbar, K. R. *Chem. Soc. Rev.*, **2008**, *37*, 68-83.

[119] Although a thermal 1,3-hydrogen shift is symmetry-allowed according to the Woodward-Hoffmann rules, the requirement of the Mobius transition state geometry prohibits such a shift. (a) Dedobbelaere, J. R.; Vandijk, J. M. F.; Dehaan, J. W.; Buck, H. M. *J. Am. Chem. Soc.*, **1977**, *99*, 392-397; (b) Houk, K. N.; Li, Y.; Evanseck, J. D. *Angew. Chem. Int. Ed.*, **1992**, *31*, 682-708.

[120] (a) Kikugawa, Y.; Shimada, M. *J. Chem. Soc., Chem. Commun.* **1989**, 1450-1451; (b) Tabolin, A. A.; Ioffe, S. L. *Chem. Rev.*, **2014**, *114*, 5426-5476.

[121] Bock, C. R.; Meyer, T. J.; Whitten, D. G., *J. Am. Chem. Soc.* **1975,** *97*, 2909

[122] Isse, A. A.; Gennaro, A. *J. Phys. Chem. B* **2010**, *114*, 7894.

[123] (a) Bartmess, J. E. *J. Phys. Chem.* **1994**, *98*, 6420−6424. (b) Bartmess, J. E. *J. Phys. Chem.* **1995**, *99*, 6755−6755.

[124] Prier, C. K.; Rankic, D. A.; MacMillan, W. C. *Chem. Rev.* **2013**, *113*, 5322-5363.